University of Kentucky
UKnowledge

Theses and Dissertations--Civil Engineering | Civil Engineering

2022

GEOPHYSICS-BASED GROUND CONTROL AND EXCAVATION DESIGN METHODOLOGY BASED ON ACCEPTABLE DAMAGE

Jorge Romana Giraldo
University of Kentucky, jromanagiraldo@gmail.com
Digital Object Identifier: https://doi.org/10.13023/etd.2022.438

Right click to open a feedback form in a new tab to let us know how this document benefits you.

Recommended Citation
Romana Giraldo, Jorge, "GEOPHYSICS-BASED GROUND CONTROL AND EXCAVATION DESIGN METHODOLOGY BASED ON ACCEPTABLE DAMAGE" (2022). *Theses and Dissertations--Civil Engineering*. 127.
https://uknowledge.uky.edu/ce_etds/127

This Doctoral Dissertation is brought to you for free and open access by the Civil Engineering at UKnowledge. It has been accepted for inclusion in Theses and Dissertations--Civil Engineering by an authorized administrator of UKnowledge. For more information, please contact UKnowledge@lsv.uky.edu.

STUDENT AGREEMENT:

I represent that my thesis or dissertation and abstract are my original work. Proper attribution has been given to all outside sources. I understand that I am solely responsible for obtaining any needed copyright permissions. I have obtained needed written permission statement(s) from the owner(s) of each third-party copyrighted matter to be included in my work, allowing electronic distribution (if such use is not permitted by the fair use doctrine) which will be submitted to UKnowledge as Additional File.

I hereby grant to The University of Kentucky and its agents the irrevocable, non-exclusive, and royalty-free license to archive and make accessible my work in whole or in part in all forms of media, now or hereafter known. I agree that the document mentioned above may be made available immediately for worldwide access unless an embargo applies.

I retain all other ownership rights to the copyright of my work. I also retain the right to use in future works (such as articles or books) all or part of my work. I understand that I am free to register the copyright to my work.

REVIEW, APPROVAL AND ACCEPTANCE

The document mentioned above has been reviewed and accepted by the student's advisor, on behalf of the advisory committee, and by the Director of Graduate Studies (DGS), on behalf of the program; we verify that this is the final, approved version of the student's thesis including all changes required by the advisory committee. The undersigned agree to abide by the statements above.

Jorge Romana Giraldo, Student

Dr. L. Sebastian Bryson, Major Professor

Dr. Mei Chen, Director of Graduate Studies

GEOPHYSICS-BASED GROUND CONTROL AND EXCAVATION DESIGN METHODOLOGY BASED ON ACCEPTABLE DAMAGE

DISSERTATION

A dissertation submitted in partial fulfillment of the requirements

for the degree of Doctor of Philosophy

in the College of Engineering at the University of Kentucky

By

Jorge Octavio Romana Giraldo

Lexington, Kentucky

Director: Dr. L. Sebastian Bryson,

Hardin-Drnevich-Huang Professor of Civil Engineering

Lexington, Kentucky

2022

Copyright © Jorge O. Romana Giraldo 2022

ABSTRACT OF DISSERTATION

GEOPHYSICS-BASED GROUND CONTROL AND EXCAVATION DESIGN METHODOLOGY BASED ON ACCEPTABLE DAMAGE

This dissertation is structured around a novel conceptual framework for designing deep excavation retaining systems and using geophysical data to estimate the mechanical response of soft soil deposits. It begins with presenting an approach to design excavation retaining walls based on limiting damage to adjacent infrastructure. In this approach, the damage is defined based on critical distortions of an idealized laminate beam model used for representing the adjacent building deformations. The wall and support elements of the support system are then designed such that the system yields the limiting ground deformations. The resulting excavation support system limits damage to adjacent structures below an acceptable level and automatically satisfies the structural stability requirements. More significantly, the design of the excavation support system does not require an iterative process.

Also, this dissertation presents an experimental study of geophysical measurements, shear wave velocities, for soft soils under isotropic consolidation. The presented results show that the variation of effective stress during consolidation can be determined based on shear wave measurements. An approach to estimate consolidation processes based on a 1D hypoplastic model with three parameters is presented. In addition, the proposed method showed favorable results for ko-consolidation conditions. Based on

the defined parameters of the model, it is possible to estimate the complete stress history of the soil.

Finally, this study proposed a shear wave-based approach to predicting the triaxial behavior of cohesive soils. Laboratory tests with bender elements were performed for silt-predominant samples from the state of Kentucky. A function to relate mean effective stresses and shear wave velocities was adapted from the measured behavior to predict undrained and drained triaxial behavior. Using the previous function in conjunction with a hypoplastic model for soft soils expressed in stress invariants, the deviatoric strains, volumetric strains, and excess porewater pressures developed during shearing were predicted. The proposed methodology performed very well in simulating the various soils under undrained and drained conditions.

KEYWORDS: Deep excavations, Building Damage, Geophysical testing, Shear wave velocity, Triaxial testing

Jorge O. Romana Giraldo

October 12, 2022

GEOPHYSICS-BASED GROUND CONTROL AND EXCAVATION DESIGN METHODOLOGY BASED ON ACCEPTABLE DAMAGE

By

Jorge Octavio Romana Giraldo

Dr. L. Sebastian Bryson
Director of Dissertation

Dr. Mei Chen
Director of Graduate Studies

October 12, 2022

ACKNOWLEDGEMENTS

I sincerely express my gratitude to my advisor, Dr. L. Sebastian Bryson, for providing guidance and feedback throughout this study. His expertise and experience significantly contributed to my professional and personal development. It was an excellent opportunity to work and study under his leadership.

I would also like to thank my Committee Members, Dr. Michael Kalinski, Dr. Gabriel Dadi, Dr. Jhon Silva Castro, and Dr. Nelson Akafuah. Thanks to the Department of Civil Engineering staff for their help during my lab work.

This dissertation would not have been possible without my family and friends. Thanks for all the support you have provided me through this investigation. Special thanks to Emma.

TABLE OF CONTENTS

LIST OF TABLES

LIST OF FIGURES

CHAPTER 1
INTRODUCTION

1.1 PROBLEM STATEMENT

Along with the development of modern cities, there is a need for underground space to satisfy the population's necessities through transportation systems, water management, parking garages, shopping centers, and other facilities. Consequently, deep excavations are popular in urban environments. Typically, in large metropolitan areas, these excavations are in the vicinity of existing infrastructures such as buildings and pipe utilities (Figure 1-1). Considering that the performance of deep excavations is evaluated based on the integrity of adjacent structures, it is generally required to monitor the excavation process in terms of wall deformations, water pressures, ground settlements, and building tilt to avoid damage to these structures. Furthermore, these monitoring results should be incorporated into the excavation process in real-time to prevent further damage if observed or to control damage within acceptable limits. Therefore, an excavation process, which is a highly dynamic environment, may adapt to the response of its surroundings.

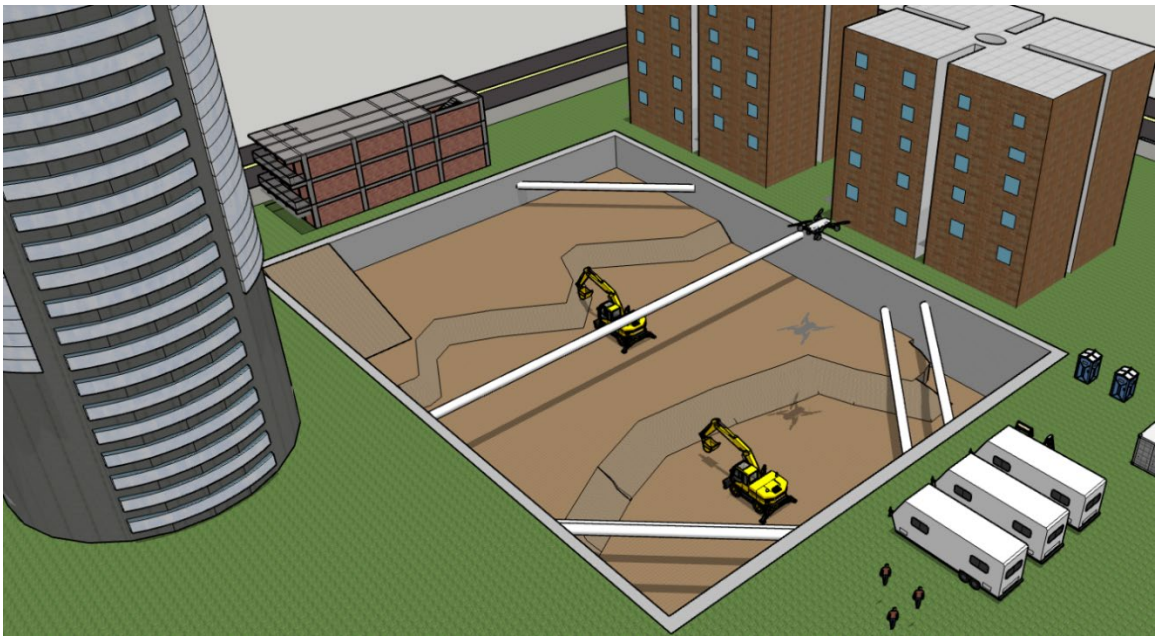

Figure 1-1 Deep excavation in an urban environment

Controlling the extent to which deep excavations threaten existing structures is of particular interest because the cost associated with induced damage may be significant. The

associated cost of a project can be better estimated if the damage caused by the deep excavation is determined accurately and updated based on the existing excavation conditions and surrounding infrastructure. In addition, uncertainties in the mechanical properties of the soil deposits, previous and during excavation, and construction sequence make the predictions of the excavation performance more challenging.

Because of the complexity of depositional and post-depositional processes, soil deposits are inherently spatially and temporally variable. Consequently, variations of material types, state conditions (e.g., density, degree of saturation), and stress states (e.g., in situ stresses and pre-consolidation stresses) dramatically affect the mechanical behavior of a soil mass. This ground variability implies that the mechanical behavior of a soil can differs significantly from one location to another within the overall soil mass affected by a deep excavation.

The traditional approach for characterizing a soil mass is collecting samples at discrete locations within the mass and performing various laboratory tests on each sample before the excavation. Instrumentation devices are also deployed at specific locations around the excavation to monitor its performance with time. However, the acquisition and interpretation of monitoring results at these predetermined locations are often time-consuming and labor-intensive. This discrete monitoring concern is particularly exacerbated for a highly variable deposit.

Although the design process of a deep excavation may be rigorous, uncertainties in predicted performance always arise before and during excavation. Some sources of uncertainty can be the numerical model of the excavation, the executed excavation process, ground composition and parameters, and unanticipated conditions found during the excavation. Thus, it is essential, to maintain a satisfactory performance of the excavation, to monitor the process through adequate instrumentation (Dunnicliff 1993).

Previous to any excavation activity, it might take excessive samples tested under a multitude of loading conditions to adequately predict behavior representative of the deposit and the adjacent infrastructures. Because of these limitations, the average or bulk values of soil parameters are typically used to characterize a soil mass and to predict potential mechanical behavior. Unfortunately, this approach often leads to unexplained deviations between actual and predicted soil and structure behavior. Geophysical methods allow for

determining material properties and behavior over a large spatial domain. In addition, geophysical methods provide data for areas that may not be accessible to sample extraction equipment.

Geophysical measurements, such as seismic wave velocities (e.g., shear wave and compression wave velocities) and electrical conductivity, EC are commonly used in hydrologic and geotechnical investigations for subsurface characterization. The geophysical properties of a soil system are affected by parameters such as soil type, pore structure, degree of saturation, stress state, and stress history (Hussien and Karray 2016). These parameters also affect the strength and deformation behavior of a soil system (Oh et al. 2017). Thus, geophysical measurements in soil deposits may provide a reliable means to monitor and predict mechanical behavior. Therefore, integrating geophysical measurements into a constitutive soil model would provide a bridge to predict soil stress-strain behavior and volume change/pore pressure change behavior over a large spatial domain. Given the capabilities of modern geophysical testing, real-time data can be collected efficiently. This information will allow the maintenance of the safety of the excavation and the structures in the vicinity.

1.2 CONCEPTUAL OVERVIEW

Typical elements in an excavation in an urban environment are presented in Figure 1-2. The first element considered corresponds to the adjacent infrastructure. As a consequence of the excavation, the caused ground settlements and displacements, which are the second element, impose distortions and strains on the infrastructure. These induced movements are related to the support system (i.e., retaining wall, struts, wales, rakers, or anchors) deformation. A successful excavation procedure links these elements in such a manner that damages in the adjacent infrastructure are limited to admissible thresholds, defined typically by the owner of the adjoining property.

Element 1 relates the spatial (3D) distribution of building distortions with the damage criteria. This element establishes the damage incurred in the adjacent infrastructure based on induced movements by the excavation. From the several damage classifications, the ones that adjust to the building characteristics should be selected. The properties of the adjacent infrastructure may be included in the damage assessment.

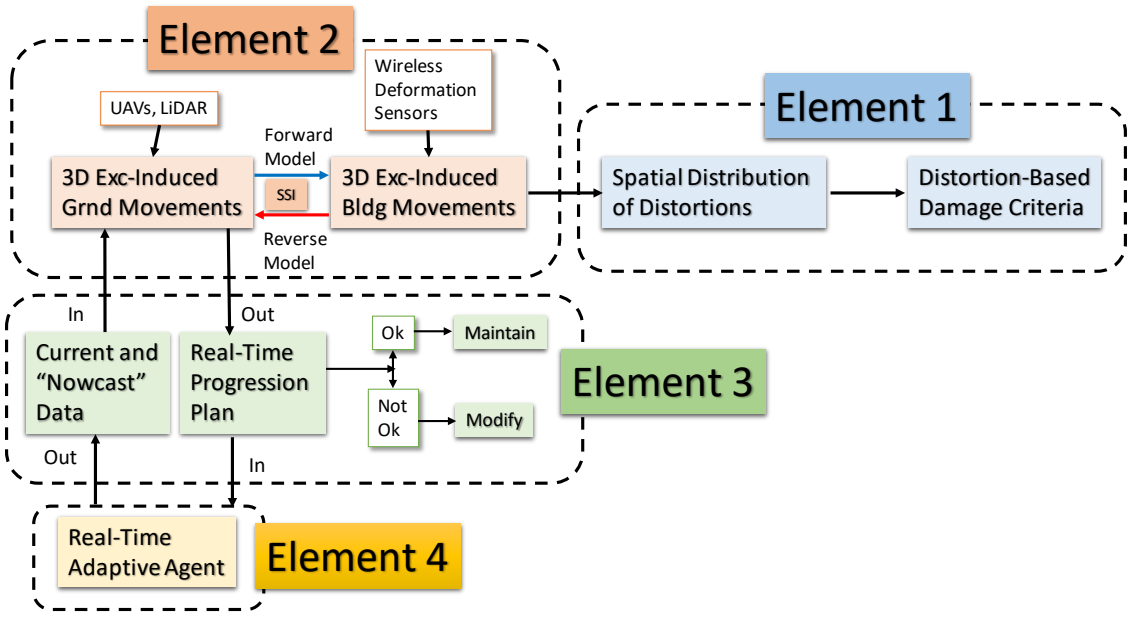

Figure 1-2 Conceptual model

Quantifying damage to adjacent facilities is necessary to evaluate the performance of the excavation support system. Since the early damage criteria (Skempton and MacDonald 1956), several researchers have proposed criteria to categorize damage based on some measurable quantities. Charts are typically used to determine the risk of damage in structures. Variables considered in the damage classification include lateral strain, angular distortion (differential settlement divided by the length between the two points), deflection ratio, cumulative crack width, settlement, and tilt of the building columns.

Element 2 corresponds to the soil-structure interaction and the estimation of building and ground movements. The relationship between these two movements is typically established based on fully coupled numerical simulations considering the soil-structure interface. The forward model, Figure 1-2, calculates the building response based on predicted/measured ground movements and building stiffness characteristics. In the reverse model, the process is the opposite because building deformations are used to estimate constraints to the spatial distribution of the ground movements. Also, it is highlighted that modern tools can be used to monitor these movements as geophysics testing, LiDAR, and wireless deformation sensors.

Element 3 corresponds to a monitoring program of damage and excavation sequence. It is expected that based on observation of induced damage, corrective actions

will be taken. Furthermore, unknown encountered conditions, as ground inclusions, during the excavation process need to be addressed to define the proper progression plan. In this dissertation, Element 4 is represented by the engineering practitioner in charge of taken the decisions based on the observed monitoring results.

G Geophysical testing provides a means to link Element 2 and Element 3 by implementing constitutive models using soil geophysical measurements such as seismic waves or electrical conductivity. Through this implementation, real-time excavation control may be executed based on geophysical testing within the area of influence of the excavation. Geophysics offers the advantage of covering larger areas during surveys; however, data processing may be more rigorous than in the case of individual instrumentation measurements as discrete locations around an excavation.

1.3 RESEARCH OBJECTIVES

The main objective of this research is to develop a novel methodology for designing deep excavation in an urban environment along with fundamental geophysics-based models that allow the estimation of ground response based on shear wave measurements.

The specific objectives of this research are developed to address the current deep excavation design practice and deformational behavior of the soil based on geophysics data that can be collected in real-time. These objectives include:

Implement a new design method to define retaining excavation system dimensions (i.e., wall, wales, and struts) based on damage to adjacent infrastructure from induced ground movements. This approach will consider the stochastic variation in the material properties of the structures through Monte Carlo analysis. In addition, the methodology will not require an iterative procedure to estimate a wall section from the damage threshold in nearby structures.

Develop an approach to estimate the stress history of a soil deposit based on measured shear wave velocities. This approach should be able to predict effective stress changes regardless of unloading and reloading directions.

Investigate the variation of shear wave velocity during drained and undrained testing and develop a stress function to incorporate it into a constitutive model for soft soils. Furthermore, integrate the volume change and shear geophysical-based functions into the soil constitutive model to produce a new geophysics-based model capable of estimating soil strains and stresses.

1.4 CONTENTS OF DISSERTATION

Chapter 2 proposes a novel methodology that directly designs an excavation support system by first considering an acceptable level of damage in the surrounding facilities and estimating the corresponding ground deformations. The wall and support elements of the support system are then designed such that the system yields the limiting ground deformations. The resulting excavation support system limits damage to adjacent structures below an acceptable level and automatically satisfies the structural stability requirements. More significantly, the design of the excavation support system does not require an iterative process.

Chapter 3 presents an experimental study of geophysical measurements and shear wave velocity for soft soils under isotropic consolidation. The results show that effective stress variation during consolidation can be determined based on shear wave measurements. An approach to estimate consolidation processes based on a 1D hypoplastic model with three parameters is presented. In addition, the presented approach showed favorable results for ko-consolidation conditions. Based on the defined parameters of the model, it is possible to estimate the soil's complete stress history regardless of the loading or unloading cycles.

Chapter 4 aimed to develop a geophysics-based approach to predicting the triaxial behavior of cohesive soils. Laboratory tests with bender elements were performed for silt-predominant samples from the state of Kentucky. A function to relate mean effective stresses and shear wave velocities was adapted from the measured behavior to predict undrained and drained triaxial behavior. Using the previous function in conjunction with a hypoplastic model for soft soils expressed in stress invariants, the deviatoric strains, volumetric strains, and excess porewater pressures developed during shearing were

predicted. The proposed methodology performed very well in simulating the various soils under undrained and drained conditions.

Chapter 5 briefly presents the findings and conclusions of the research prescribed in the previous Chapters 2-4.

CHAPTER 2
EXCAVATION SUPPORT SYSTEM DESIGN METHOD TO LIMIT DAMAGE IN ADJACENT INFRASTRUCTURE

2.1 INTRODUCTION

A major concern for urban construction projects involving deep excavations is the impact of excavation-related ground movements on adjacent buildings and utilities. Consequently, rigid, or stiff excavation support systems are required to execute the work (Koutsoftas et al. 2000; Finno et al. 2002; Chen et al. 2018). The conventional approach for designing an excavation support system is to use a limit equilibrium approach to determine the required capacity and stiffness of the excavation support system. Loads applied to deep excavation support systems are typically obtained from apparent earth pressure envelopes (Peck 1969; Tschebotarioff 1973; Sabatini et al. 1999), which, as the name implies, are not distributions of pressure but upper limits of average measured pressures. Although this approach may provide an adequate factor of safety against structural failure, it shows no regard to the ground movements that might impact adjacent structures. Therefore, potential excavation-induced damages to adjacent infrastructure are not directly controlled during the initial design stage of the support system.

Numerical methods, such as finite elements or finite difference, may give reliable predictions of ground displacements within the excavation. However, the intrinsic variability of soil deposits and their incremental nonlinear behavior makes the prediction of displacements away from the excavation somewhat problematic. Moreover, additional challenges arise when the behavior of the adjacent infrastructure is included in the numerical models. The extent and magnitude of excavation-induced ground movements in urban environments depends on the adjacent building type and configuration, support system type and performance, ground conditions, and construction activities. Consequently, idealizations of the ground and building response must be used in practice for the design of excavation support systems.

Several empirical and semiempirical methods have been developed to predict induced deformations adjacent to an excavation. These approaches vary from simple envelopes considering only generic soil conditions (Peck 1969; Clough 1990; Roboski and Finno 2006) to more sophisticated approaches that combine the support system

characteristics and the soil parameters (Clough et al. 1989; Hsieh and Ou 1998; Kung et al. 2007; Schuster et al. 2009; Bryson and Zapata-Medina 2012). Potential damages to adjacent structures are assessed by imposing these induced deformations onto the adjacent structures. During this process, the structures and ground are modeled using simplified assumptions of soil-structure interaction (Boone et al. 1999; Schuster et al. 2009; Son and Cording 2011; Halim and Wong 2012; Goh and Mair 2014; Tan et al. 2016). The level of damage is compared with established damage criteria (Skempton and Macdonald 1956; Burland and Wroth 1975; Boscardin and Cording 1989; Boone 1996), and the adequacy of the excavation support system is determined based on the degree of damage accepted by the designer. Because the damage level of the structure is estimated at the end of the wall design process, the design involves iterations of the support system characteristics until the required stiffness of the system complies with the acceptable level of damage. Given that the design process is iterative, any variation in the adjacent structure characteristics from a previous definition may cause a complete redefinition of the support system characteristics.

This study presents a new design methodology for excavation support systems. The proposed method directly designs an excavation support system by first considering an acceptable level of damage in the surrounding facilities and estimating the corresponding ground deformations. The wall and support elements of the support system are then designed such that the system yields the limiting ground deformations. The resulting excavation support system limits damage to adjacent structures below an acceptable level and, thus, automatically satisfies the structural stability requirements. More significantly, the design of the excavation support system does not require an iterative process.

2.2 DESIGN APPROACH CONCEPT

The design approach of excavation support systems for tolerable deformations is divided into three general elements. Figure 2-1 presents these elements in the context of the proposed design process. Firstly, the characteristics of the adjacent infrastructure (Element 1) are determined along with the tolerable damage. Then, this acceptable damage level in the structure is related analytically, via a structural idealization, to distortions and the corresponding maximum vertical settlement caused by the nearby deep excavation (Element 2). Afterward, the vertical displacement profile (i.e., settlement profile)

determined by the maximum vertical settlement is related to the horizontal wall movements (Element 3). In this study, this relationship is based on simplified assumptions of zero volume change in the soil during the excavation process (i.e., undrained conditions) (Finno et al. 2002). From the approximation of horizontal wall movements and from characterizations of support system stiffness, the wall characteristics are selected in a way that limits the estimated lateral deformation.

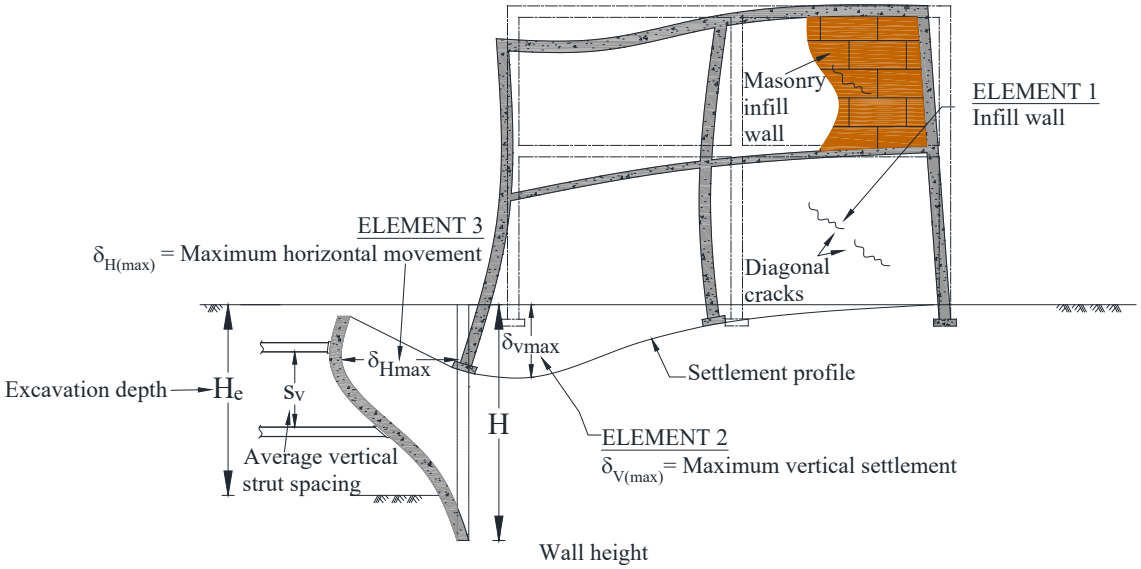

Figure 2-1 Conceptual approach to deformation-based excavation support system design

Although there is extensive literature for each of the individual elements presented in Figure 2-1, there is not an integrated design methodology. The proposed approach corresponds to a deep excavation in which plain strain conditions are applicable. A framed building represents the adjacent infrastructure and is in the zone in which the excavation causes the largest ground deformations and subsequent building distortions. Characteristics of the considered elements are discussed herein. The proposed methodology combines all the elements of the excavation support system design in a single process.

2.2.1 Quantification of damage to adjacent excavation

The quantification of damage is an important aspect of assessing the performance of an excavation support system. Boone et al. (1999) presented a general procedure to evaluate the damage in adjacent infrastructure subjected primarily to spandrel-type ground movements. These researchers developed damage criteria based on cumulative crack width

due to principal tensile strain and cumulative tensile strain. Son and Cording (2005) slightly modified the damage criteria proposed by Boscardin and Cording (1989) by using the average state of strain in an equivalent beam with a percentage of openings. This approach resulted in a relationship between the angular distortion and the magnitude of cracking strains. However, the Son and Cording (2005) method does not explicitly predict the cracking strains. Kotheimer and Bryson (2009) assessed excavation-induced damage by estimating crack width progression in infill walls of adjacent buildings. These researchers estimated crack width as a function of diagonal strain as suggested by Dulácska (1992). Figure 2-2(a) shows the distortions experienced by an infill wall resulting from differential settlement between the columns. In the figure, δ is the differential settlement, β is angular distortion, ld is the original length of the diagonal, and Δld is the change in the length of the diagonal.

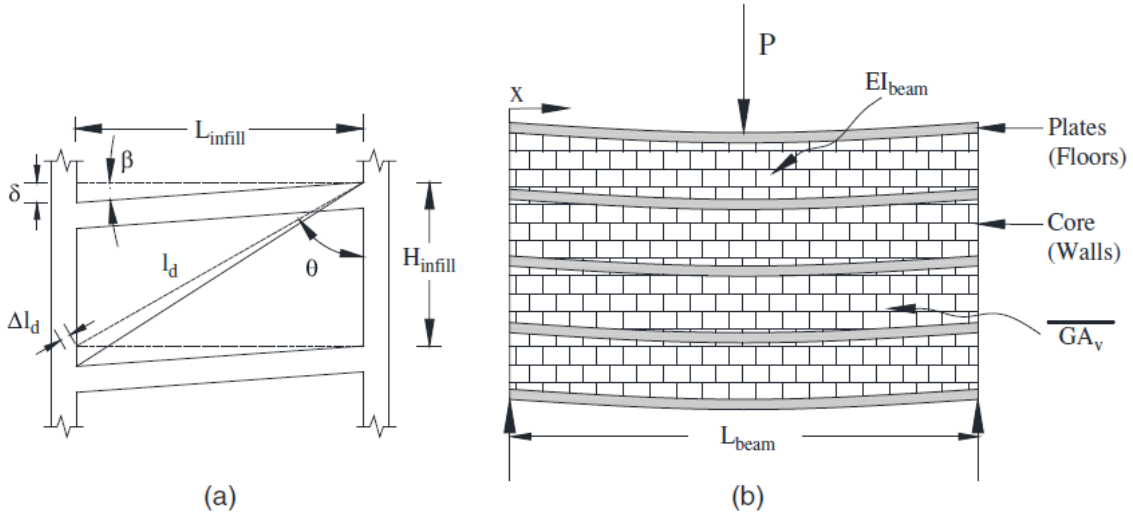

Figure 2-2 Damage quantification: (a) building frame and infill wall; and (b) laminate beam model

The Kotheimer and Bryson (2009) approach equates the diagonal strain to the normalized crack width and is shown to be proportional to distortion, which is defined as the differential settlement divided by the distance between the two settling points. The normalized crack width is thus given as

$$\frac{\Delta l_c}{L_{\text{infill}}} = \eta\left(\beta_{meas} - \beta_{crit}\right)\frac{H_{\text{infill}}}{\sqrt{H_{\text{infill}}^{\ 2} + L_{\text{infill}}^{\ 2}}} \qquad (2\text{-}1)$$

where Δl_c = estimated crack width; β_{meas} = measured or anticipated ground distortion; β_{crit} = critical distortion of the infill wall; H_{infill} = height of the infill wall; L_{infill} = length of the infill wall; and η = flexibility factor, which accounts for the stiffness of a building or a wall section. It ranges from 0.5 for a solid wall to 1.0 for a highly punctured wall. Figure 2-2 (a) corresponds to an infill wall bounded by a frame. The type of connections for the frame can be considered by adjusting the length in Eq. (2-1). For pinned connections, such as simple beams and columns, the length term is multiplied by unity and the deformed shape resembles a rhombus. For rigid connections, such as a concrete frame, the end rotations are restricted. It is assumed that 1/4 of the length on both sides is restricted. Thus, the length in Eq. (2-1) is multiplied by 0.5 when calculating the normalized crack width for a rigid connection.

From Eq. (2-1), the ground distortion that corresponds to acceptable normalized crack width, predefined by the designer, $\beta_{\max}$, can be determined as

$$\beta_{\max} = \left(\frac{\Delta l_c}{L_{\text{infill}}} \right) \frac{\sqrt{H_{\text{infill}}^2 + L_{\text{infill}}^2}}{H_{\text{infill}}} \frac{1}{\eta} + \beta_{crit} \tag{2-2}$$

2.2.2 **Critical distortions in infill walls**

Critical distortion is defined as the distortion at the onset of cracking. Although some sources (Polshin and Tokar 1957; Burland and Wroth 1975) tend to represent critical distortion as a single value for a given type of structure, the value is more appropriately determined as a function of the building configuration, number of floors, and stiffness (Son and Cording 2011; Goh and Mair 2014; Tan et al. 2016). Finno et al. (2005) proposed the laminate beam model to determine the critical distortion as shown in Figure 2-2(b). The laminate beam comprises a multistory building with floor slabs, infill walls, and columns subject to excavation-induced ground movements. Within the laminate beam model, infill walls resist shear deformation while the floors resist bending deformation. Considering the building as a simply supported beam, Finno et al. (2005) related the deflection ratio to bending strain, at the top and bottom of the laminate beam, and diagonal strain on each floor.

Consider a simply supported beam subjected to a concentrated load. The deflection and slope of the beam including shear deformations are given by

$$\delta(x) = \frac{PL_{beam}^2}{48EI_{beam}}\left(\frac{x}{L_{beam}}\right)\left(3 - 4\frac{x^2}{L_{beam}^2}\right) + \frac{Px}{2\overline{GA_v}} \tag{2-3}$$

$$\frac{d\delta(x)}{dx} = \frac{P\left(L_{beam}^2 - 4x^2\right)}{16EI_{beam}} + \frac{P}{2\overline{GA_v}} \tag{2-4}$$

where $\delta(x) =$ beam deflection at a distance x from support; $EI_{beam} =$ bending stiffness of the beam; $L_{beam} =$ length of the beam; $P =$ concentrated load; and $\overline{GA_v} =$ equivalent shear stiffness as defined by Finno et al. (2005). Note that Timoshenko (1957) used a shear coefficient, α_s, to determine the deflection of the loaded beam. However, based on the derivations by Finno et al. (2005), this effect is included in the stiffness of the laminate beam in which the shear force in a cross section is distributed only in the infill walls.

The angular distortion, β, is assumed to be the maximum slope along the beam and is obtained as

$$\beta = \frac{PL_{beam}^2}{16EI_{beam}} + \frac{P}{2\overline{GA_v}} \tag{2-5}$$

Considering that the maximum shear force in the beam is given by $V = P/2$, Eq. (2-5) can be expressed as

$$\beta = \left(\frac{L_{beam}^2}{8EI_{beam}} + \frac{1}{2\overline{GA_v}}\right)V \tag{2-6}$$

Using the laminate beam approach as proposed by Finno et al. (2005) and considering the distribution of shear in each story, the critical distortion on each story will be

$$\beta_{crit_i} = \left(\frac{L^2\left(GA_v\right)_i}{8EI\frac{V_i}{V}} + \frac{\left(GA_v\right)_i}{\overline{GA_v}\frac{V_i}{V}}\right)\gamma_{crit_i} \tag{2-7}$$

where γ_{crit_i} = critical shear strain of the wall material of each wall. Details about the estimation of the equivalent bending, EI_{beam}, and shear stiffness of the structure, $\overline{GA_v}$, are presented in Finno et al. (2005).

Eq. (2-7) allows the estimation of the critical distortion based on a given critical shear strain. Using the critical strain calculated from Eq. (2-7), the normalized crack width of an infill wall can be approximated with Eq. (2-1). It should be noted that the angular distortion in this study does not account for rigid body tilt.

Figure 2-3 shows the calculated critical distortion, for a hypothetical building with uniform floors, as a function of the number of floors. A critical shear strain, γ_{crit}, of 0.11% was used for the masonry walls (Boone 1996). The height of the infill walls was considered as $H_{\text{infill}} = 3.86$ m. Material properties were considered as $E_c = 24.8$ GPa and $G_c =$ 10.3 GPa for the concrete, $E_m = 12.4$ GPa and $G_m = 4.96$ GPa for the masonry. In this example, the third floor has the lowest critical distortion and is therefore more likely to experience cracks during the excavation. This result is derived from the distribution of shear force along the section in which the third story has the highest percentage of shear in this laminate beam model. If there were openings in any of the floors, the cracking assessment would be different based on the different stiffness of the structure. It is also observed from this figure that the floors with less percentage of shear $\left(V_i/V\right)$ will tend to have a greater critical distortion as floors one and five in this hypothetical case. For this case, the critical distortion calculated using the laminated beam approach does not show significant variation for typical $L_{\text{infill}}/H_{\text{infill}}$ ratios between 1 and 4.

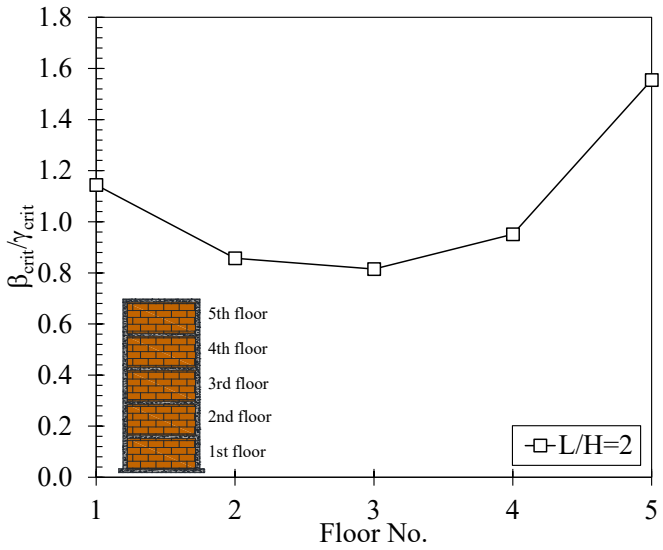

Figure 2-3 Variation of critical distortion normalized by the critical shear

2.2.3 Probability of exceedance critical distortion

Recognizing the uncertainty in the infill properties used for the laminated beam, a simplified probabilistic analysis is presented here for the determination of the critical distortion. This analysis will then be linked to the design process presented later in which the designer can associate a probability of cracking with the wall design. A Monte Carlo simulation was conducted to estimate the probability distribution of the critical distortion based on uncertain structure properties. Infill properties were considered as random variables, specifically the shear modulus of the masonry and the Young's modulus of concrete. The mean values of these properties were taken as previously mentioned and the coefficients of variation were 0.24 and 0.124, respectively, based on Choudhury and Kaushik (2018). These two variables were considered as normally distributed. The Monte Carlo simulation was carried out with 1,000 samples for this case.

Error! Reference source not found. (a) shows the empirical cumulative distribution function (CDF) of the critical distortion based on the Monte Carlo (MC) simulation of a hypothetical building of three floors (i.e., solid line). The empirical CDF was plotted as the proportion of values less than or equal to a given value of β_{crit}. Assuming that the building distortion is distributed as lognormal variable (Zhang and Ng 2005), the theoretical CDF was calculated as

$$CDF\left(\beta_{crit}\right)=0.5\left[1+erf\left(\ln\left(\beta_{crit}\right)-\frac{\mu}{\sqrt{2}\sigma}\right)\right] \tag{2-8}$$

where μ and $\sigma=$ mean and standard deviation of the natural logarithm of the critical distortion, respectively. **Error! Reference source not found.**(b) shows probability of exceedance a critical distortion for the same structure as a function of openings percentage of the infill walls. The percentages in **Error! Reference source not found.** represent the average percentage of openings on each floor. As shown, increasing the percentage of openings in the infill walls tends to decrease the critical distortion as observed in the shift of the curves. It is noted that this figure represents a specific building configuration (i.e., three floors). Other configurations, such as additional floors, can be represented using the same approach followed in this study.

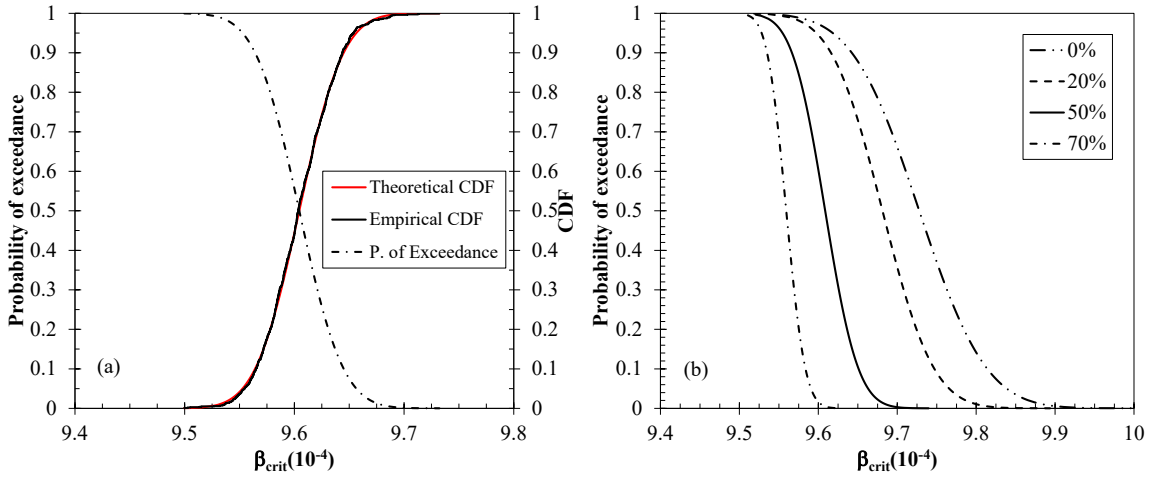

Figure 2-4 Probability of exceedance for the critical distortion using a Monte Carlo simulation: (a) cumulative distribution function (CDF) of the critical distortion; and (b) effect of openings on probability of exceedance for the critical distortion

2.3 EXCAVATION-INDUCED GROUND MOVEMENTS

Excavation-induced ground movements describe the lateral deformations of the excavation support system that develop in response to each stage of the excavation. The lateral deformations are accompanied by vertical deformations (i.e., ground settlement) behind the excavation support wall, which impinges on adjacent buildings, utilities, and other facilities. Thus, stringent limits to excavation-related deformations are required in congested urban areas. To protect adjacent infrastructure, it is critical to develop a design methodology based on limiting the deformations, as opposed to being based on limit state

conditions. Figure 2-5 presents the typical ground movements caused by excavation. In the figure, H is the total height of the wall; H_e is the excavation depth; z is the depth beginning at the ground surface; $\bar{z}$ is the depth normalized by the total embedded depth of the wall; x' is the location of the pivot point; L is the distance between to two arbitrary vertical settlement points, δ_V; β is the ground distortion calculated from the differential settlement of two arbitrary points; and δ_H is the lateral ground movements.

The lateral deformations of the support wall and the adjacent ground are often measured by inclinometers that provide a lateral deformation profile with respect to depth. Settlement behind the support wall is typically measured using a vertical control survey (i.e., construction survey). The settlement points of the survey define the settlement profile behind the wall. As can be inferred from Figure 2-5, the ground settlement is a function of the lateral deformations. The figure also shows that ground distortion is calculated from ground settlement, which by extension implies that ground distortion is a function of lateral deformations as well.

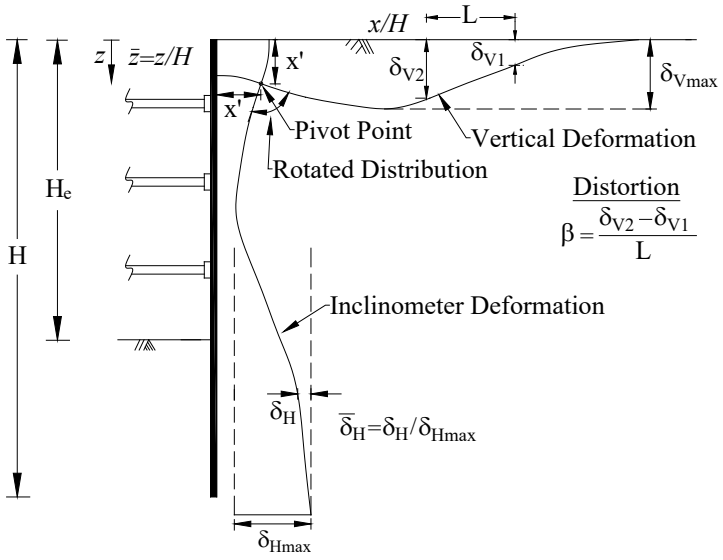

Figure 2-5 Typical excavation-induced ground movements, normalized

2.3.1 Settlement Profile Behind the Support Wall

Prediction of damage in adjacent infrastructure is determined by the induced settlement and lateral deformation profiles. A precise estimation of the settlement profile and ground distortions needs a detailed soil-structure interaction model to reflect the

complex ground changes caused by a deep excavation. From a practical standpoint, these detailed analyses may not be necessary in all cases. Consequently, simplified settlement profiles are used routinely to estimate the induced movements caused by the excavation. Several approaches have been suggested to estimate settlement distribution and envelopes behind a retaining wall (Clough 1990; Hsieh and Ou 1998; Kung et al. 2007). These methods consider the characteristics of the excavation and the excavated soil to evaluate the final induced movements.

2.3.1.1 Development of Simplified Settlement Profiles

Bryson et al. (2018) presented simplified lateral wall movement profiles based on the undrained shear strength of the excavated clay. The profiles were developed by overlaying trilinear plots over case history data in which the lateral deformations were normalized by the embedment depth of the excavation support walls and the lateral wall displacements were normalized by the maximum horizontal wall displacements. Finno et al. (2002) suggested that if the deformations of the clay layers are under undrained conditions (little or no volume change), the settlement profile can be approximated by rotating the lateral deformation profile of the wall by 90 degrees. From this approach, the settlement profiles for the different shear strengths can be estimated based on the normalized coordinates of lateral displacements by rotating the lateral wall displacement with respect to a pivot point (Figure 2-5). Figure 2-6 presents the approximated settlement profiles based on Bryson et al. (2018) lateral deformation profiles. The settlement profiles are given for three shear strength classifications: stiff clay su > 50 kPa, medium clay 25 kPa < su < 50 kPa, and soft clay su < kPa, where su is the undrained shear strength of the clay. Similar to the Bryson et al. (2018) lateral deformation profiles, the settlement profiles are presented as point settlement normalized with the maximum vertical settlement, as a function of the horizontal distance from the excavation support wall normalized by the depth of embedment of the support wall. The normalized coordinates of the settlement profiles were developed by slightly reinterpreting the data presented by Bryson et al. (2018) and are given in Table 2-1.

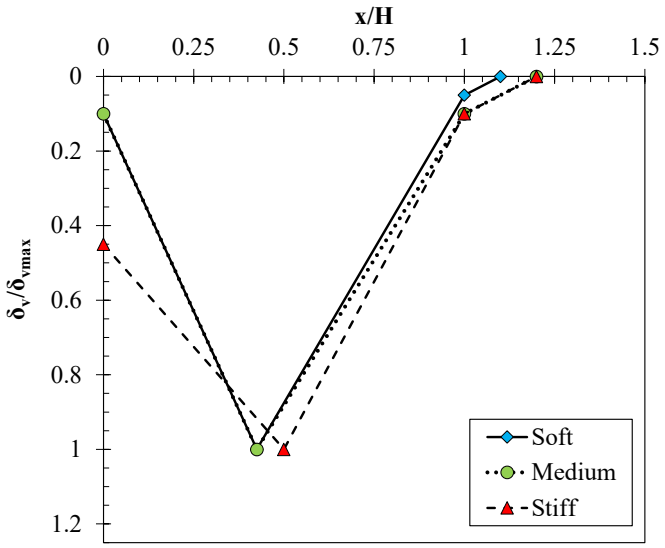

Figure 2-6 Proposed approximated settlement profiles for each clay type

Table 2-1 Normalized coordinates for settlement profiles for soft clay

Clay type	$x=H$	$\delta V=\delta V$max
Soft	0	0.1
	0.425	1
	1	0.05
	1.1	0
Medium	0	0.1
	0.425	1
	1	0.1
	1.2	0
Stiff	0	0.45
	0.5	1
	1	0.1
	1.2	0

2.3.1.2 Verification Analysis of Settlement Profiles

The efficacy of the approximated settlement profiles developed for this study was evaluated by comparing the normalized profiles with normalized data from case histories not used in the development of the Bryson et al. (2018) lateral deformation profiles. Table 2-2 presents the case histories used for verification. Note that the presented case histories correspond to diaphragm walls as well was most of the cases of Bryson et al. (2018). However, the proposed approach is not limited to these types of walls. Characteristics of the case history excavations are presented in Table 2-3.

Figure 2-7 shows the measured settlement profiles for the three strength classifications. The proposed profiles were defined based on relatively homogeneous soil conditions without significant ground improvement. For cases in which the excavated soil is layered due to stratification or ground improvement, it is suggested that an equivalent undrained shear strength, $s_{u(eq)}$, as given by Peck (1969), be applied to the proposed methodology.

For most of the case histories, the approximated normalized settlement profiles match the measured profiles very well. In a few cases, there are slight differences between the approximated and measured profiles. In those cases, the proposed profiles represent an envelope to the measured movements. Regardless, the simplified settlement profiles are considered satisfactory to estimate the ground distortions caused by a deep excavation.

Table 2-2 Case histories used for verification of the proposed settlement profiles

Soil type	Case ID	Description	Wall type	Reference
Soft	So1	Shanghai World Finance Center (SWFC) building	Diaph	Tan and Wang (2013)
	So2	One Museum Park West building	Diaph.	Finno et al. (2015)
	So3	Metropolitan area of Shanghai	Diaph.	Tan and Wei (2012)
Medium	M1	Metro station in Shanghai	Diaph.	Liu et al. (2005)
	M2	Osaka Subway Line No. 8	Diaph.	Konda et al. (2008)
	M3	Bangkok MRT underground railway	Diaph.	Likitlersuang et al. (2013)
Stiff	St1	Suzhou broadcasting and television station	Diaph.	Tan et al. (2015)

Note: Diaph. = diaphragm wall; and MRT = metropolitan rapid transit.

Table 2-3 Case history data for comparison with the proposed settlement profiles.

Case ID	H (m)	He (m)	B (m)	s_v[a] (m)	s_h[a] (m)	su (kPa)	EI[b] (MN-m^2=m)	$\delta_{V(max)}$(mm)
So1	34	17.8	125	4.5	1	20	25,000	64
So2	24	17.9	47	2.75	1	25	2,500	62.1
So3	34.7	16	20	3.5	3	20	1,280	25
M1	28	15.5	17.4	2.9	3	30	540	12.4
M2	26.3	21.5	16.3	2.5	2.5	34	399	23.9
M3	27.9	20.9	13	6.5	1	30	2,333	27
St1	35	15.6	125	4.8	6.5	50	3,500	21

[a]1 m assumed for slabs.

[b]Concrete modulus assumed as 30 GPa.

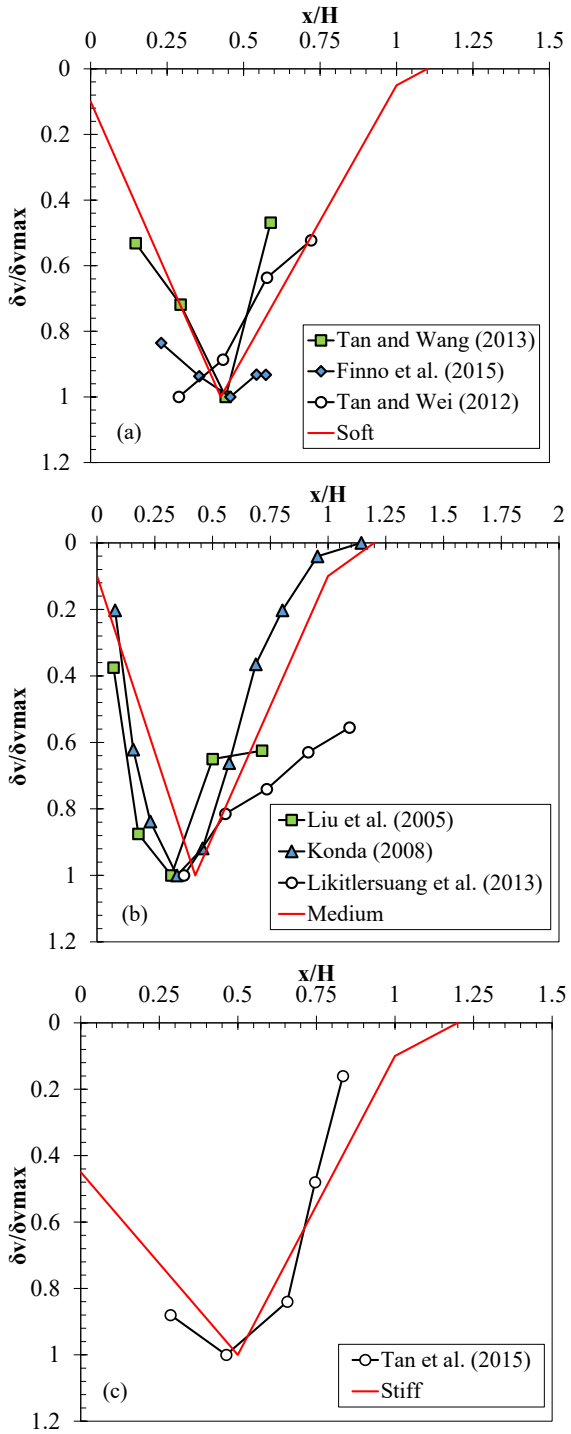

Figure 2-7 Comparison of the proposed normalized settlement profiles with case history data for: (a) excavations in soft soils; (b) excavations in medium soils; and (c) excavations in stiff soils in medium soils; and (c) excavations in stiff soils.

2.3.2 Estimation of Lateral Ground Movements

Lateral movements of an excavation support wall are influenced by several factors such as the soil strength and stiffness parameters, retaining system stiffness, groundwater conditions, and construction methods. For the assumption of a frictionless wall, lateral ground movements at the excavation face are equaled to the lateral support wall movements. Clough et al. (1989) developed an approach to estimate maximum lateral wall movements as functions of the factor of safety against basal heave at the bottom of the excavation and the effective stiffness of the support system. Although the Clough et al. (1989) approach is routinely used to estimate the maximum wall movements, it was developed from a two-dimensional plane strain finite-element analysis. Therefore, Clough et al. (1989) approach does not consider the three-dimensional nature of excavations, which can play an important role in the general performance of an excavation support system (Finno et al. 2007; Li et al. 2015; Bahrami et al. 2018). Bryson and Zapata-Medina (2012) presented the relative stiffness ratio based on three-dimensional finite-element analysis. This parameter is an improved representation of the stiffness of the excavation support parameters of the excavated soil. The relative stiffness ratio is given by

$$R = \frac{E_s}{E}\frac{s_h s_v H}{I}\frac{\gamma_s H_e}{s_u} \tag{2-9}$$

where $R =$ relative stiffness ratio; $E_s =$ initial tangent modulus of the soil; $E =$ Young's modulus of the support wall; $s_v =$ average vertical support spacing; $s_h =$ average horizontal support spacing; $H =$ total embedded depth of the wall; $I =$ moment of inertia per unit length of the wall; $\gamma_s =$ average unit weight of the soil; $H_e =$ excavation depth; and $s_u =$ undrained shear strength of the soil at the bottom of the excavation. The methodology proposed in this study will use Eq. (2-9) to determine the required wall section that complies with the damage requirements defined by the wall designer. From this equation the required bending stiffness of the wall can be determined as

$$EI_{req} = \frac{E_s s_h s_v H}{R_{\text{req}}} N_s \tag{2-10}$$

where $N_s =$ stability number defined as $N_s = \gamma_s H_e / s_u$; and R_{req} corresponds to the required relative stiffness ratio of the wall, which is determined based on the allowable ground deformation. It is clear from Eq. (2-10) that the relationship between the required stiffness of the wall and R_{req} is inversely proportional for a given excavation (i.e., given s_v, s_h, H).

Figure 2-8 shows the relationship among the maximum lateral ground deformations, the factor of safety against basal heave, and the relative stiffness ratio. The factor of safety used by Bryson and Zapata-Medina (2012) is a modified version of the Terzaghi (1943) equation reported by Ukritchon et al. (2003) that includes the wall embedment effects and given as

$$FS = \frac{N_c s_u + \sqrt{2} s_u \left(\frac{H}{B}\right) + 2 s_u \left(\frac{D}{B}\right)}{\gamma_s H_e} \tag{2-11}$$

where $N_c =$ bearing capacity factor at the bottom of the excavation; $D =$ depth of embedment below the excavation bottom; and $B =$ width of the excavation; the other terms were previously defined.

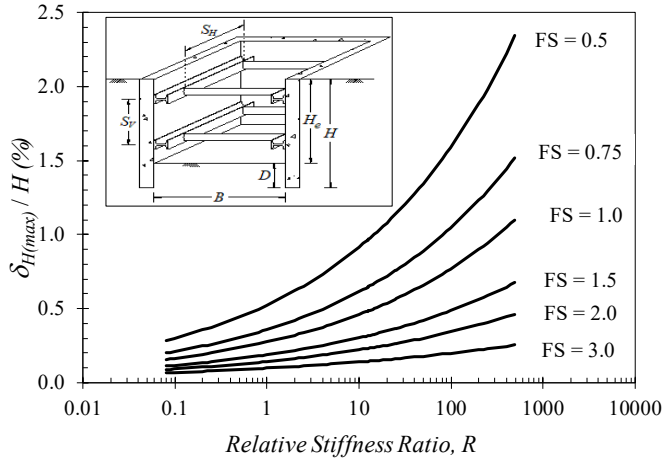

Figure 2-8 Relative stiffness ratio design chart. (Adapted from Bryson and Zapata-Medina 2012.)

Maximum ground settlement can be related to the maximum horizontal wall movement using the empirical relationship proposed by Bryson and Zapata-Medina (2012), given as

$$\frac{\delta_{H(\max)}}{H} = 0.9221\left(\frac{\delta_{V(\max)}}{H}\right)^{0.7696} \tag{2-12}$$

Eq. (2-12) links estimates of horizontal wall deflection to excavation-related ground settlement, which in turn are used to estimate ground distortions. Given that cracking in infill walls of adjacent infrastructure can be estimated from ground distortions [see Eq. (2-1)], Eq. (2-12) ultimately provides a means to design an excavation support system to limit adjacent damage.

2.4 DEPTH OF EMBEDMENT CONSIDERATIONS

The embedment of an excavation retaining wall is designed based on static equilibrium and basal heave considerations. Although Eq. (2-11) considers depth of embedment in assessing basal stability, the equation implicitly assumes a rigid wall. Several researchers (Ukritchon et al. 2003; Do et al. 2013; Goh 2017; Sun et al. 2017; Huang et al. 2018) have suggested that basal stability is a function of the soil strength, excavation characteristics, and wall stiffness.

2.4.1 Depth Embedment from Assessing Basal Stability

In this current study, the equation proposed by Ukritchon et al. (2003) was used to analyze the stability of an excavation retaining wall assuming a homogeneous clay deposit. Based on Ukritchon et al. (2003), the factor of safety for basal stability, FS_{BS}, is given by

$$FS_{BS} = \frac{F_1}{F_2} \tag{2-13}$$

where the functions F1 and F2 are defined as

$$\begin{aligned} F_1 &= (2+\pi)\left(\frac{B}{H_e}\right) + b_2 + b_3\sqrt[4]{\frac{M_p}{s_u D^2}}\left(\frac{D}{H_e}\right) \\ &+ \left(\frac{M_p}{s_u D^2}\right)\left(\frac{D}{H_e}\right)^2\left\{c_2\left(\frac{D}{H_e}\right)\left(\frac{H_e}{B}\right)^2 + c_3\sqrt{\frac{D/H_e}{H_e/B}}\right\} \end{aligned} \tag{2-14}$$

$$F_2 = \frac{\left(\frac{B}{H_e} + a_2 + \sqrt{\frac{M_p}{s_u D^2}} \left(\frac{D}{H_e} \right) \left\{ a_3 \left(\frac{D}{H_e} \right) + a_4 \sqrt{\left(\frac{D}{H_e} \right)} \right\} \right)}{\left(\frac{\gamma_s H_e}{s_u} \right)} \tag{2-15}$$

where M_p = plastic bending moment of the wall; and a_i, b_i and c_i = regression coefficients determined by Ukritchon et al. (2003) from a regression analysis of numerical and case history data. The regression coefficients of Eqs. (2-14) and (2-15) are given in Table 2-4.

Table 2-4 Regression coefficients for Eq. (2-14) and Eq. (2-15)

Coefficient	Value
a1	0.608
a2	0.208
a3	−0.224
b2	6.102
b3	2.082
c2	0.147
c3	0.172

Source: Data from Ukritchon et al. (2003).

Note that to evaluate the basal stability using Eq. (2-13), the plastic bending moment of the wall, M_p, is required. However, this parameter is not known a priori. For this study, M_p was approximated considering the bending moments that develop below the lower support of the wall. Assuming the earth pressure distribution as shown in Figure 2-9, the plastic bending moment is given by

$$M_p = \left(\gamma_s H_e - 4 s_u \sqrt{1+\alpha} \right) \cdot D \cdot \left(\frac{D}{2} + H_{lowest} \right) + k_{app} \gamma_s H_e \frac{H_{lowest}^2}{2} \tag{2-16}$$

where α = wall adhesion factor assumed as $2/3$ (Ou 2006); H_{lowest} = distance from the lowest support to the bottom of the excavation; and k_{app} = coefficient of the apparent earth pressure diagram; the other variables were defined previously. Using Eq. (2-16) to obtain M_p assumes that the final designed wall will be adequate to resist the calculated M_p.

2.4.2 Depth Embedment from Assessing Moment Equilibrium

The embedded length of a retaining wall was also analyzed by considering static equilibrium below the lowest support level. It is assumed that the wall is free to rotate about the lowest support level. In this study, the active pressure above the excavation bottom is represented by the apparent earth pressure distribution. The apparent earth pressures were calculated based on the recommendations given by Sabatini et al. (1999). Below the excavation bottom, the active and passive pressures were represented by classical Rankine earth pressures linearly varying with depth. Figure 2-9 shows the pressure distribution assumed for a typical excavation support wall. From the figure, the factor of safety based on moment equilibrium for the embedded portion of the wall can be defined as

$$FS_{ME} = \frac{P_p d_p + M_{all}}{P_a d_a} \tag{2-17}$$

where $P_a =$ resultant force of the active pressures below the lowest support (including apparent earth pressure); $P_p =$ resultant force of the passive pressures below the excavation grade; $d_p =$ distance from P_p to the lowest support; $d_a =$ distance from P_a to the lowest support; and $M_{all} =$ allowable bending moment of the retaining wall. According to Ou (2006), $FS_{ME} = 1.2$ is required when the allowable bending moment of the wall is ignored $\left(M_{all} = 0\right)$; otherwise, $FS_{ME} = 1.5$.

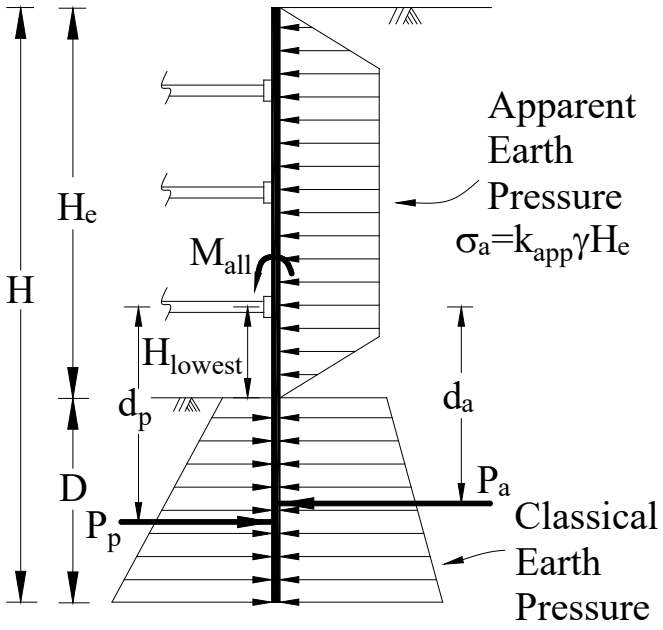

Figure 2-9 Assumed pressure distribution for the excavation support wall.

Based on the previously defined factors of safety, for several uniform soil conditions, the required embedment depth, D, was calculated such that the minimum factor of safety against stability heave or moment equilibrium was 1.5. The results of this calculation are shown in Figure 2-10 for different ratios of width-to-height of the excavation, B/H_e. The required depth of embedment is presented for a given stability number. For calculating the depth of embedment based on assessing the basal stability, the distance H_{lowest} was assumed as 20% of the height of the excavation, H_e.

As seen in Figure 2-10, the required depth of embedment based on moment equilibrium does not vary with the width of the excavation. However, the required embedment based on basal stability is sensitive to the variation of the width. As the B/H_e ratio increases, the required embedment, D, increases. In some cases, the calculations would suggest that the required embedment is as much as twice the excavation depth for a factor of safety of 1.5. However, this is considered to be impractical. Thus, it is suggested that the depth embedment be limited to the excavation depth (i.e., $D = H_e$).

For values of N_s less than 4, the factor of safety based on moment equilibrium governs the selection of the embedment depth when the B/H_e ratio is less than 4. The

required embedment tends to zero when N_s approaches 2.0. For large values of the stability number $(N_s > 4)$, in most of the width-to-height of the excavation ratios shown in the figure, the required depth of embedment will be governed by basal stability considerations. In cases where $B/H_e \geq 5$, a stability number less than 4 $(N_s < 4)$ determines the selection of the depth of embedment. For excavations in which the given characteristics do not converge to any of the observed tendencies of Figure 2-10, ground stabilization is suggested to conduct the excavation.

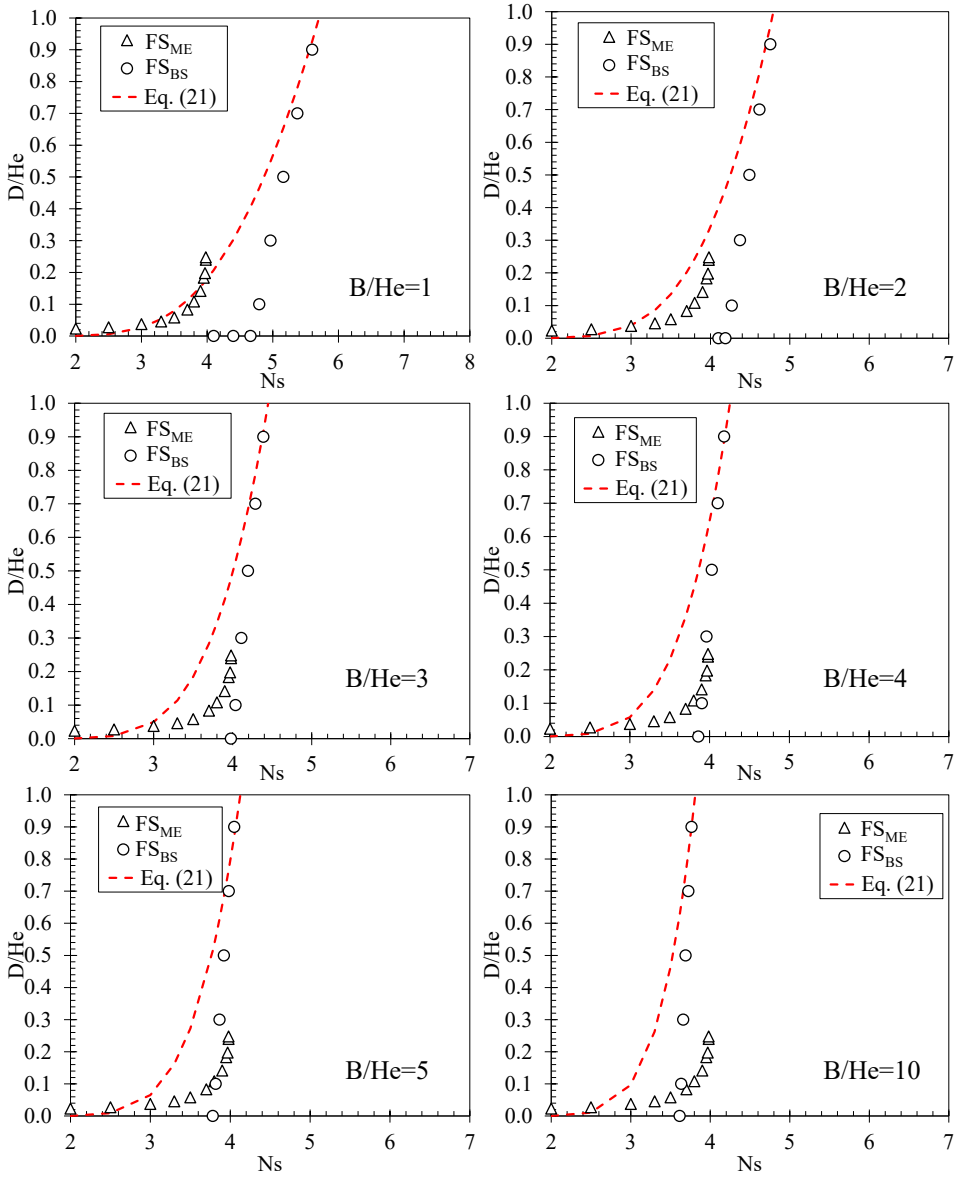

Figure 2-10 Normalized depth of embedment as a function of the width of the excavation and the stability number, Ns

A series of curves were fitted to the data points obtained from the previous embedment depth analysis for the different plots of B/H_e. The curves for each B/H_e was represented by a shifted exponential function given in natural logarithmic form as

$$\ln\left(\frac{D}{H_e}\right) = a - \frac{b}{N_s} \tag{2-18}$$

Table 2-5 presents the estimated a and b coefficients from the fitting process. An additional regression analysis was performed on the data by plotting the a and b coefficients as a function of the B/H_e ratio. This analysis is shown in Figure 2-11.The relations established for the a and b coefficients are given as

$$a = 2.0104\ln\left(B/H_e\right) + 4.0222 \tag{2-19}$$

$$b = 4.35\ln\left(B/H_e\right) + 22.949 \tag{2-20}$$

These relations are valid for B=He ratios ranging from 1.0 to 10. Substituting Eqs. (2-19) and (2-20) into Eq. (2-18) yields an expression for the normalized depth of embedment given as

$$\frac{D}{H_e} = 55.825 \cdot \exp\left[2.0104\ln\left(\frac{B}{H_e}\right) - \frac{1}{N_s}\cdot 4.35\ln\left(\frac{B}{H_e}\right) - \frac{1}{N_s}22.949\right] \tag{2-21}$$

Eq. (2-21) is represented in Figure 2-10 as a dashed line. As seen in the figure, Eq. (2-20) produces a satisfactory performance with respect to the selected data also shown in the figure. As previous discussed, Eq. (2-21) produces a minimum factor of safety of 1.5 against stability heave or moment equilibrium.

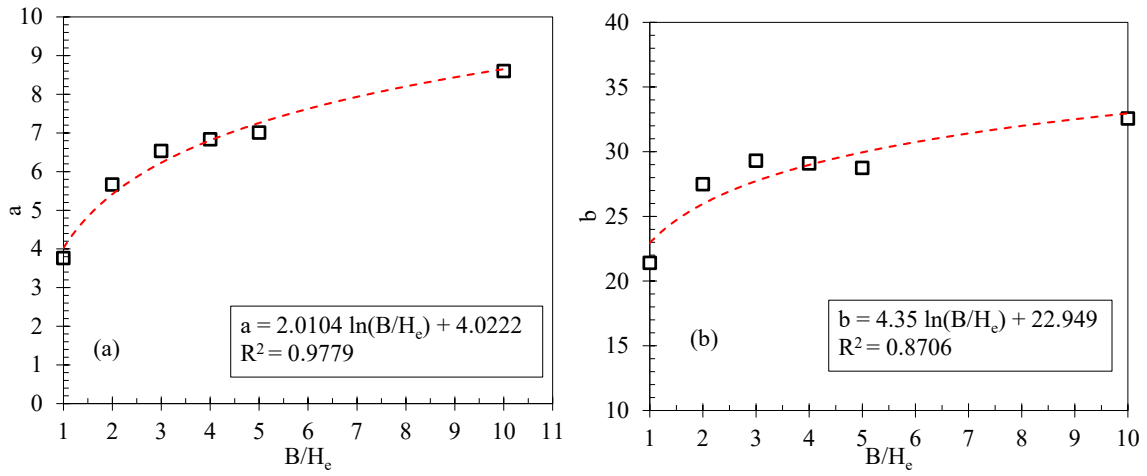

Figure 2-11 Fitting coefficients for the normalized depth of embedment expression: (a) relation for the a-parameter; and (b) relation for the b-parameter

Table 2-5 Fitting parameters for the normalized depth of embedment relationship

$B=H_e$	a	b
1	3.761	21.400
2	5.660	27.478
3	6.531	29.289
4	6.834	29.080
5	7.007	28.738
10	8.595	32.550

2.5 DESIGN OF STRUTS AND WALES

At this point in the design process, the wall component of the excavation support system has been defined based on the deformation and damage requirements. The remaining components of the support system that must be designed are the wales and struts. Traditionally, these components are designed based on loads calculated from apparent earth pressures. In this study, it is proposed to design these components based on the flexural capacity of the required wall section M_{max}. The flexural capacity of an excavation retaining wall is computed based on reinforced concrete theory for concrete wall or using the section modulus for a steel wall. In this study, only the capacity of sheet-pile sections will be considered. Assuming a distribution of bending moments along the wall as shown in Figure 2-12, a uniform load p that will correspond to the flexural capacity of the wall is given by

$$p = \frac{8 \cdot M_{\max}}{s_v^{\,2}} \tag{2-22}$$

Design of the struts and wales with this load may result in excessively conservative sections. The reason for this overestimation lies in the fact that these components of the support system are typically designed based on apparent pressures that depend only on the properties of the excavated soil. However, the load, p, calculated with Eq. (2-22), depends on its flexural capacity $M_{\max}$, which depends on the section of the wall determined from serviceability requirements.

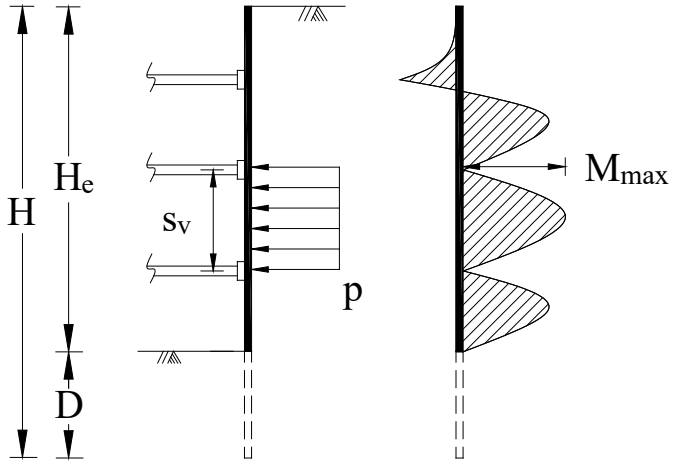

Figure 2-12 Assumed bending moment diagram for the excavation support

To illustrate the overestimation of the calculated load p (function of $M_{\max}$), from Eq. (2-22), several forward and backward calculations of the maximum bending moment on the wall were computed based on the parameters provided in Table 2-6. In the forward calculation, for given soil properties represented by the stability number, the apparent earth pressures were calculated using a traditional approach such that $p = k_{app}\gamma_s H_e$. Sabatini et al. (1999) recommended a coefficient of $k_{app} = 0.22$ for the apparent pressure diagram in cases in which the stability number is between 4 and 5.14 (Figure 2-9). However, a constant value of $k_{app} = 0.30$, corresponding to the average recommend for stiff clays, was considered for stability numbers less than 5.14. For cases in which the stability number was greater than 5.14, the Henkel equation as presented by Sabatini et al. (1999) was applied. Afterwards, the maximum moment was calculated using Eq. (2-22) solving for

M_{max}. Note that the value 5.14 corresponds to the bearing capacity factor for a perfectly smooth footing assumed by Terzaghi (1943).

Table 2-6 Parameters for the parametrical analysis for the reduction factor, ξ.

Parameter	Range
N_s	2.5 to 8
H_e	9 m to 15 m
s_h/s_v	1 to 2
B/H_e	1 to 2

In the backward calculation, the system stiffness ratio, R, was defined, then the required stiffness of the wall was calculated from Eq. (2-10). The required inertia and the section modulus of the wall component were selected for steel wall sections, then the maximum allowable moment was calculated based on a maximum bending stress, F_b, limited to $0.6F_y$, where F_y is the yielding stress of the steel.

The results based on the apparent earth pressures (Sabatini et al. 1999) are indifferent to those based on the relative stiffness ratio, R. However, for the results based on R, there is a significant variation of the maximum flexural capacity of the wall. For cases where R is small (e.g., stiff walls), the moment capacity must be high to limit the excavation-induced moments. Under the same conditions, the apparent earth pressures do not reflect the serviceability requirements of the excavation support system.

Figure 2-13 shows the variation of the maximum bending moment as a function of the relative stiffness ratio. As expected, an increase on R corresponds to a decrease in the flexural capacity of the walls because these walls are more flexible. Based on the uniform load p determined from the flexural capacity of the wall, the design of the other structural components of the support system will be overestimated. Note that in Figure 2-13, the bending moment on the wall from the apparent earth pressures (i.e., horizontal lines) in most of the cases is well below the bending moment (i.e., flexural capacity) from the relative stiffness ratio R, represented by the different markers.

Consequently, a reduction factor applied to the uniform load p is necessary to obtain loads comparable to those calculated using apparent earth pressures. The wall design

is based on the deformation limits defined by the designer. Then, the design of the wall support system (i.e., struts and wales) is based on the characteristics of the wall. In this proposed approach, the design process does not require the calculation of apparent earth pressures.

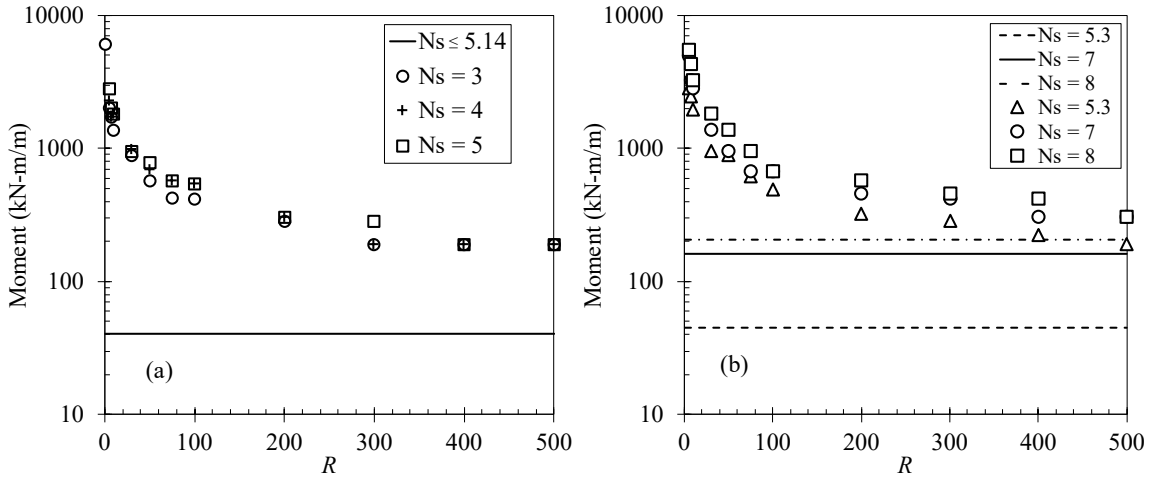

Figure 2-13 Variation of the bending moments for (a) Ns less than 5.14; and (b) Ns greater than 5.14

From Figure 2-13, based on the range of the parameters presented in Table 2-6, Figure 2-14 presents the reduction factor, ξ. As seen from the figure, this factor is a function of R and the stability number of the excavation. Therefore, the equivalent load for the design of the wales and struts is determined by multiplying ξ and p determined from Eq. (2-23) as

$$p_{eqv} = \xi \cdot p \tag{2-23}$$

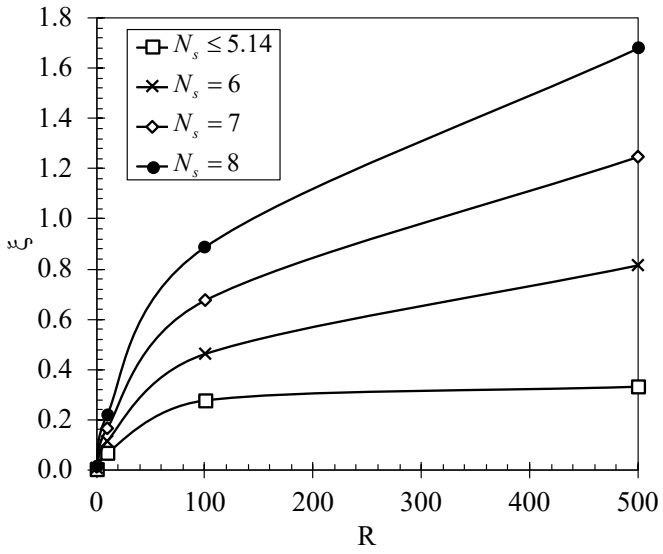

Figure 2-14 Reduction factor, ξ, for the equivalent load to design the wales and struts

The graphic representation of the reduction factor, ξ, shown in Figure 2-14 can be expressed in an equation. Eq. (2-24) condensed the results shown in Figure 2-14. For values of the stability number, N_s, less than 5.14, which corresponds to the separation between soft and medium clays, the reduction factor was approximated as a power function. For stability numbers greater than 5.14, ξ was estimated based on a linear function

$$\xi = \begin{cases} R \le 100 & N_s \le 5.14 \quad 0.0112 \cdot R^{0.6085} \\ & N_s > 5.14 \quad \left(0.0086 \cdot N_s - 0.0329\right) \cdot R^{0.6085} \\ R > 100 & N_s \le 5.14 \quad 0.2201 \\ & N_s > 5.14 \quad \left(0.0004 \cdot N_s - 0.0018\right) \cdot R + \left(0.0741 \cdot N_s - 0.02652\right) \end{cases} \tag{2-24}$$

The wales can be design based on a bending moment using the equivalent load as

$$M_{wale} = \frac{p_{eqv} \cdot {s_h}^2}{12} \tag{2-25}$$

Eq. (2-25) assumes the wale can be represented as a continuous beam, which assumes hinge at the horizontal strut locations. For assumptions of fixed supports at the horizontal strut locations, Fang (1991) recommended a denominator of 10 instead of 12 in the equation. It is up to the designer to decide which condition is more representative of a particular excavation. Finally, the struts can be design based on the determined p_{eqv} and the vertical and horizontal separation. It is noted that the previous development of the

reduction factor, ξ, for the design of the wales and struts is based on sheet-pile walls. To adjust the methodology to concrete walls, further developments are required to relate the maximum bending moment in the section and the required stiffness of the section based on allowable displacements. This development is not included in the presented approach.

2.6 OVERVIEW OF THE DESIGN METHODOLOGY

Figure 2-15 presents the flow chart of the proposed methodology. This approach provides a primary estimation of the wall components based on limiting excavation-related damage in adjacent structures. In the proposed approach, the elements of the excavation support system are designed based on a level of damage in an adjacent structure acceptable by the designer and owner. Implementation of the proposed design methodology is demonstrated using an example presented in the Appendix.

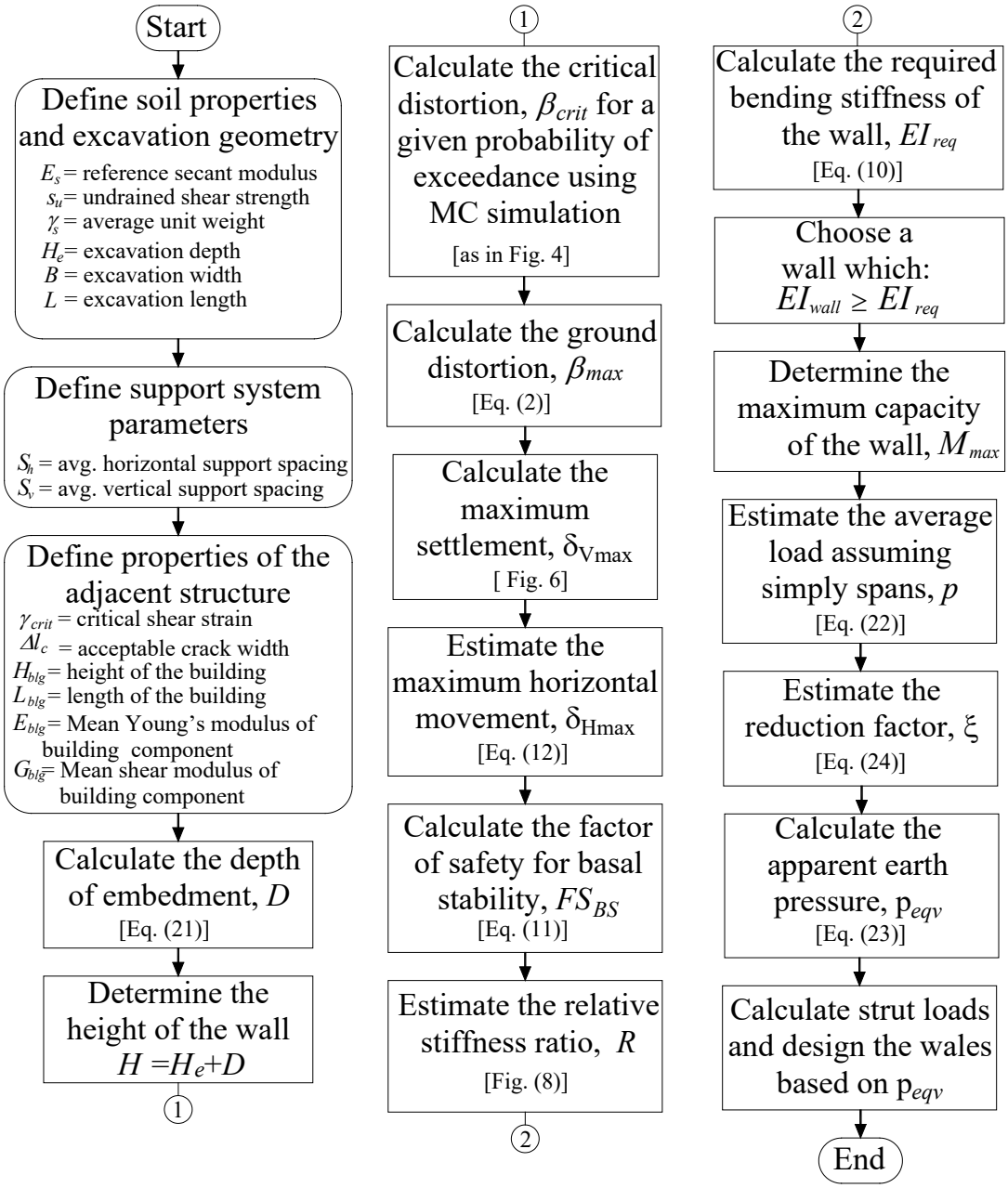

Figure 2-15 Deformation-based design method for deep excavation support system design

2.7 SAMPLE DESIGN TO LIMIT CRACKING IN ADJACENT INFILL WALL

A hypothetical excavation is used to illustrate the methodology. Figure 2-16, Table 2-7 and Table 2-8 present the excavation geometry and soil properties used in this example, as well as the properties of the building section.

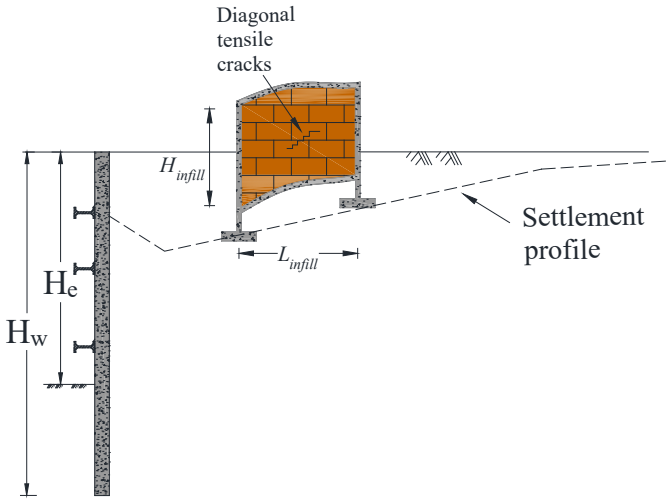

Figure 2-16 Schematic excavation and adjacent building for the example of the proposed methodology

Table 2-7 Excavation and soil properties for the example of the proposed methodology

s_u	γ_{eq}	H_e	B	E_{50}	s_h	s_v
42	18.1	10	25	12,476	5	2.5

Table 2-8 Properties of the building section for the example of the proposed methodology

E_m (GPa)	G_m (GPa)	E_c (GPa)	G_c (GPa)	H_{infill} (m)	L_{infill} (m)	γ_{crit} (%)
12.4	4.96	24.8	10.3	3.86	7.72	0.11

For the selection of the vertical strut spacing, s_v, typical values range between 2.5 and 6 m. However, larger separations can also be observed (Long 2001). In the context of this study, it is recommended to limit the horizontal and vertical separations to the previous range. Otherwise, the procedure may result in wall sections that can be impractical. The following steps are used to design the excavation support system using a deformation-based design methodology that will limit damage:

1. Define the accepted crack width

In this example, the building owner is willing to damage corresponding to a crack width less than or equal to 4 mm. $\Delta l_c = 4mm$ corresponds to slight damage according to Boone et al. (1999). Burland et al. (1977) presented a classification of damage as: Very slight $\left(\Delta l_c \le 1mm\right)$, slight $\left(\Delta l_c \le 5mm\right)$, moderate $\left(\Delta l_c \le 15mm\right)$, severe $\left(\Delta l_c \le 25mm\right)$, and very severe $\left(\Delta l_c > 25mm\right)$.

2. Calculation of the depth of embedment.

From the properties of the excavated soil, the stability number is $N_s = 4.31$; $B/H_e = 2.5$. Using Eq. (2-21), $D = 6.8m$. Therefore, the height of the wall will be $H = 16.8m$.

3. Calculation of the critical distortion

Using the laminate beam approach and the MC simulation for a single infill wall with no openings bounded by a strip foundation and a beam, the critical distortion was estimated as $\beta_{crit} = 0.00139$ for a probability of exceedance of 50%. This value corresponds to the mean material parameters.

4. Calculation of the ground distortion

The ground distortion that will cause the accepted crack width was calculated based on Eq. (2-2). In this case, η was assumed as 1.0. The properties of the wall were taken from Table 2-8, $\beta_{\max} = 0.002086$.

5. Calculation of the maximum induced settlement

To calculate the maximum induced settlement that corresponds to the distortion βmax, it is necessary to know the location of the building or portion of the building under consideration with respect total height of the wall, as shown in Figure 2-6. Then, the slope of the settlement profile can be determined (i.e., based on the coordinates from Table 2-1 or Figure 2-6 for soft, medium, and stiff soils) corresponding to that location. It is assumed that $\beta_{\max}$ is equal to the previously determined slope. Assuming that the building is in the sagging portion of the settlement profile at a distance greater than the distance to the maximum induced settlement. This location corresponds to the second slope of the settlement profile shown in Figure 2-6, from which the coordinates can be taken. The maximum settlement that represents the calculated distortion, $\delta_{V\max} = \beta_{\max}\left(0.575H/0.9\right)$ was determined as $\delta_{V\max} = 30.65mm$.

6. Calculation of the maximum normalized horizontal displacement

Based on the calculated maximum settlement, from Eq. (2-12), the normalized horizontal displacement will be $\left(\delta_{H\max}/H\right)(\%) = 0.25$.

7. Calculation of the relative stiffness ratio

Using the chart developed by Bryson and Zapata-Medina (2012) (Figure 2-8), for a factor of safety against basal heave of $FS_{BH} = 1.5$ from Eq. (2-11), the relative stiffness ratio was determined as $R_{req} \approx 4.5$.

8. Calculation of the required bending stiffness of the wall

From Eq. (2-10), the required bending stiffness of the wall was determined as $EI_{req} = 2,508,977\, kN \cdot m^2/m$.

9. Calculation of the required inertia of the wall

Assuming a sheet-pile section of the wall with $E = 200GPa$, the required inertia of the retaining wall will be: $I_{req} = 1,254,488\, cm^4/m$.

10. Selection of the wall section

Choosing a wall section such that $I_{dgn} > I_{req}$. Selecting a Nucor Skyline steel Pipe-Z combined wall system PAZ66/AZ38 with a moment of inertia of $I_{dgn} = 1,473,880\, cm^4/m$. The section modulus for this sheet pile is $S_{dgn} = 17,584\, cm^3/m$.

11. Average uniform loading

The flexural capacity of the wall was determined as $M_{\max} = 0.6F_y \cdot S_{dgn} = 4,378.4\, kN \cdot m/m$. Assuming simply supported spans, the average uniform load that results in the capacity of the wall will be: $p = 5604.4\, kN/m/m$ from Eq. (2-22).

12. Equivalent load and wale design

An equivalent load for the design of the wales and struts can be calculated as $p_{eqv} = 263.4\, kN/m/m$ using $\xi = 0.047$ from Eq. (2-24). For this load a section W 30×191 is selected for the wale. This same load is used for the design of the struts.

CHAPTER 3

GEOPHYSICS BASED MODEL FOR DETERMINING EFFECTIVE STRESS IN SOFT SOILS

3.1 INTRODUCTION

Geophysical measurements such as seismic wave velocities are routinely used in geotechnical investigations. In addition, geophysical methods are a valuable engineering tool for subsurface characterization. In recent decades, several researchers have used geophysical data to predict the subsurface response (Lin et al. 2017; Crawford et al. 2019; Pasierb et al. 2019; Imani et al. 2021) and to estimate material parameters such as unit weight (Moon and Ku 2016) , drained and undrained shear strength and preconsolidation pressure (Guadalupe et al. 2013; Moon and Ku 2018; Yoo et al. 2018; Duan et al. 2019; Trafford and Long 2020).

Unlike traditional subsurface exploration techniques that involve drilling and sampling at localized depths within a soil mass, geophysical surveys, such as shear wave velocities, provide a larger observation scale (Gouveia et al. 2019). The subsurface investigation problem is particularly exacerbated for a highly variable deposit. In-situ geophysical testing can minimize other difficulties associated with traditional exploration techniques, such as time consumption, material disturbance, equipment accessibility, and high cost (Mohamad Nor et al. 2011; Muttashar et al. 2019). Moreover, spatial and temporal variation of subsurface conditions can be obtained from geophysical methods with the advantage that these techniques are readily adapted to remote sensing platforms (Calamita et al. 2019; Whiteley et al. 2021).

Consolidation processes are commonly encountered in geotechnical engineering practice involving soft foundation soils. Laboratory testing on several undisturbed samples is the usual procedure to evaluate settlements associated with consolidation. For complex environments, this approach can lead to an unclear picture of the compressional behavior of the site in question. Field geophysical measurements such as shear wave velocities can provide a more comprehensive approach to obtaining information about larger sub-surface areas (L'Heureux et al. 2013). The variables involved in consolidation mechanisms such as void ratio (e), current stress state and stress history (i.e., overconsolidation ratio (OCR))

also affect the shear wave propagation through a material (Hardin and Richart 1963; Houlsby and Wroth 1991; Santamarina et al. 2001). Based on this link between shear wave velocity and material state, several researchers have estimated consolidation behavior based on shear wave measurements (Mohamad Nor et al. 2011; L'Heureux et al. 2013; Oh et al. 2017; Muttashar et al. 2019).

Consolidation often results in elastic deformations for overconsolidated soils (OCR>1.0), plastic deformations for normally consolidated soils (OCR=1.0), or a combination of both deformations for applied stresses above the preconsolidation pressure of the soil. Previous studies divided shear wave velocities during consolidation into two different responses depending on the stress history of the soil, overconsolidated or normally consolidated soils (L'Heureux et al. 2013; Oh et al. 2017). Muttashar et al. (2019) used a monotonic relationship that captures both elastic and plastic deformations. However, the stress history of the material was not investigated in this formulation. From a survey of the available literature, a unified approach that relates shear wave measurements with consolidation pressures and volumetric changes regardless of the stress state of the soil and its stress history has not been developed.

This paper presents an approach to estimating consolidation settlement based on shear wave velocity measurements. A series of isotropic consolidation tests were conducted with one reloading cycle. Data were obtained at very close intervals during testing to gain insights into V_s behavior. The proposed approach is based on a hypoplastic scalar model formulation and a hypothesized relationship between the inverse of the shear wave velocity and the confining pressure of the soil. The developed approach was compared with measured data in the literature under different confining conditions (i.e., oedometer testing. The significance of this study is that the full range of mechanical behavior for soil undergoing consolidation can be predicted at any point in a three-dimensional soil mass using geophysical techniques.

3.2 MATERIALS, SAMPLE PREPARATION AND EXPERIMENTAL PROGRAM

This study used and combined four different source soils to create the samples for testing under isotropic consolidation conditions. Table 3-1 presents the properties of the source soils as well as their classification according to the unified soil classification system

(USCS). The source materials represent fine-grained soil varying from predominately silt samples to predominantly clay samples with liquid limit ranging between 28.2% and 64.3%, and plasticity index varying between 8.5% and 30%. Eight different soils were selected for the testing program by combining the source soils or using them as independent materials.

Table 3-1 Index properties of the source soils

Parameter	Davies county	Henderson county	Fayette county	Lee county
Gs	2.63	2.69	2.86	2.7
LL (%)	31	30	68.6	64
PI (%)	22	20.5	42.8	36.3
PF (%)	60	75.5	64	52
USCS	CL	CL	CH	MH

*Gs= Specific gravity; LL= Liqui limit; PI= Plasticity index; PF=Percentage of fines (% passing #200 sieve)

Table 3-2 presents the index properties of the eight different soil types. In all the materials, the percentage of fines was greater than 50%, and the maximum clay and silt content were 45.3% and 66.2%, respectively. Figure 3-1 shows the grain size distribution of the tested soils. These soils represent an ample range of fine-grained materials (Figure 3-1). Two samples were created for testing from each of the eight soils. A total of 16 samples were prepared using a variation of the resedimentation method (Germaine and Germaine 2009; Schneider et al. 2011). Instead of using a constant load to consolidate the soil to a specific preconsolidation pressure, the soil samples were consolidated by a downward displacement of a steel plunger attached to a load frame through a plastic mold containing the soil.

The preparation process of each sample started by mixing a known mass of dry soil with tap water to create a uniform slurry. The percentage of water used in the mixture was about two times the liquid limit of the soil. The mixture was poured into a split plastic mold between porous stones and filter papers. Then, the slurry was compressed at a very low displacement rate (0.009 mm/min). The target height of each sample was determined based on a dry unit weight of 15.7 kN/m^3. The main advantage of the used procedure is that samples were created with a comparable initial density. However, the disadvantage of this

procedure is that the preconsolidation pressure of the samples could not be controlled. The previous procedure is stopped when the predefined height of the sample is reached.

Table 3-2 Index properties of the 8 materials used in this study

Soil type ID	Fines (%)	Clay (%)	Silt (%)	CF/SF	LL (%)	PI (%)
# 1	75.5	9.3	66.2	0.140	30.0	20.5
# 2	60	11.5	48.5	0.237	31.0	22.0
# 3	52	26.2	25.8	1.016	64.0	36.6
# 4	64	45.3	18.7	2.425	68.6	42.8
# 5	52	14.4	37.6	0.381	45.2	26.6
# 6	51	7.2	43.8	0.164	31.5	20.8
# 7	56	24.5	31.5	0.777	50.0	32.6
# 8	52	19.4	32.6	0.597	43.5	29.1

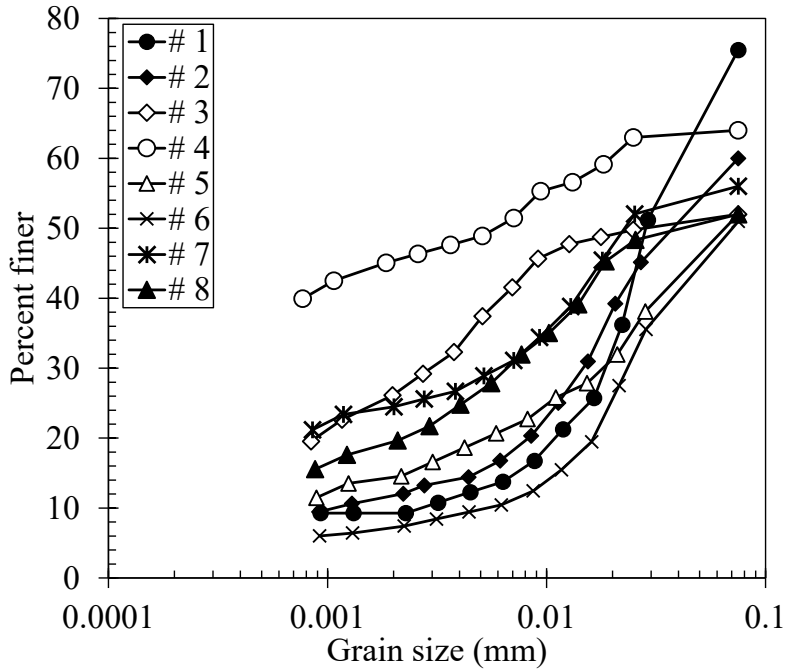

Figure 3-1 Grain size distribution for soils used in study

A triaxial test apparatus was used throughout this study. Shear waves through the samples were generated and received using bender elements (BEs) (Shirley and Hampton 1978). These piezoelectric elements were installed in the top cap and pedestal of the triaxial testing equipment provided by GDS (GDS-Instruments 2010). In addition to the BEs, the equipment included a signal conditioning and control box and the computer software to trigger the BEs. The length and the thickness of the bender elements were 11.6 mm and

1.8 mm, respectively. Figure 3-2 shows the BEs attached to the triaxial equipment at the top cap and pedestal. All the shear waves from this study were propagated in the vertical direction with horizontal polarization.

To determine V_s using bender element tests, two measurements are required: the travel distance and the travel time (Viggiani and Atkinson 1995; Brignoli et al. 1996; Wang et al. 2007). The shear wave velocity is calculated as

$$V_s = \frac{L_{tt}}{t} \tag{3-1}$$

where $V_s =$ shear wave velocity; $L_{tt} =$ wave travel distance; and $t =$ wave travel time. In Eq. (3-1), both right-hand side variables vary with strain. As consolidation advances, L_{tt} was updated based on the measured vertical strain in the sample at the time of generation of shear waves with the BEs. The travel can be estimated based on time or frequency domain methods such as peak-to-peak, cross-correlation, and cross-spectrum (Yamashita et al. 2009). In this study, the travel time was calculated using the cross-correlation method; nonetheless, the peak-to-peak method was used to corroborate these travel times.

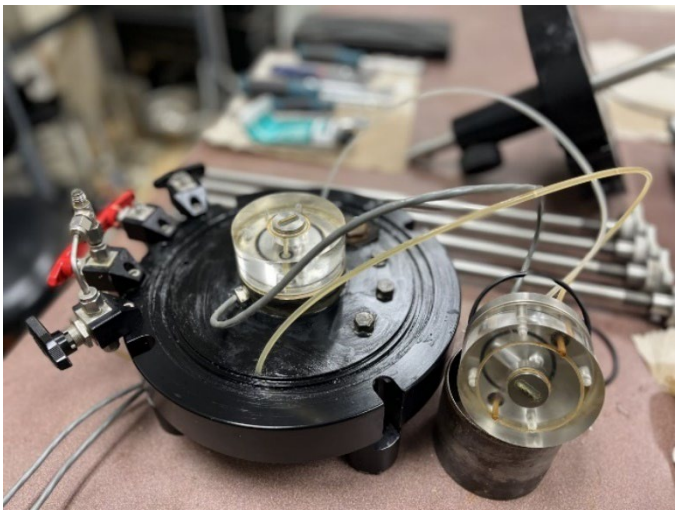

Figure 3-2 Top cap and pedestal of the testing equipment and the attached bender elements

After setting the soil samples in the triaxial cell, the samples were saturated to a maximum back pressure of 551.5 kPa. The B values during the saturation phase of the samples were greater than 0.95 for all samples. Then, the samples were consolidated using

a sequence of loading, unloading and reloading stages. The target mean effective stresses p' for the stages were 172.4 kPa, 68.9 kPa, and 206.8 kPa.

The mean effective stress, p', is defined as

$$p' = \frac{\sigma'_v + 2\sigma'_h}{3} \tag{3-2}$$

where σ'_v and σ'_h are the effective vertical and horizontal stresses, respectively. At the end of each consolidation stage, a hold period of 30 minutes was imposed on the samples. This hold period resulted in a decrease in void ratio in some samples. This decreased in void ratio also resulted in an increase of the measured V_s.

During this experimental program, a single sinusoidal signal was used for the wave propagation. The amplitude of this input wave was set to 14 V. The automation software Microsoft PowerShell (version 5.1) (Microsoft-Corporation 2016) was used to

to control the GDSBES software (GDS-Instruments 2010). This allowed the computer files generated during BE measurements to be saved automatically every trigger interval t_{shot}. The trigger interval t_{shot} in all the conducted test was at most 120 seconds.

To minimize near field effects during bender element testing, it is generally required that the ratio between the wave travel distance (L_{tt}) and the wavelength (λ) to be at least 2 (Sanchez-Salinero 1986; Wang et al. 2007; Airey and Mohsin 2013{Elbeggo, 2019 #10)}. This ratio would imply that a maximum shear wave velocity V_s of approximately 683 m/s could be measured for the excitation frequency of 10 kHz and average L_{tt} of 137 mm at the beginning of consolidation used in this study. Because the calculated V_s were considerably below the previous limit of 683 m/s, near-field effects during testing were expected to be minimum.

Figure 3-3 shows a typical result observed during shear wave propagation in one of the tests conducted in this study. Each output signal corresponds to a given p' shown in this figure. The time to the peak output voltage, t_p, is shown by the closed circles (Figure 3-3). As seen in Figure 3-3, travel times decreased with the increased of the confining stress until $p' = 172\ kPa$. After unloading from the previous p' until a value of $p' = 69\ kPa$, travel times tended to decrease. However, notice that at $p' = 150\ kPa$

the travel time was slightly shorter than at $p' = 172\ kPa$. Because of the greater L_{tt} at $150\ kPa$, V_s at $150\ kPa$ was shorter than at $172\ kPa$. During the reloading portion of the test after $69\ kPa$ until $206.8\ kPa$, the t_p values decreased monotonically.

Signal stacking requires measuring the output signal multiple times and averaging the recorded signals to improve signal-to-noise ratio. Each output signal in Figure 3-3 corresponds to a single generated shear wave; therefore, signal stacking was not performed during travel time calculations. For this reason, the whole output signal in some cases may look slightly slanted. However, a clear distinction of the peak location can be observed in Figure 3-3. Notice also in the figure, that the initial bumps in the output signals correspond to reflected p-waves originated during shear wave generation (Lee and Santamarina 2005). Until $p' = 206.8\ kPa$ inference problems were disregarded as the shear waves were noticeable.

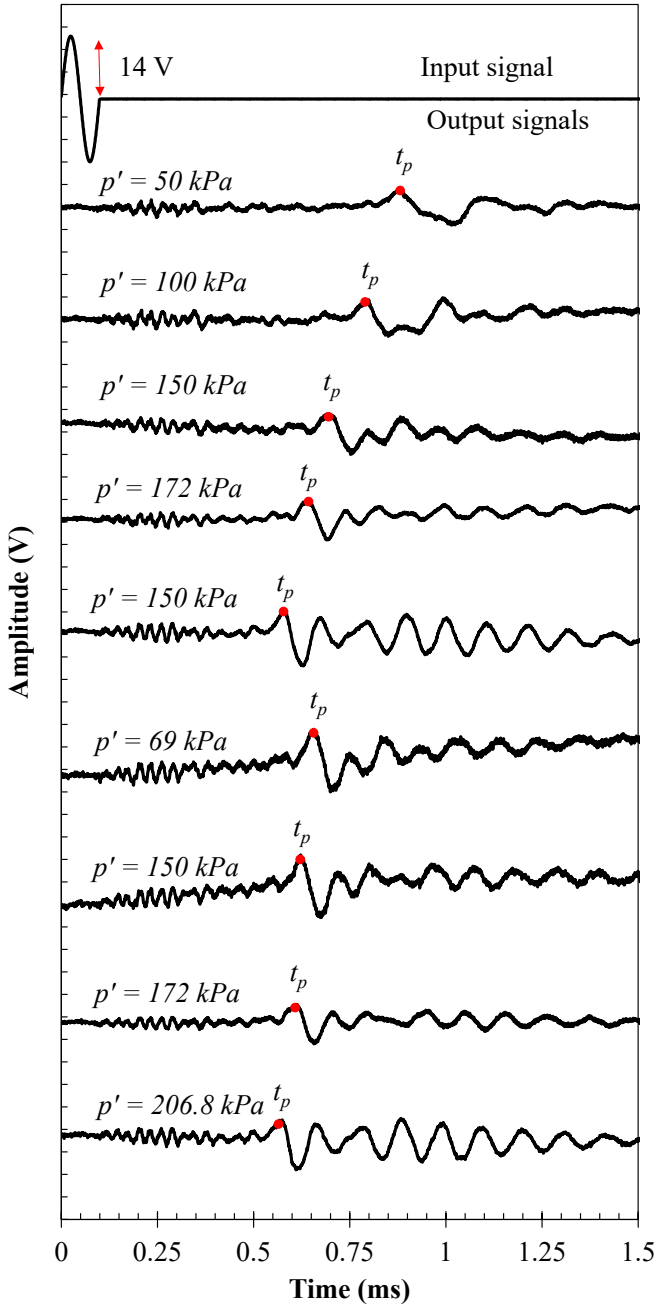

Figure 3-3 Waterfall plot of shear wave signals during consolidation

3.3 SHEAR WAVE VELOCITY MEASUREMENTS DURING CONSOLIDATION

Figure 3-4 presents the consolidation behavior of sample 1-U in terms of void ratio (e) and shear wave velocity (V_s) as a function of the mean effective stress, p'. An identical behavior was observed between e and V_s during the sample's initial loading,

unloading, and reloading. For this sample, the preconsolidation pressure (p'_c) after the resedimentation procedure was around 60 kPa (Figure 3-4 (a)). On the other hand, this pressure does not correspond to a significant change in curvature in the p'-V_s plane (Figure 3-4 (b)). If the same procedure to determine the preconsolidation pressure is used in Figure 3-4 (b), a preconsolidation pressure of 25 kPa is obtained. Other researchers have reported a closer agreement between both ways of determining p'_c (Elbeggo et al. 2019). Generally, a more satisfactory agreement was observed in the other tests conducted in this study.

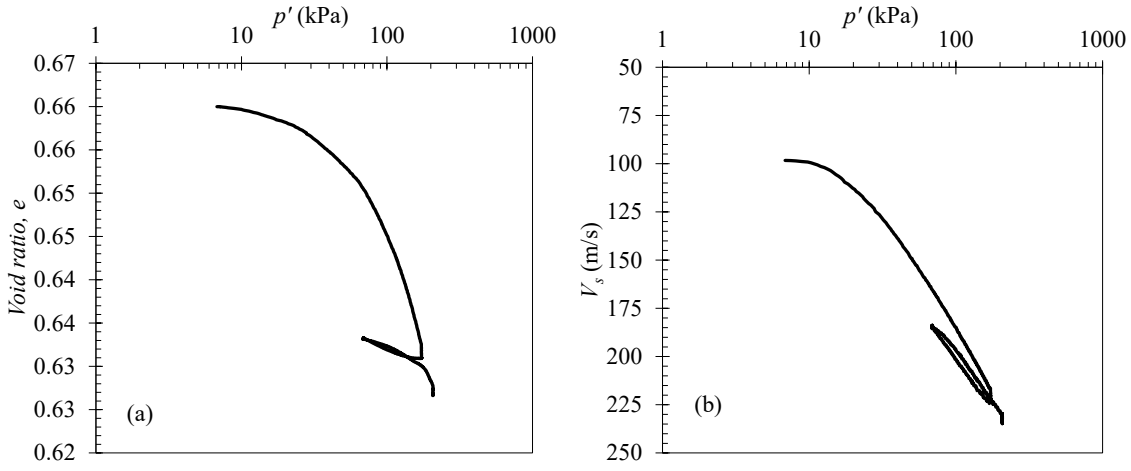

Figure 3-4 Consolidation results for sample 1-U in terms of (a) void ratio and (b) shear wave velocity

Figure 3-5 shows the consolidation results only in terms of p' and V_s for the same sample shown in Fig. 4. Notice that the axes are inverted as V_s is considered an input variable to describe the consolidation process. Figure 3-5(b) shows the shear wave velocities measured during the hold period t_{hold}. For this study, these data were not considered in the approach formulation. From Figure 3-5(a), three distinctive curves are observed. One curve corresponds to the initial monotonic loading until $172.4\ kPa$, the second curve corresponds to unloading until $68.9\ kPa$, and the last curve corresponds to reloading until $206.8\ kPa$. The variation of the shear wave velocity in the normally consolidated portion of the consolidation curve corresponds to the label NCL. The other two curves corresponding to the unloading-reloading cycle of the test are labeled URL and shown more clearly in Figure 3-5 (b). The unloading and reloading curves are very close to each other but are not exactly the same; they form a loop similar to the one observed in

consolidation testing in the p'-e plane. This observation highlights the fact that the relationship between V_s and p' depends on the loading history and direction. This behavior was pointed out by Wang et al. (2021) and previously reported by Choo et al. (2011). They stated that the soil stiffness is also influenced by the directional stress history (e.g., unloading-reloading). For shear waves propagated horizontally, Zhao et al. (2020) also observed this behavior during consolidation in soils rich in kaolinite and illite. For a constant p', the V_s measured in the unloading portion of the tests were slightly bigger than those during reloading.

Although it is recognized the influence of the unloading and reloading directions in V_s, for the purpose of this study, it is considered that the URL portion of the consolidation curve in terms of p' and V_s can be represented by a single curve. The observed behavior for this sample is representative of the results of the other samples. In all cases, the shear wave velocity increased consistently with increasing confining pressures and decreased during the unloading-reloading cycle.

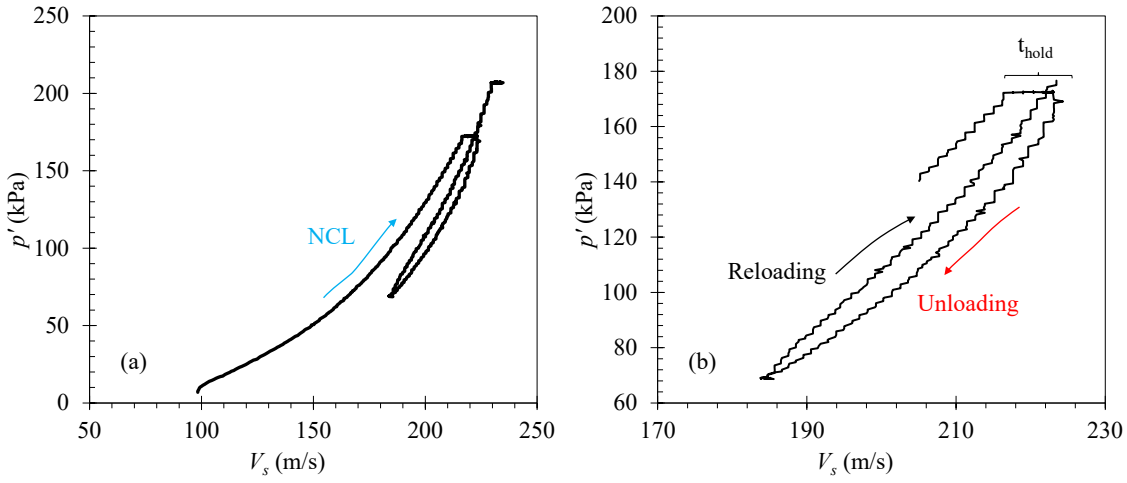

Figure 3-5 Experimental measurements (a) complete consolidation curve; (b) close view at the unloading-reloading cycle for sample 1-U

p' and V_s are typically related through a power function (Santamarina et al. 2001) given as

$$V_s = \alpha(p')^{\beta} \tag{3-3}$$

where α represents the shear wave velocity at mean effective stress of 1 kPa; and β characterizes the sensitivity of the velocity to the stress state (Santamarina et al. 2001{Cha, 2014 #3)}. In this equation (Eq. (3-3)), the influence of other soil parameters such as void ratio, size and roughness of soil particles, and fines content is implicit in the coefficients α and β. It has been recognized that the relationship between the coefficients α and β is inversely proportional Santamarina et al. (2001{Ku, 2017 #2. {Muttashar, 2019 #67) observed that these fitting coefficients tend to be related to material parameters such as clay fraction and liquid limit (LL).

To formulate a V_s-based model for consolidation processes, one may start by defining the confining pressure as a dependent variable. From Eq (3-3),

$$p' = \left(\frac{V_s}{\alpha} \right)^{1/\beta} \tag{3-4}$$

Eq (3-4) must take into consideration that the coefficients α and β vary based on the stress history of the soil. Eq (3-4) represents a straight line in log space. The coefficients $1/\alpha$ and $1/\beta$ represent the intercept and the slope of this straight line. As the whole consolidation curve is divided into two curves (NCL and URL), each of these curves will have a different pair of coefficients representing two lines in log space. The first line in the log space characterizes normally consolidated loading (NCL) until a mean effective stress of 172.4 kPa. The second line (URL) represents reloading from 68.9 kPa to the normally consolidated line. Any additional unloading and reloading cycle, at a different mean effective stress, will also have different coefficients defining an independent line in the log space.

To further analyze the influence of material properties and state conditions (i.e., void ratio) on the coefficients of Eq. (3-3) and Eq. (3-4), the measured data were normalized to the initial stress condition p'_{ini} and its associated initial shear wave velocity $V_{s\,ini}$. The normalization pressure was taken as $p_{ini} = 50\ kPa$. This pressure was selected because it was considered as the lowest threshold at which initial scatter observed in shear wave measurements, V_s, immediately after back-pressure saturation was avoided. Using a normalization approach, the relationship between p' and V_s becomes

$$\frac{p'}{p'_{ini}} = \alpha' \left(\frac{V_s}{V_{s\,\mathrm{ini}}} \right)^{\beta'} \tag{3-5}$$

where α' and β' are also represent the intercept and the slope in the normalized log space of a straight line, respectively. These coefficients also considered the implicit effect of void ratio in shear wave velocities. Figure 3-6 shows the normalized consolidation data corresponding to sample 1-U. The two distinctive segments corresponding to normally consolidated loading (NCL) and overconsolidated loading (URL) are depicted in the figure in the normalized space. Because of the normalization, the coefficient α' in the NCL is expected to be one as it represents the vertical intercept of the power function given by Eq. (3-5) at $V_s/V_{s\,\mathrm{ini}}$ equal to 1, as shown in Figure 3-6. Furthermore, in the URL, the coefficient α' varies based on the response in overconsolidated conditions (i.e., stress history), it is dependent on the preconsolidation pressure. Notice that in Figure 3-6, the URL curve is based on the reloading curve shown in Figure 3-5(b). The p'_c/p'_{ini} point corresponds to the unloading from the mean pressure of 172.4 kPa.

By moving in the URL from the starting point associated with 68.9 kPa at $V_s/V_{s\,\mathrm{ini}} = 1.24$, as the current normalized stress state, p'/p'_{ini}, approaches the normalized preconsolidation pressure p'_c/p'_{ini}, the NCL and the URL join at a point highlighted in Figure 3-6 as intercept. It is hypothesized that this intercept point is comparable to the normalized point given by p'_c/p'_{ini}, and given by the normalized coordinates $\left(V_{sc}/V_{s\,\mathrm{ini}}, p'_c/p'_{ini}\right)$. However, an offset between these two coordinates was measured because of the hold period at the end of each consolidation stage. In general, the abscissa of the intercept point of the two curves (i.e., NCL and URL) was between 1.5 and 1.6 in all the tests.

The coefficient β' is related to the steepness of the curves represented by Eq. (3-5) and characterizes the sensitivity of confining stresses with respect to changes in shear wave velocities. It is observed in Figure 3-6 that for overconsolidated states, a given change in V_s corresponds to a greater variation in p' than for normally consolidated states.

Therefore, the coefficient β' decreased from moving from overconsolidated to normally consolidated behavior.

From Figure 3-6, it may be argued that each unloading-reloading cycle experienced by the soil under consideration will require its own set of coefficients α' and β' to obtain changes in confining stresses as a function of seismic waves. Therefore, to approximate the stress history of the soil within a certain range of confining stresses, a large number of coefficients will be necessary. This approach, however, is not particularly descriptive as unloading and reloading cycles may occur at any point in the normally consolidated curve.

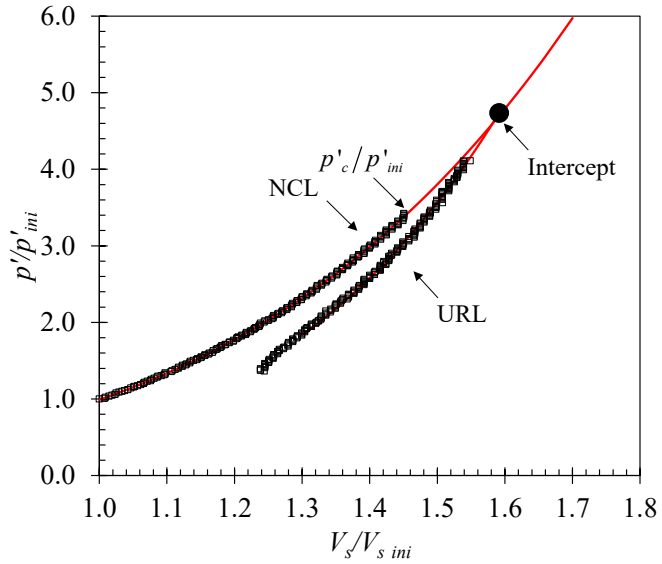

Figure 3-6 Normalized mean effective stress p' versus normalized shear wave velocity and V_s during loading and reloading stages for sample 1 U

From the previous reasoning about the relationships between p' and V_s. The following hypotheses were considered to establish a more general model that estimates stress state based on measured shear waves. First, a single curve can represent the relationship between p' and V_s for a normally consolidated soil. Second, any unloading reloading cycle can be characterized by a single slope analogous to β'. Finally, the effect of the void ratio on V_s is implicit in the relationships between V_s and p'. This study proposes to amend an hypoplasticity model to predict the full consolidation response encompassing the load-unload-reload consolidation path seismic waves measurement.

3.4 HYPOPLASTIC SCALAR MODEL FOR CONSOLIDATION

Constitutive models based on hypoplasticity are of the rate type. In these types of models, the strain rate is related to the stress rates through constitutive tensors of fourth and second order in the general three-dimensional case. The general non-linear soil behavior is captured by the stress dependence of the soil stiffness (Fellin 2002). Because of the rate nature of hypoplasticity, it is adequate to represent changes in p' with changes in V_s within a hypoplastic framework.

A hypoplastic scalar model for compression was introduced by Kadlíček et al. (2022). This model uses the compression law presented by Butterfield (1979), shown in Figure 3-7. It assumes that the normal consolidation line (NCL) is linear in the $\ln(1+e)$ - $\ln(p'/p'_r)$ space, where p'_r is a reference stress taken as 1 kPa. The position of the NCL is controlled by the parameters N , and λ^*. N represents the intercept of the NCL with the $\ln(1+e)$ axis (i.e., $\ln(1+e)$ at a p' equal to 1 kPa) and λ^* the slope of the NCL. Therefore, the normal consolidation line is given as

$$\ln(1+e) = N - \lambda^* \ln\left(\frac{p'}{p_r}\right) \tag{3-6}$$

The unloading line (URL) is characterized by the parameter κ^*, which is the slope at unloading from the normally consolidated state. Although the parameters N and λ^* are taken directly from the results of isotropic compression tests or oedometer tests, the parameter κ^* should be calibrated based on the results of these same tests, according to Mašín (2019). Figure 3-7 illustrates the parameters N , λ^* and κ^*.

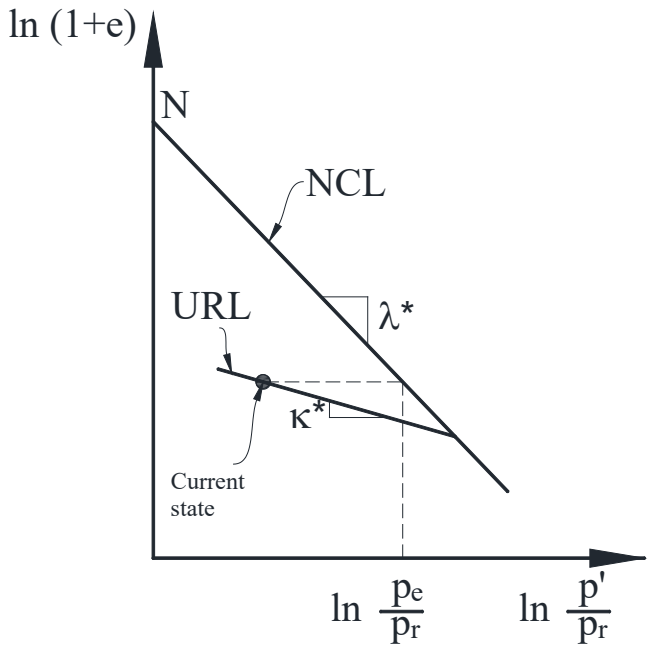

Figure 3-7 Graphical representation of the hypoplastic parameters N, λ^*, κ^*, and equivalent pressure p_e (Mašín 2019).

In Figure 3-7 p_e represents is an equivalent Hvorslev pressure; this is the pressure associated with the current void ratio at the NCL. For a soil state at the NCL, p' will be equal to p_e. The variable p_e is calculated for the current void ratio e as

$$p_e = \exp\left[\frac{N - \ln(1+e)}{\lambda^*}\right] \tag{3-7}$$

The change in effective stress associated with the change in volumetric strain can be expressed as

$$dp' = f_s\left(d\varepsilon_v + f_d Y\left|d\varepsilon_v\right|\right) \tag{3-8}$$

where $dp' =$ change in effective stress; $d\varepsilon_v =$ change in volumetric strain, it is defined as $d\varepsilon_v = de/1+e$; Y, f_s, and f_d are additional model variables. In oedometer tests, $d\varepsilon_v$ can be replaced by the normal strain, $d\varepsilon_n$, as the change in volumetric strain is equal to the change in normal strain. Also, the effective stress p' may be replaced by the effective vertical stress σ_v'. In this formulation, compressive stresses are taken as

negative; accordingly, during loading (i.e., compression) $d\varepsilon_v < 0$; during unloading $d\varepsilon_v > 0$. Stress states to the right of the NCL are not considered possible. The variable f_d is defined as

$$f_d = \left(-\frac{p'}{p_e} \right)^{\alpha_h} \tag{3-9}$$

where α_h is a factor that controls the stiffness non-linearity in the overconsolidated state. Finally, the variables Y and f_s are given as

$$Y = \frac{\lambda^* - \kappa^*}{\lambda^* + \kappa^*} \tag{3-10}$$

$$f_s = -p' \frac{\lambda^* + \kappa^*}{2\lambda^* \kappa^*} \tag{3-11}$$

To obtain the consolidation behavior of a soil with this approach, an incremental procedure is required in which a small change in $d\varepsilon_v$ is defined. The parameters N, λ^*, κ^*, and α_h are constants and given at the beginning of the computation. Based on the initial conditions (p'_o, e_o), p_e is determined from Eq. (3-7) from e_o. The variables f_d, Y, and f_s are calculated based on the current p'. The change in effective stress dp' is calculated from Eq (8). Finally, the values p' and e are updated as

$$p' = p'_{prev} + dp' \tag{3-12}$$

$$e = e_{prev} + de \tag{3-13}$$

where $de = d\varepsilon_v (1 + e_{prev})$. The incremental change in p_e is determined as a function of $d\varepsilon_v$ as

$$dp_e = -\frac{p_e}{\lambda *} d\varepsilon_v \tag{3-14}$$

A new $d\varepsilon_v$ value is imposed, and the values of p' and e are updated following the previous procedure.

Figure 3-8 presents the measured consolidation results for six of the samples in this study and the calculated using the hypoplastic scalar model by Mašín (2019). A constant value of 0.0005 was used for $d\varepsilon_v$ in the calculation. As observed in the figure, the measured and calculated results are in good agreement in all the cases. However, several remarks on the calculation process are applicable. First, the holding period at the end of each consolidation stage had a recognizable effect on the observed behavior, as seen in the variation of $\ln(1+e)$ for constant $\ln(p'/p_r)$. In some of the samples, this effect did not significantly influence the observed behavior, as shown in Figure 3-8 (a) and (b). In this case, the data shows that the soil remained close to the NCL line. Nevertheless, in the rest of the samples (Figure 3-8 (c), (d), (e), and (f)), there is a more prominent divergence for the NCL. It appears that this disparity was a function of the plasticity of each sample (i.e., it increased with sample plasticity).

Second, because the Mašín (2019) model does not consider the observed secondary compression during the hold period, in the calculation, the reloading portion of each curve was approximated based on the ordinate at the end of the hold period. Thus, in the calculation process, the confining pressures were estimated in the NCL until the value of $\ln(1+e)$ was similar to the measured value at the end of the hold period for the first loading stage, as seen in Figure 3-8 (a) and (b). A common characteristic observed in all the tests was the small values of λ^* and κ^*. A possible explanation for this fact was that during back-pressure saturation, an unregulated vacuum was actioned in the sample pressure tubing. This vacuum caused an involuntary compression of the samples. Table 3-3 presents the parameters estimated during consolidation for the test results shown in Figure 3-8.

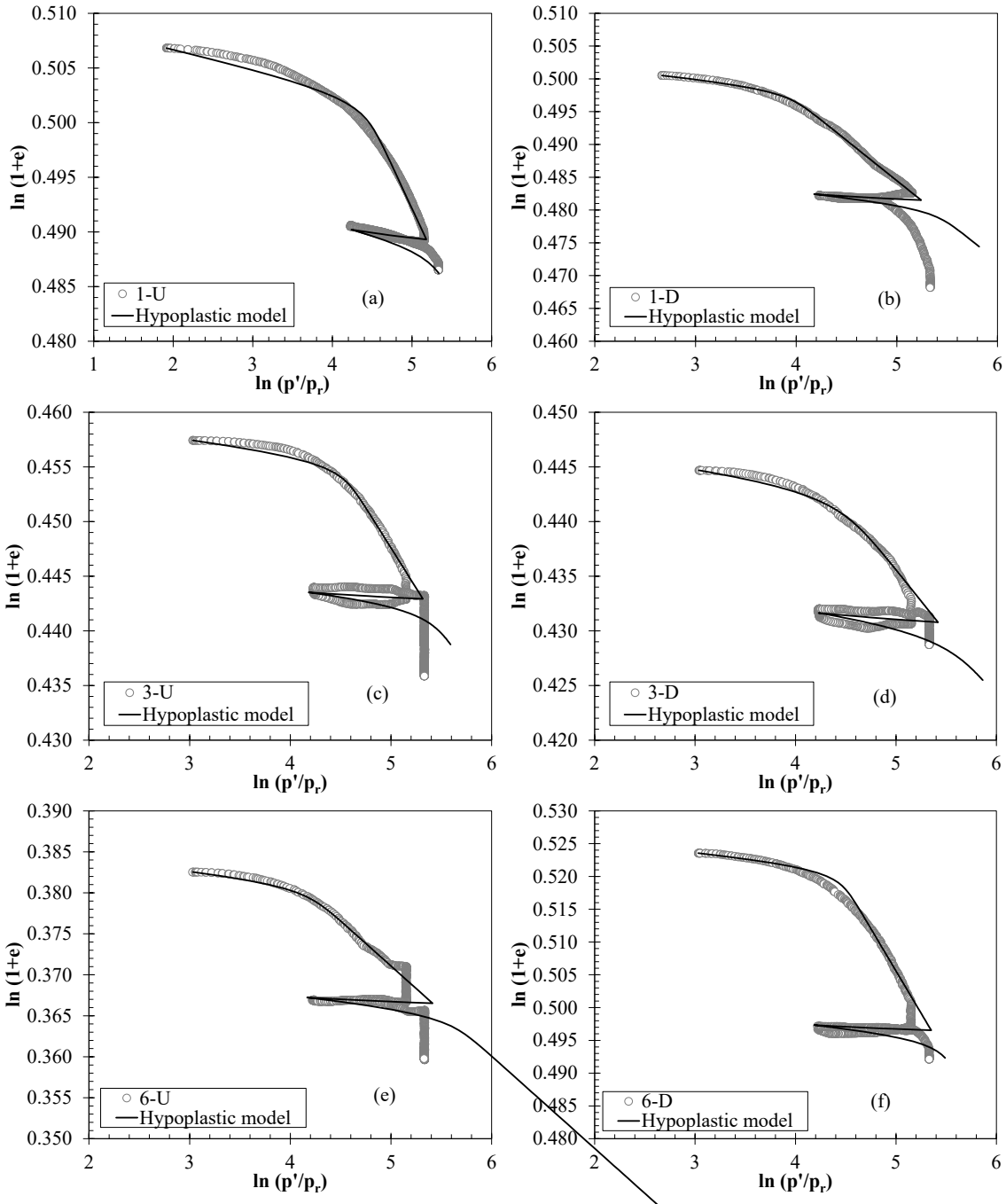

Figure 3-8 Consolidation results and hypoplastic model. Sample ID (a) 1-U;(b)1-D;(c)3-U;(d)3-D; (e)6-U; and (f) 6-D

Based on the results from this study, only one unloading-reloading cycle was predicted with the previous hypoplastic model (Mašín 2019). The adequacy of the previous approach to model several unloading-reloading cycles was determined based on the consolidation results presented by Zhao (2016). The measured response of three kaolinite

samples during consolidation is shown in Figure 3-9. The initial flat portion observed, for log-normalized pressures of around 2, in the consolidation curve was disregarded in the calculation. Notice that for these tests, the results are given based on the effective vertical stress σ_v' and not the mean confining stress p'. Regardless, the calculation process is the same as used in Figure 3-8.

In general, there is a good agreement between the measured and the calculated soil response. However, as seen in Figure 3-9, the third unloading cycle presents the greatest discrepancies for log-normalized pressures between 5 and 7. Therefore, it is presumed that an additional reloading cycle will make the computed response closer to the calculated, as observed in all the samples for the first and second unloading-reloading cycles (Figure 3-9). Figure 3-9 emphasizes that the stress history of the material can be conveniently described by a single parameter which in this case is κ^* in the logarithmic plane (Butterfield 1979).

Table 3-4 collects the parameters used for the calculation results shown in Figure 3-9.

Table 3-3 Parameters estimated from the test results of this study for samples shown in Figure 3-8

Sample ID	N	λ^*	κ^*	N_{V_s}	$\lambda^*_{V_s}$	$\kappa^*_{V_s}$
1-U	0.5706	0.0157	0.0008	-3.807	0.3060	0.15
1-D	0.5460	0.0123	0.0007	-3.779	0.3107	0.15
3-U	0.5211	0.0147	0.0005	-4.002	0.2412	0.035
3-D	0.4931	0.0115	0.0006	-3.271	0.3942	0.07
6-U	0.4261	0.011	0.0005	-3.433	0.3510	0.06
6-D	0.6346	0.0258	0.0006	-4.100	0.2203	0.06

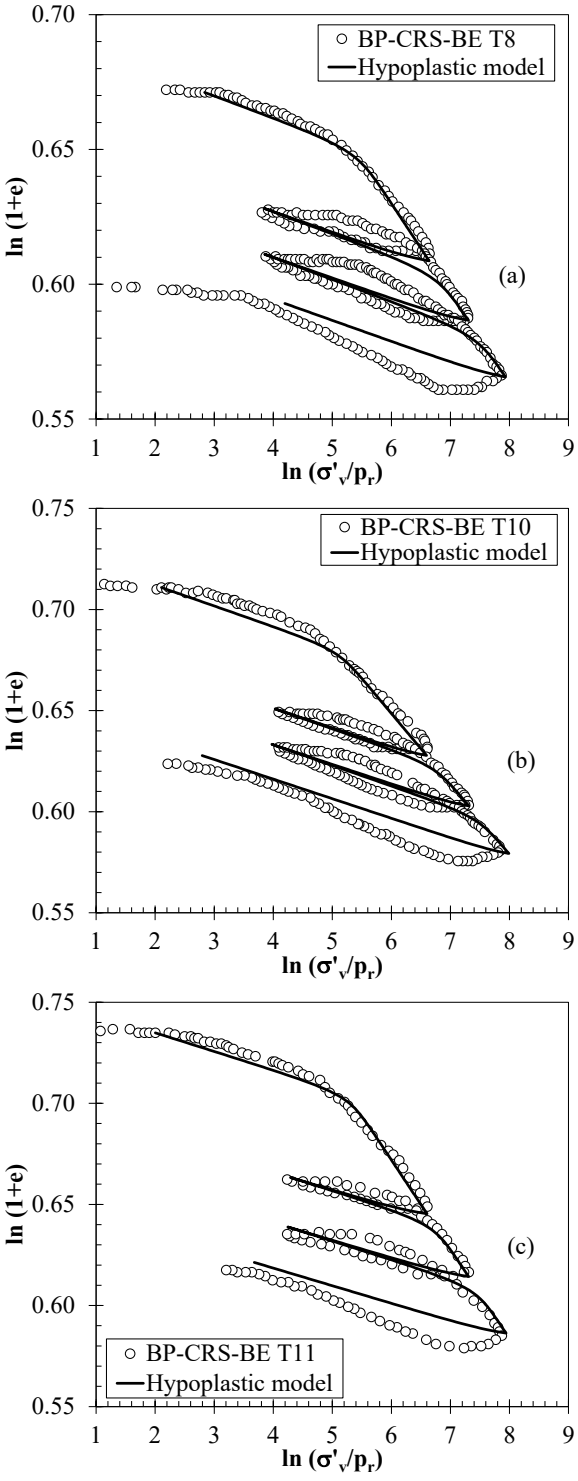

Figure 3-9 Kaolinite results from Zhao (2016). Sample (a) BP-CRS-BE T8; (b) BP-CRS-BE T10; and (c) BP-CRS-BE T11

Table 3-4 Parameters estimated from the Zhao (2016) test results

Sample	N	λ^*	κ^*
BP-CRS-BE T8	0.830	0.0333	0.0045
BP-CRS-BE T10	0.857	0.0348	0.0058
BP-CRS-BE T11	0.937	0.0441	0.0050
BP-CRS-BE T1	1.524	0.114	0.0032
BP-CRS-BE T2	1.601	0.121	0.0035

3.5 PROPOSED HYPOPLASTIC MODEL BASED ON V_s

Based on the observed results in Figure 3-8 , Figure 3-9 and the similarities between V_s and e variation shown in Figure 3-4, previously also reported by other authors (L'Heureux et al. 2013{Oh, 2017 #98; Elbeggo et al. 2019)}, it seemed suitable to apply a hypoplastic approach, to define the variation of p' or σ_v' with V_s.

Some modifications necessary to achieve this objective will be discussed along with the introduction of the proposed approach. Figure 3-10 presents the idealized variation of shear wave velocity and confining pressure. In this study, V_s is measured in units of m/s and p' in kPa. The ordinated are transformed from $\ln(1+e)$ (Figure 3-7) to $\ln(1/V_s)$. The slopes of the NCL and URL lines are given by the parameters λ^*_{Vs} and κ^*_{Vs}, respectively.

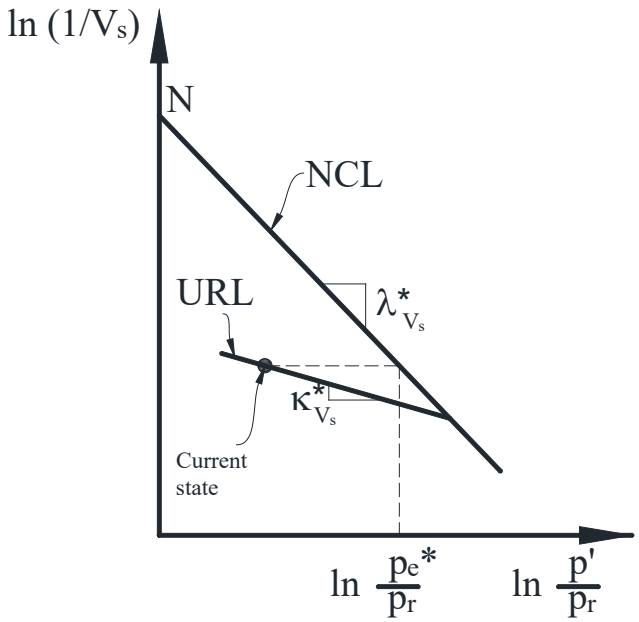

Figure 3-10 Proposed model parameters to relate shear wave velocity (Vs) and mean effective stress p'

The abscissa remains the same as the scalar model of Mašín (2019). Instead of using $d\varepsilon_v$ or $d\varepsilon_n$ in Eq. (3-8), a new dummy variable is defined as dV_s^*. Similar to the Mašín (2019) model, during loading (i.e., compression) $dV_s^* < 0$; during unloading $dV_s^* > 0$. The factor α_h from Eq. (3-9) is considered a constant and can be taken as 20. The equivalent pressure p_e for the initial state conditions is given by

$$p_e = \exp\left[\frac{N_{Vs} - \ln\left(1/V_s\right)}{\lambda^*_{Vs}}\right] \tag{3-15}$$

The incremental change in p_e is estimated as

$$dp_e = \frac{p_e \cdot dV_s}{\lambda^*_{Vs} \cdot V_s} \tag{3-16}$$

where $dV_s = -dV_s^* \cdot V_s$. Finally, dp' is given as

$$dp' = f_s\left(dV_s^* + f_d Y \left|dV_s^*\right|\right) \tag{3-17}$$

The values of Y, f_s, and f_d are computed as in Eq. (3-9), (3-10), and (3-11) but using the parameters λ^*_{Vs} and κ^*_{Vs}. Figure 3-11 presents a flowchart of the proposed approach to estimate the variation of p' based on measured values of V_s.

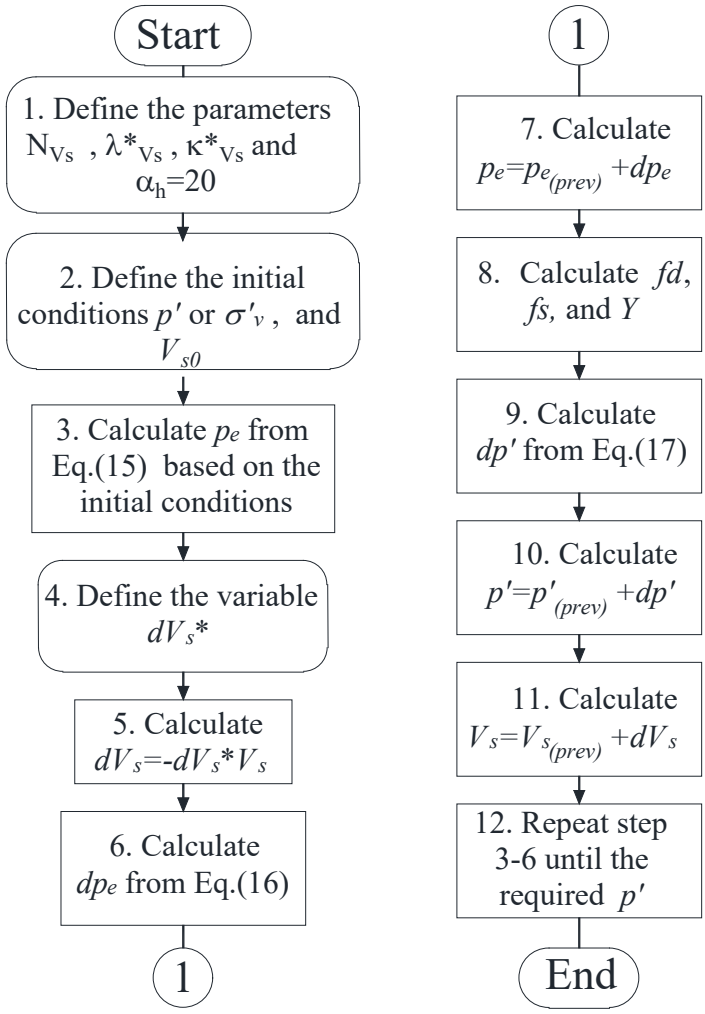

Figure 3-11 Flowchart of the proposed approach to estimate consolidation processes, based shear wave velocities V_s.

In the proposed methodology, monotonic loading during consolidation, as proposed by Muttashar et al. (2019), is captured by defining the parameters N_{Vs} and λ^*_{Vs}. Furthermore, the stress history of the material is captured by defining the parameter κ^*_{Vs} in conjunction with the previous parameters.

Figure 3-12 presents the measured and calculated results using the proposed approach in this study for the samples shown in Figure 3-8. From the measured data in each sample, the effect of the hold period at the end of each consolidation step is also observed in the variation of V_s. During this period, the travel path of the shear waves is reduced because of the decrease in void ratio; thus, V_s increased. Unlike the consolidation

results in terms of $\ln(1+e)$, where the initial conditions for the calculation were those directly measured at the beginning of consolidation, in the $\ln(1/V_s)$ plane, the initial conditions for most of the samples were at a confining pressure of about 50 kPa, as seen in Figure 3-12 (c) until (f). It appears that for the samples in this study, this pressure is an adequate lowest threshold for the initial conditions when using the proposed approach. However, a definitive statement in this regard will require more investigation.

As observed in Figure 3-12, the proposed approach gives reasonable results compared to the measured data. The greatest discrepancies are observed in samples on which the hold period had an observable effect on V_s , as in Figure 3-12 (e). In the NCL line, the calculated results are in very good agreement with the measured. On the other hand, in the URL line, the calculated results are like an average value of the measured. The gradual change in the curvature of the consolidation curve seen in Figure 3-8 is not observed in the $\ln(1/V_s)$ - $\ln(p'/p_r)$ for pressures close to the NCL in the reloading path as in Figure 3-12. By setting α_h to 20, the unloading-reloading portion of the calculated results appears to be a straight line.

In all the calculations, a value of $|dV_s^*|$ equal to 0.0009 was used. As previously reported, confining pressures were calculated in the NCL line until the value of $\ln(1/V_s)$ was comparable to the measured value at the end of the hold period. This adjustment in the calculation approach is not required for consolidation results that do not include periods of constant load. The parameters used in the calculations are presented in Table 3-3.

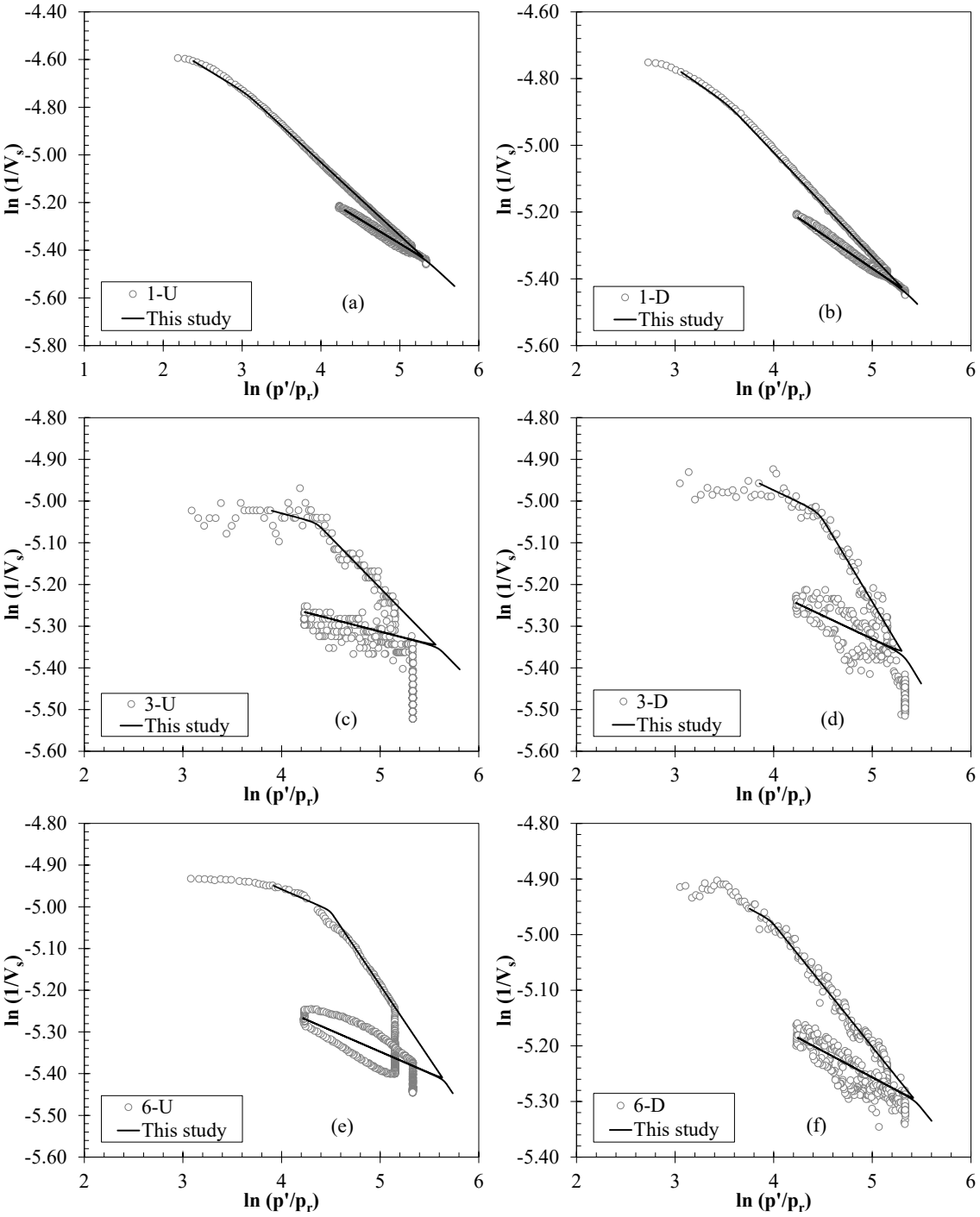

Figure 3-12 Comparison of results. Sample ID (a) 1-U;(b)1-D;(c)3-U;(d)3-D; (e)6-U; and (f) 6-D

3.6 VALIDATION OF THE PROPOSED APPROACH

The proposed approach was validated based on test results in the literature where shear wave velocities were measured during consolidation. Each of these collected results was obtained under a different test setup to the one used in this study. Regardless of the test configurations, a close agreement was obtained between the reported and the calculated results. Only the results in terms of shear wave velocities and confining pressures are shown in this section. The calculated consolidation results in terms of void ratio and confining pressure are shown in the supplemental data.

3.7 VS MEASURED DURING CONSTANT-RATE-OF-STRAIN CONSOLIDATION

Zhao (2016) conducted consolidation tests on Kaolinite and Illite soil samples. These samples were tested on a back-pressure saturated, constant-rate-of-strain consolidation device. Shear wave velocities were measured with bender elements attached to the consolidation device. The direction of the shear waves was horizontal, and their polarization was vertical.

Figure 3-13 shows the measured V_s corresponding to the test results from Figure 3-9. The measured data was discretized based on the unloading-reloading cycles during consolidation. In most of the loading cycles, a clear interpretation of the parameter λ^*_{Vs} that defines normally consolidated loading (NCL) was obtained. However, a deviation of the inferred trend defined by λ^*_{Vs} was noticed in the first cycle of the BP-CRS-BE T8 test (Figure 3-13 (a)). The other tests seemed to line up closely along the NCL line.

The initial conditions for the calculation were selected based on a confining pressure of 50 kPa, as the pair of σ'_v-V_s values closest to this threshold. The reported data agrees with the proposed approach in all three tests in the first and second unloading paths. Nevertheless, apparent discrepancies are observed in the third unloading path, except for the initial unloading values of $\ln(1/V_s)$ in the BP-CRS-BE T10 test (Figure 3-13 (b)). This observation may suggest that the presented approach is limited to confining pressures less than 2980 kPa approximately. Regardless of this consideration, further research is required to fully establish the applicable range of pressures of the presented methodology. Nevertheless, in all the cases, the best agreement was obtained for the second loading cycle.

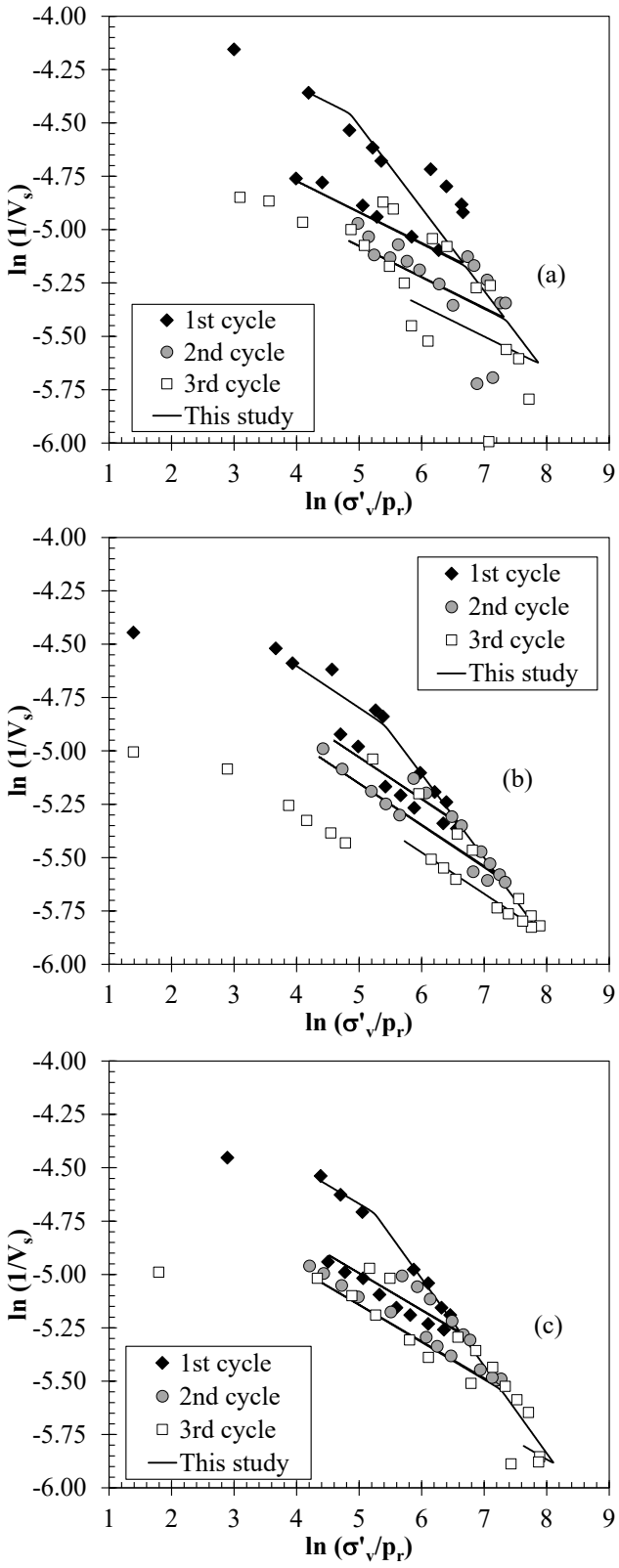

Figure 3-13 Measured and calculated response of Kaolinite test results. Sample (a) BP-CRS-BE T8; (b) BP-CRS-BE T10; and (c) BP-CRS-BE T11

Reported results on Illite samples are presented in Figure 3-14. Only two loading cycles were imposed on these samples. In both Illite tests, the predicted variation of the shear wave velocity with confining stress was in good agreement with the reported. The characteristic loop in V_s during unloading-reloading observed in the samples tested in this study (Figure 3-12) is clearly shown in Figure 3-14 (a). In general, V_s measurements during normally consolidated loading are well represented by the parameters λ^*_{Vs} and N_{Vs}. Although, some measured values in the second reloading cycle of sample BP-CRS-BE T2 (Figure 3-14 (b)) are slightly off the NCL line. In both tests, loading under overconsolidated conditions is adequately described with the parameter κ^*_{Vs}. The initial condition for the calculation was selected based on the closest conditions above a confining pressure of 50 kPa (i.e., $\ln \sigma'_v / p_r = 3.9$).

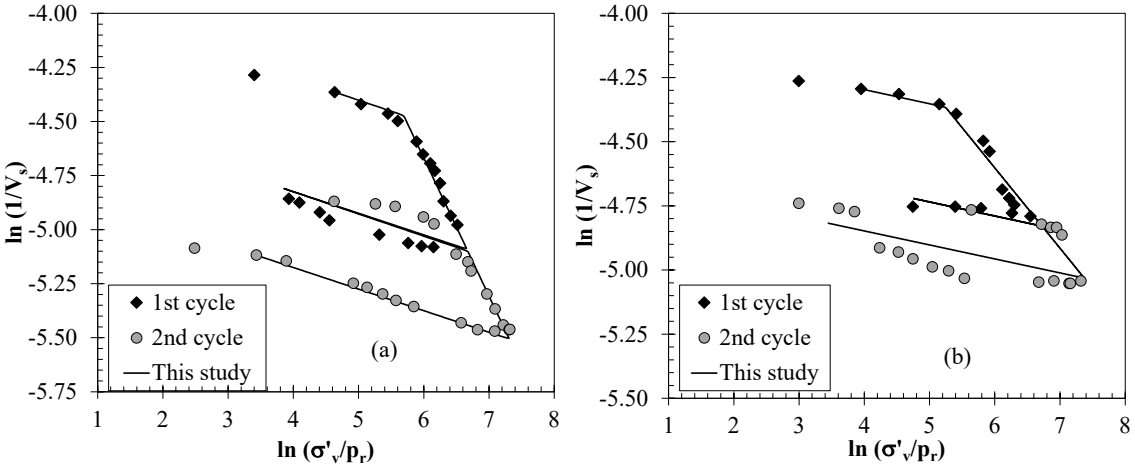

Figure 3-14 Comparison of Illite test results. Sample (a) BP-CRS-BE T1; (b) BP-CRS-BE T2

Table 3-5 lists the parameters estimated and used for the approach calculation presented in Figure 3-13 and Figure 3-14. As shown in

Table 3-5, the three estimated parameters are similar for the kaolinite samples. On the other hand, in the Illite samples, a difference was in the parameters N_{V_s} and $\lambda^*_{V_s}$. Given that both samples adjust to the presented formulation, with only two samples tested, it is challenging to ascertain which set of parameters is more representative of Illite behavior.

Table 3-5 Parameters estimated from the Zhao (2016) test results for the proposed methodology

Sample	N_{V_s}	$\lambda^*_{V_s}$	$\kappa^*_{V_s}$
BP-CRS-BE T8	-2.585	0.386	0.090
BP-CRS-BE T10	-2.774	0.389	0.130
BP-CRS-BE T11	-2.580	0.407	0.110
BP-CRS-BE T1	-0.843	0.638	0.055
BP-CRS-BE T2	-2.725	0.313	0.030

3.8 VS MEASURED DURING OEDOMETER TESTING AND PIEZOELECTRIC RING-ACTUATOR (P-RAT)

Elbeggo et al. (2019) reported a set of test results. These tests were conducted on soft soil by using an oedometer apparatus. Shear wave velocities were determined by using the piezoelectric ring-actuator technique (P-RAT). Figure 3-15 presents the set of consolidation test results on Abitibi clay in which only monotonic loading was imposed on the samples. In all the cases, the NCL line was clearly identified (i.e., N_{Vs} and λ^*_{Vs}) from the measured data. Ideally, the parameter κ^*_{Vs} is estimated from an unloading-reloading cycle. Nonetheless, in these tests, κ^*_{Vs} was estimated based on the initial loading points of the consolidation curve. The close agreement between the measured data and the estimated shown in Figure 3-15 highlights the fact that the presented approach not only estimates stress history (i.e., overconsolidated loading) but can also be used to predict monotonic loading.

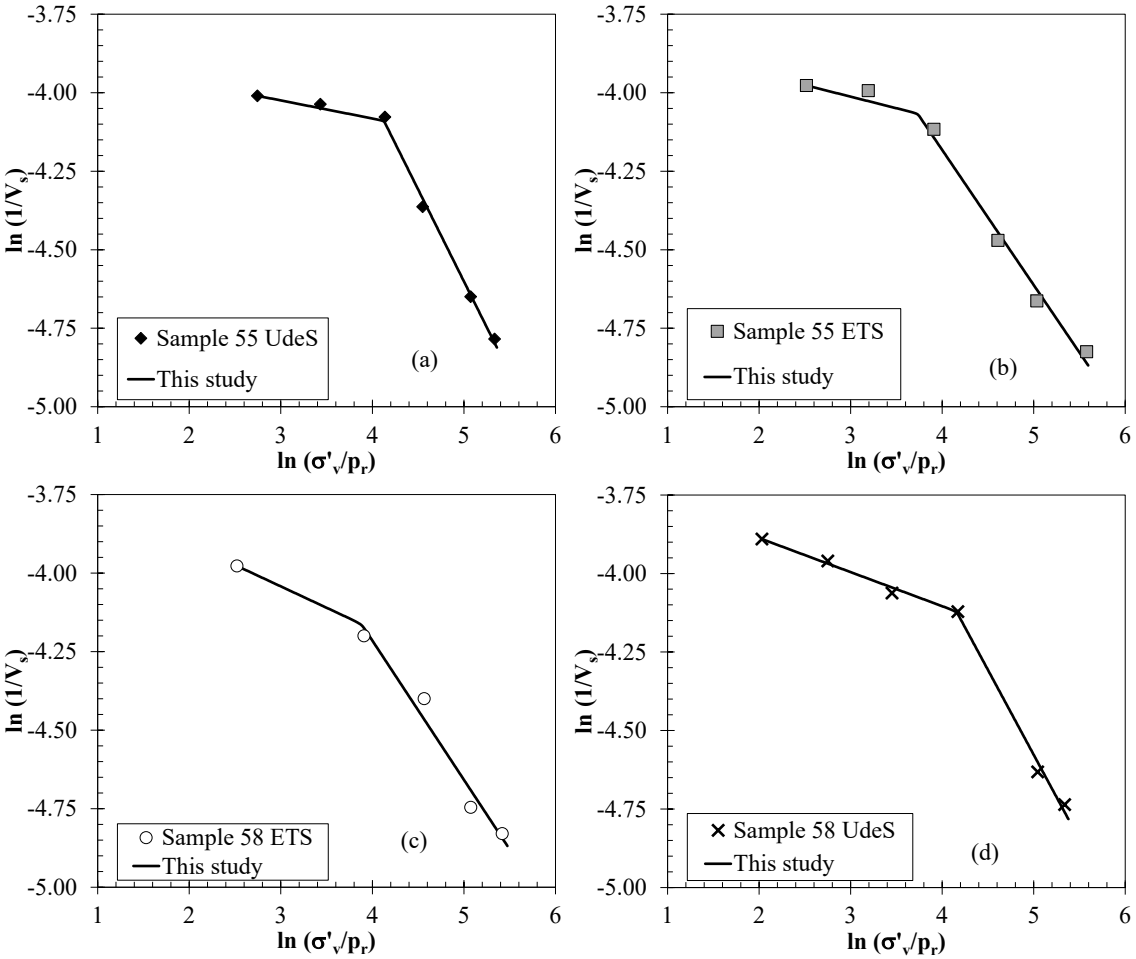

Figure 3-15 Comparison of test results on Abitibi clay. Sample: (a)55 UdeS;(b) 55 ETS; (c) 58 ETS; and (d) 58 UdeS

Elbeggo et al. (2019) also reported consolidation test results on St-Hilaire clay, as shown in Figure 3-16. For these samples, an unloading cycle was applied during consolidation. It is clear from the measured data in both samples in Figure 3-16 that the parameter κ^*_{Vs} estimated in the unloading portion of the results does not represent the observed tendency in the first three data points. This remark supports the assumption that the presented approach is mostly suitable for confining pressures of at least 50 kPa. The initial conditions for the calculation were taken at the third data point, which corresponds to the beginning of normally consolidated loading. Despite the initial differences in the observed behavior, the presented approach correctly predicted the variation of $\ln(1/V_s)$ and $\ln(\sigma'_v/p_r)$ in the NCL and URL lines.

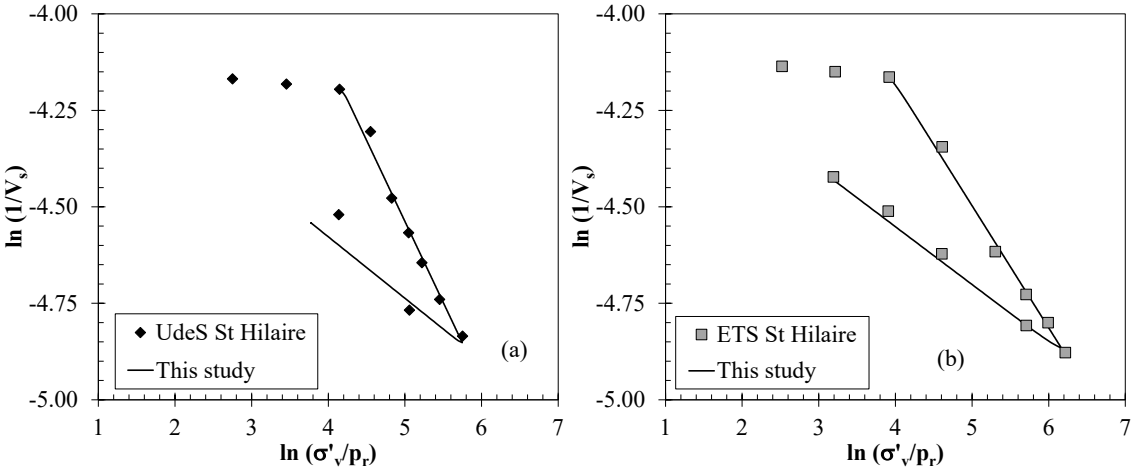

Figure 3-16 Comparison of test results on St-Hilaire clay. Sample: (a) UdeS St Hilaire; and (b) ETS St Hilaire.

The parameters used in the calculations shown in Figure 3-16 and Figure 3-17 are listed in Table 3-6. The estimated parameters are generally consistent with the test location ETS or UdeS. For the Abitibi clay, the average values of the parameters N_{V_s}, $\lambda^*_{V_s}$, and $\kappa^*_{V_s}$ at the ETS location were -2.45, 0.44, and 0.06, respectively. The corresponding values at the UdeS location were -1.78,0.56, and 0.05. For the St-Hilaire clay, the average values of the parameters N_{V_s}, $\lambda^*_{V_s}$, and $\kappa^*_{V_s}$ were -2.68, 037, and 0.10, respectively. Additional tests conducted by these authors are also shown in the supplemental data.

Table 3-6 Parameters estimated from the Elbeggo et al. (2019) test results

Sample	N_{V_s}	$\lambda^*_{V_s}$	$\kappa^*_{V_s}$
Sample 55 UdeS	-1.676	0.585	0.03
Sample 55 ETS	-2.462	0.430	0.04
Sample 58 ETS	-2.443	0.443	0.08
Sample 58 UdeS	-1.875	0.540	0.06
UdeS St Hilaire	-2.4396	0.4196	0.10
ETS St Hilaire	-2.9157	0.3162	0.10

3.9 VS MEASURED IN A FLOATING WALL CONSOLIDOMETER

Kang et al. (2014) presented consolidation results on Kaolinite samples using a floating wall consolidometer with bender elements attached in the vertical and horizontal directions. The results of a Kaolinite sample mixed with a NaCl solution with a concentration of 0.005mol/l are shown Figure 3-17. At each consolidation step, three shear

wave velocity measurements were taken. One V_s was obtained with the vertical bender elements (i.e., "vh"), and the other two were obtained with the horizontal bender elements (i.e., "hv" and "hh").

The initial V_s values for the calculation were selected at a confining pressure of 48 kPa. A satisfactory agreement is observed in Figure 3-17 between the reported results and the calculated. For loading along the NCL, the measurement aligned to the line defined by the parameters N_{V_s} and $\lambda^*_{V_s}$ except for the V_s at a confining pressure of 416 kPa. During unloading from the NCL, the initial two measurements were underestimated with the proposed approach. However, the rest of the V_s values are well represented by the parameter $\kappa^*_{V_s}$. Even though the direction and polarization of the shear waves velocities presented in Figure 3-17 was different, the proposed approach captures the behavior regardless of the source of V_s. Table 3-7 lists the parameters used in the calculations shown in Figure 3-17.

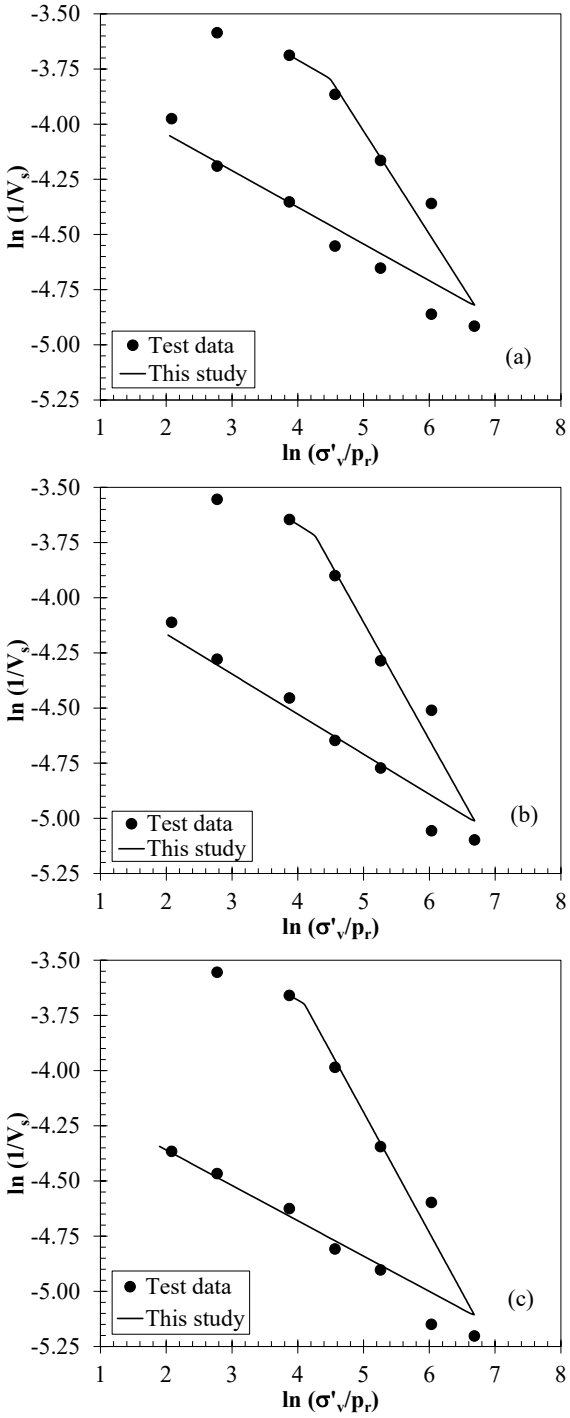

Figure 3-17 Consolidation test results by Kang et al. (2014) for different wave propagation directions (a) vh; (b) hv; and (c) hh.

Table 3-7 Parameters estimated from the Kang et al. (2014) test results

Wave direction	N_{V_s}	$\lambda^*_{V_s}$	$\kappa^*_{V_s}$
vh	-1.7017	0.4657	0.10275
hv	-1.4516	0.5318	0.11095
hh	-1.4664	0.5442	0.09535

3.10 VOLUMETRIC STRAIN AS A FUNCTION OF VS

The presented approach can be used to estimate volumetric strains from an initial condition based on normally consolidated loading or unloading. Figure 3-18 (a) is the same previous Figure 3-17 (a); it was repeated to illustrate the proposed procedure to estimate volumetric strain (ε_v) based on measured shear wave velocities. Figure 3-18 (b) shows the consolidation results in terms of void ratio for the results shown.

For normally consolidated loading from point A to B in Figure 3-18, the volumetric strain is calculated as follows. At point A the quantities e_0, σ'_{v0} and V_{s0} are known. These quantities are linked as shown in Figure 3-18 with the solid arrows and correspond to number 1 in the vertical axes. An additional point 2 in the axis $\ln(1/V_s)$ is selected (Figure 3-18 (a)), and the corresponding void ratio is shown by the dashed arrows (Figure 3-18 (b)). Considering the initial conditions at A, the volumetric strain from 1 to 2 is given as $\varepsilon_v = (\Delta e / 1 + e_0)$. Additional points are selected in both curves, and the variation of ε_v with V_s can be approximated. The previous procedure was applied for unloading from point B until point C. In this case, the initial conditions were defined based on B.

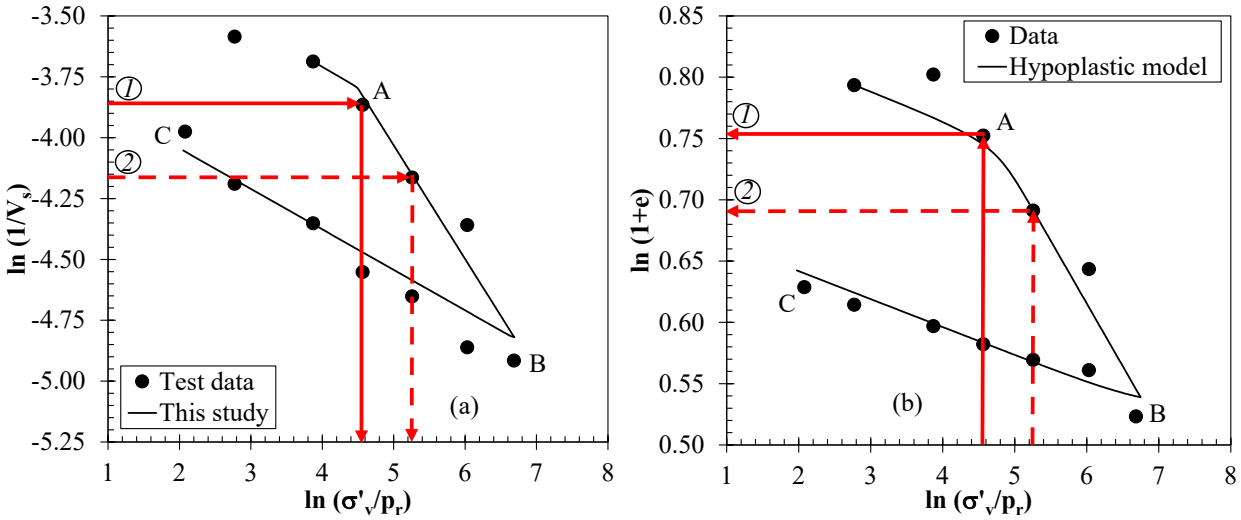

Figure 3-18 Consolidation test results from Kang et al. (2014) in terms of (a) Shear wave velocity ("vh"); (b) void ratio.

Figure 3-19 shows the variation of volumetric strain during loading along the NCL and unloading from the NCL. For loading, the calculated volumetric strain is very much like the measured for all four points along the normal consolidation line, as seen in Figure 3-19(a). For unloading, the calculated results show the same trend observed in the measured data, representing an average strain variation. While initial values of volumetric strain were underpredicted, the final two volumetric strain measurements were underpredicted. Notice that in Figure 3-19, compressive strains were considered positive.

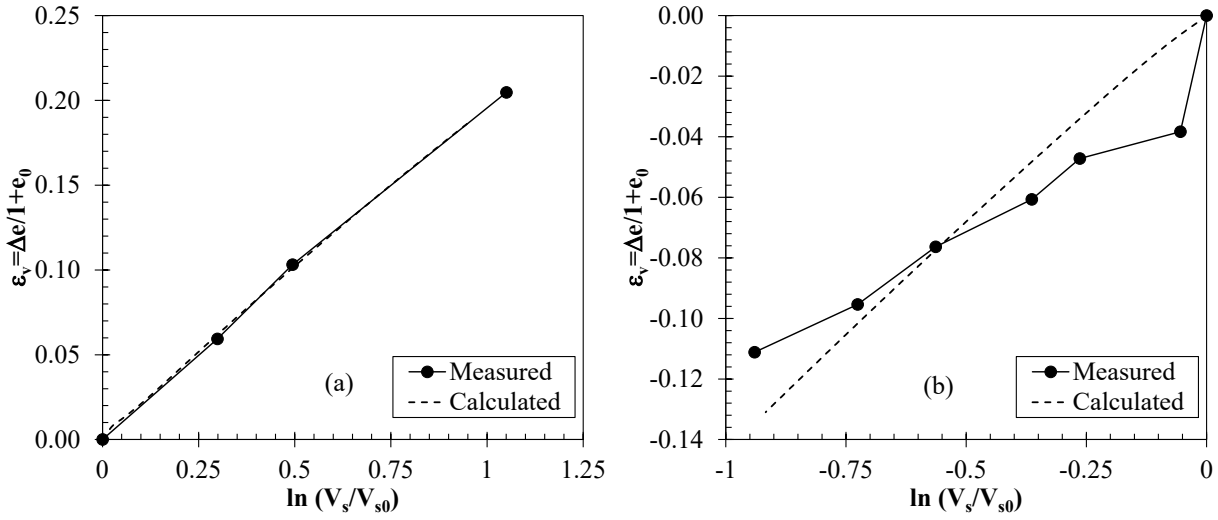

Figure 3-19 Volumetric strain as a function of shear wave velocity for (a) normally consolidated loading; (b) unloading

3.11 PARAMETER'S VARIATION

Figure 3-20 shows the variation of the parameter N, λ^* and κ^*, which can be estimated from routinely soil tests as oedometer test, with those defined in terms of shear wave velocities (N_{Vs} , λ^*_{Vs} and κ^*_{Vs}). The data points correspond to the figures presented in this paper and the supplemental data. Generally, a wider variation is observed for the parameters defining the behavior V_s. As these parameters (N_{Vs} , λ^*_{Vs} and κ^*_{Vs}) implicitly assume the influence of void ratio on shear wave velocities, they may be susceptible to slight changes in the initial conditions during testing.

In Figure 3-20, the results appear to be clustered based on the type of consolidation conditions (i.e., isotropic consolidation, constant-rate-of-strain consolidation). From Figure 3-20 (a) and Figure 3-20 (b), it is observed, in general, a direct proportionally between the shear wave velocity parameters N_{Vs} λ^*_{Vs} and the consolidation parameters N, λ^*. However, the other two parameters κ^*_{Vs} and κ^* do not show a distinctive pattern. As previously stated, the estimated parameters N, λ^* and κ^* from this study were small in comparison with those from other studies as they align to the left of the horizontal axis. However, the parameters N_{Vs} , λ^*_{Vs} and κ^*_{Vs} are in much agreement with the other studies, as seen in the ordinates of Figure 3-20. Fitting curves were not adjusted through the data due to the limited number of data points.

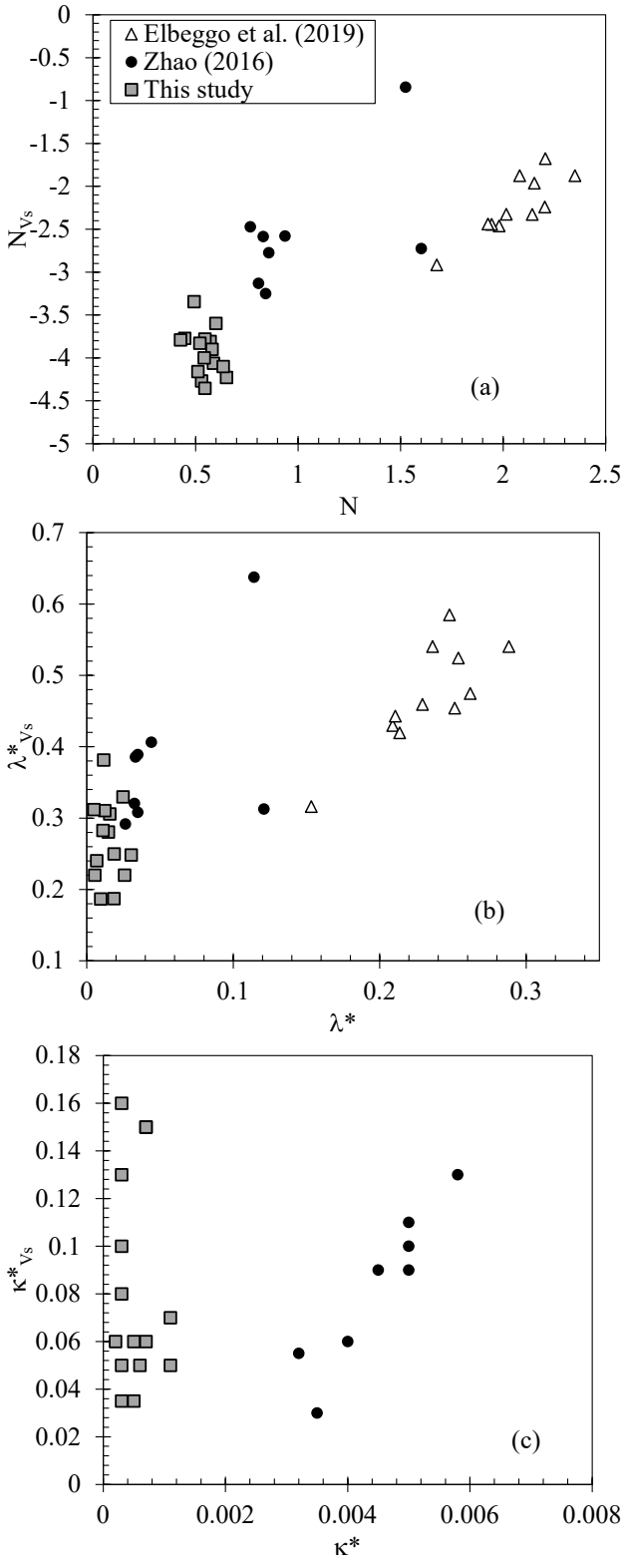

Figure 3-20 Consolidation parameters versus the proposed geophysical parameters: (a) N versus N_{Vs} (b) λ^* versus λ^*_{Vs} ; and (c) κ^* versus κ^*_{Vs}.

3.12 SUPPLEMENTAL DATA

This section contains the supplemental data for this chapter.

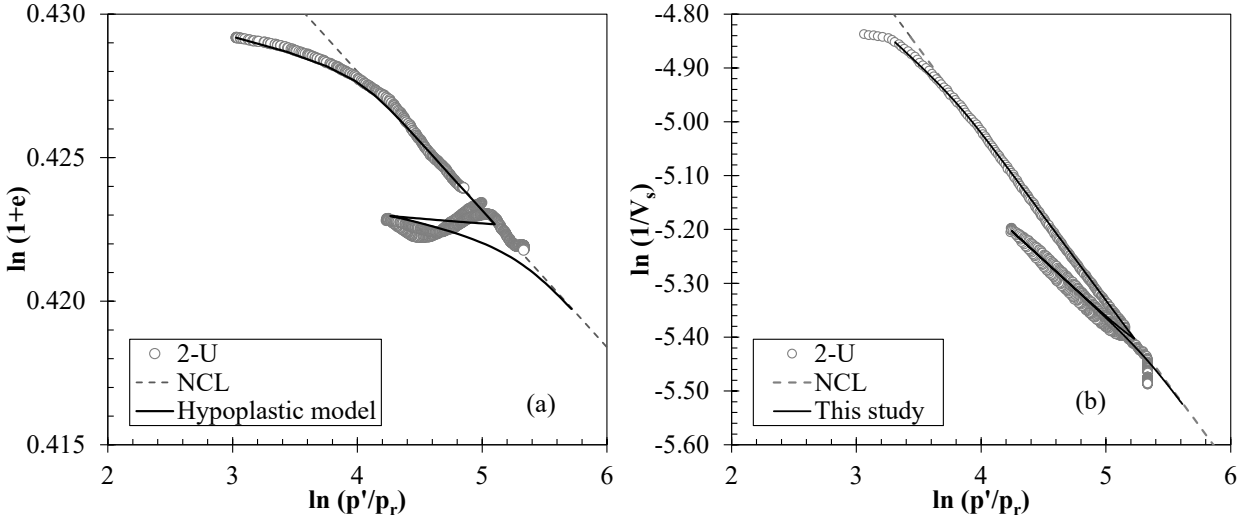

Figure 3-21 Comparison of results. Sample 2-U (a) Consolidation; (b) Shear-wave velocity

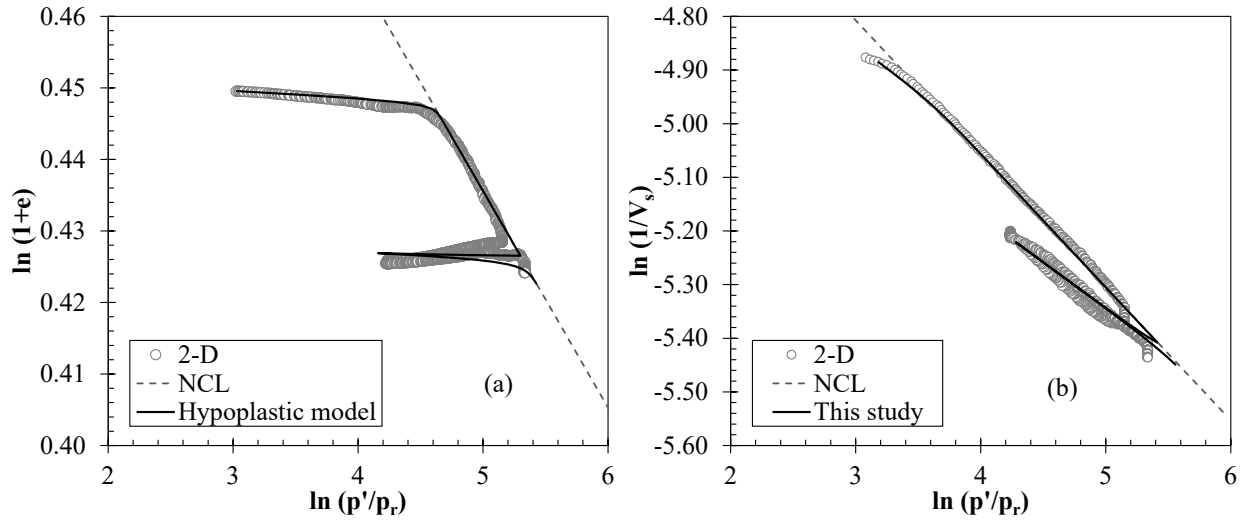

Figure 3-22 Comparison of results. Sample 2-D (a) Consolidation; (b) Shear-wave velocity

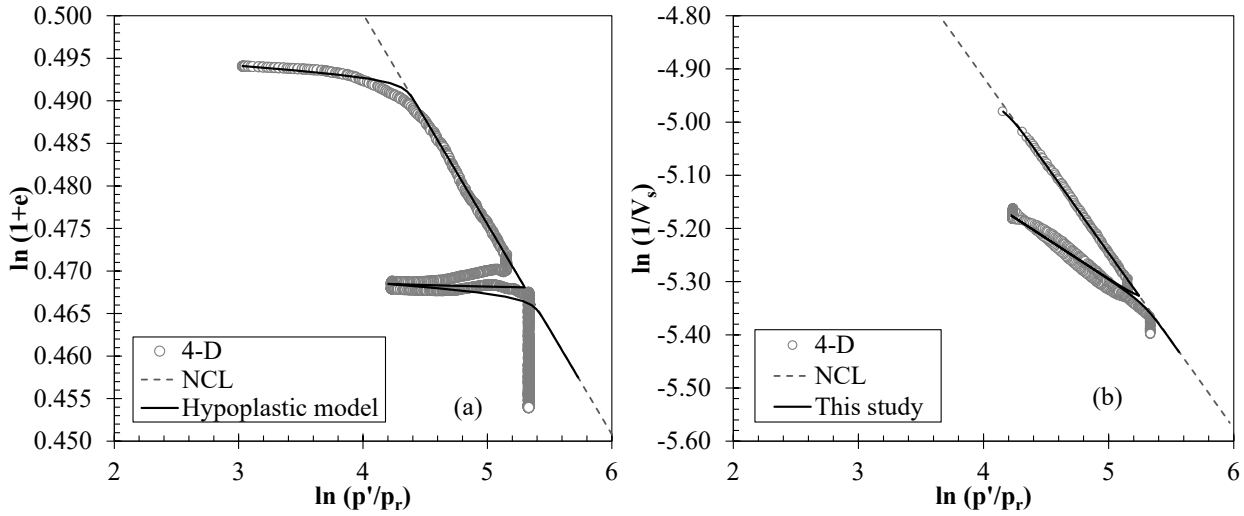

Figure 3-23 Comparison of results. Sample 4-D (a) Consolidation; (b) Shear-wave velocity

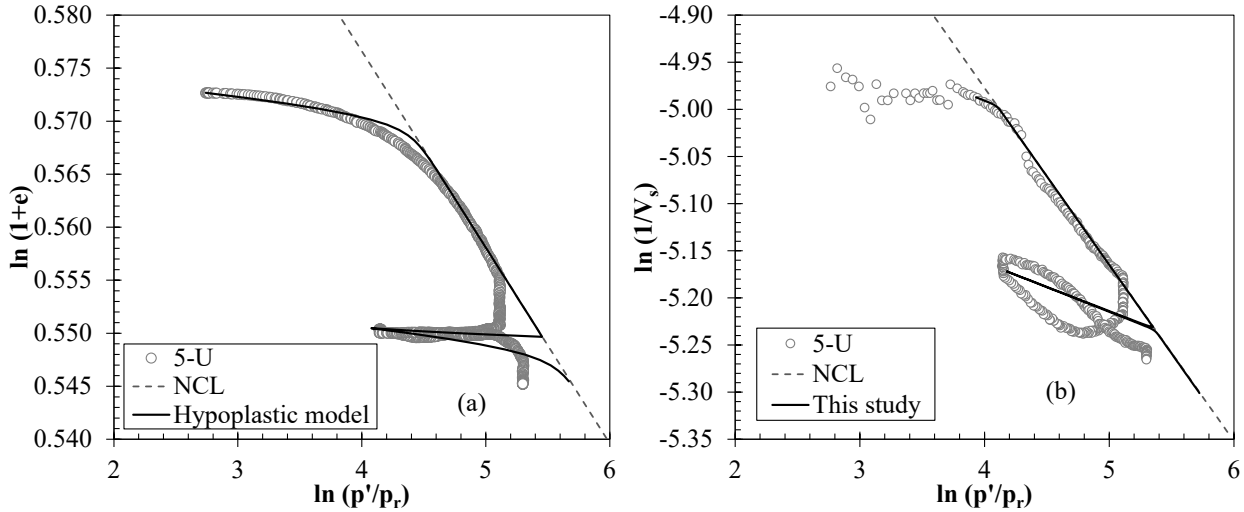

Figure 3-24 Comparison of results. Sample 5-U (a) Consolidation; (b) Shear-wave velocity

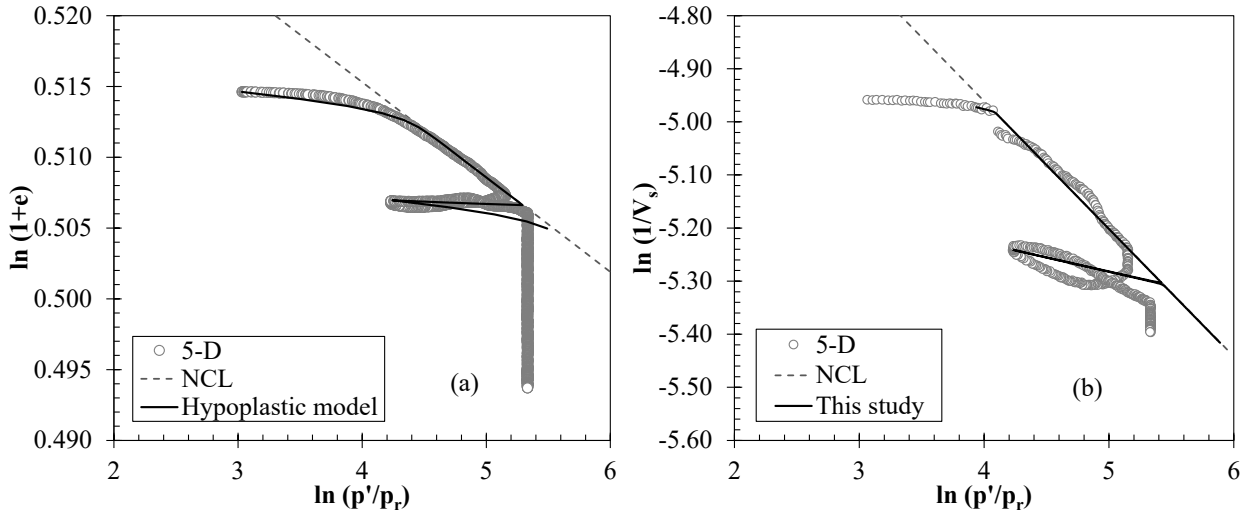

Figure 3-25 Comparison of results. Sample 5-D (a) Consolidation; (b) Shear-wave velocity

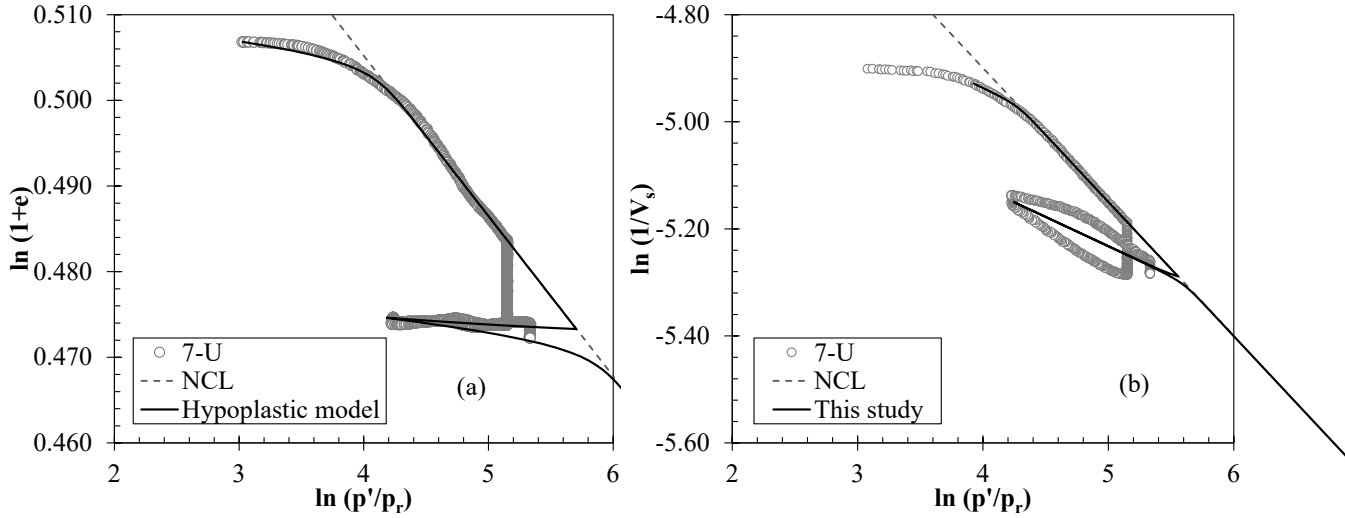

Figure 3-26 Comparison of results. Sample 7-U (a) Consolidation; (b) Shear-wave velocity

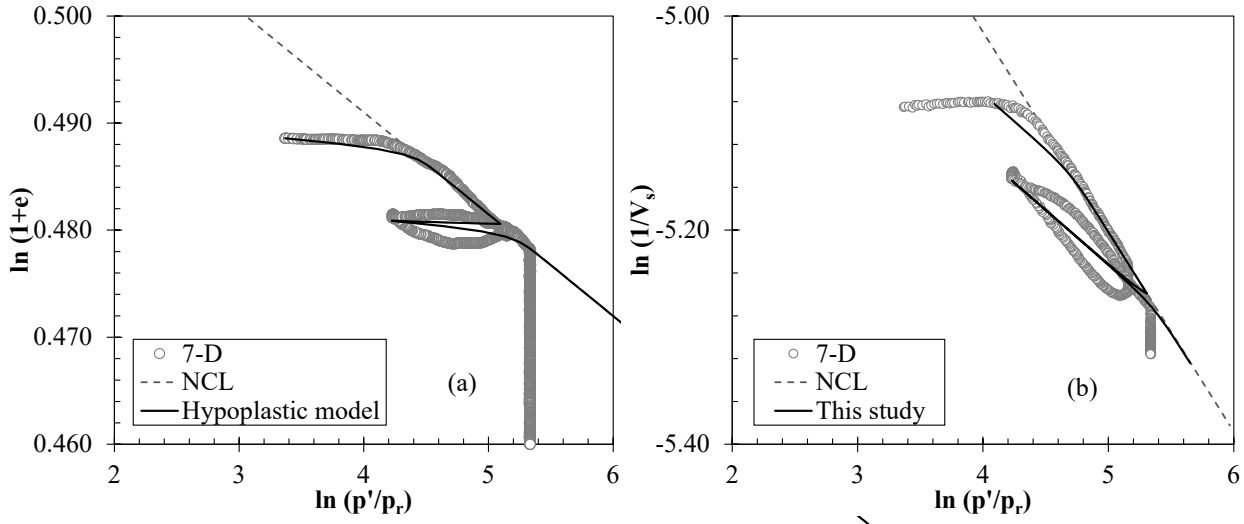

Figure 3-27Comparison of results. Sample 7-D (a) Consolidation; (b) Shear-wave velocity

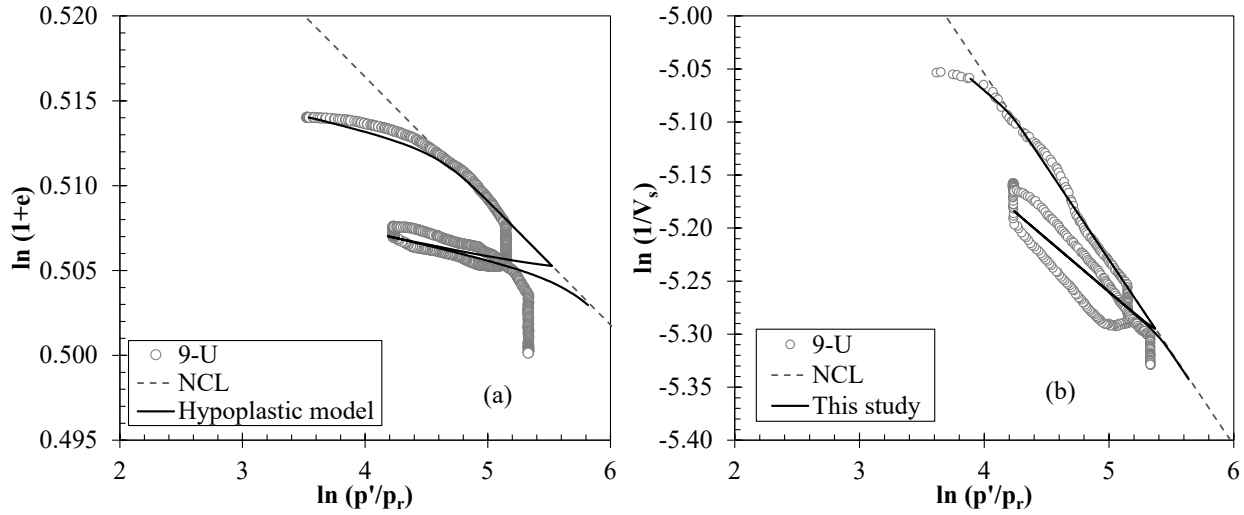

Figure 3-28 Comparison of results. Sample 9-U (a) Consolidation; (b) Shear-wave velocity

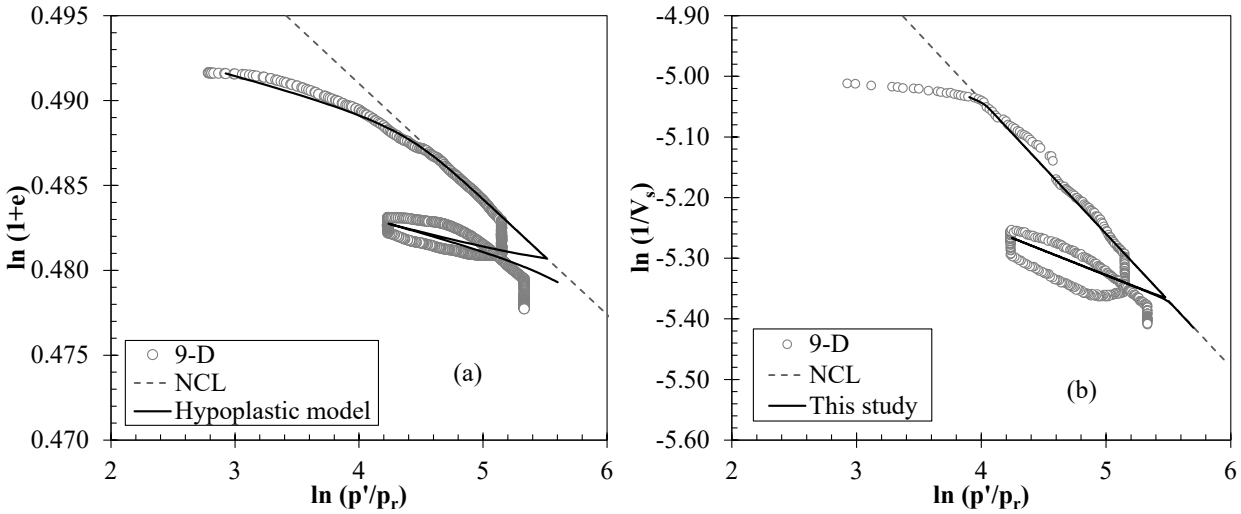

Figure 3-29 Comparison of results. Sample 9-D (a) Consolidation; (b) Shear-wave velocity

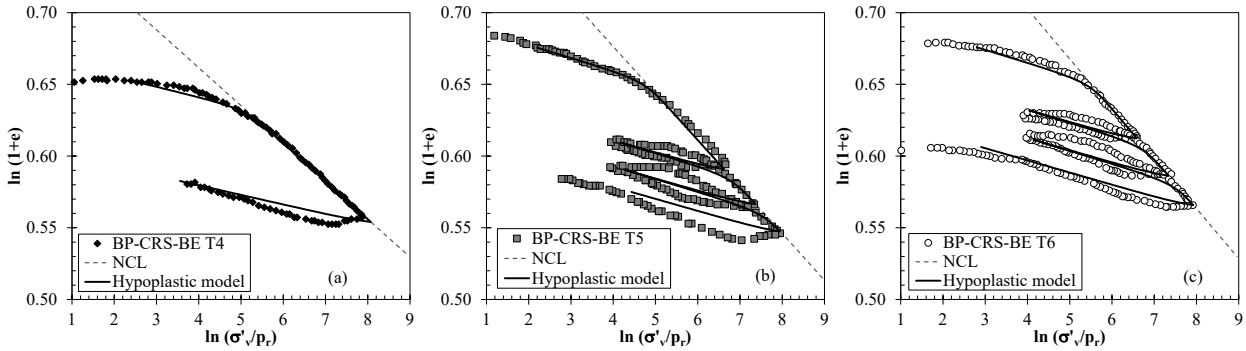

Figure 3-30 Kaolinite results from Zhao (2016). Sample (a) BP-CRS-BE T4; (b) BP-CRS-BE T5; and (c) BP-CRS-BE T6

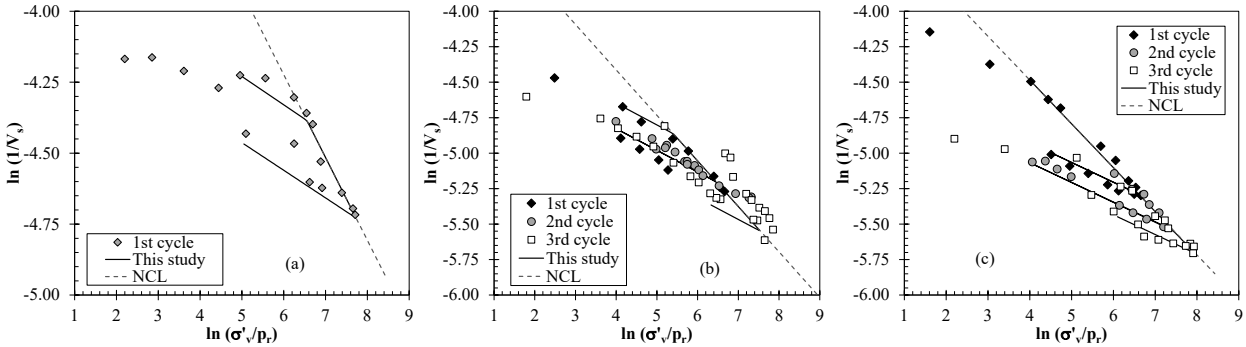

Figure 3-31 Comparison of Kaolinite test results. Sample (a) BP-CRS-BE T4; (b) BP-CRS-BE T5; and (c) BP-CRS-BE T6

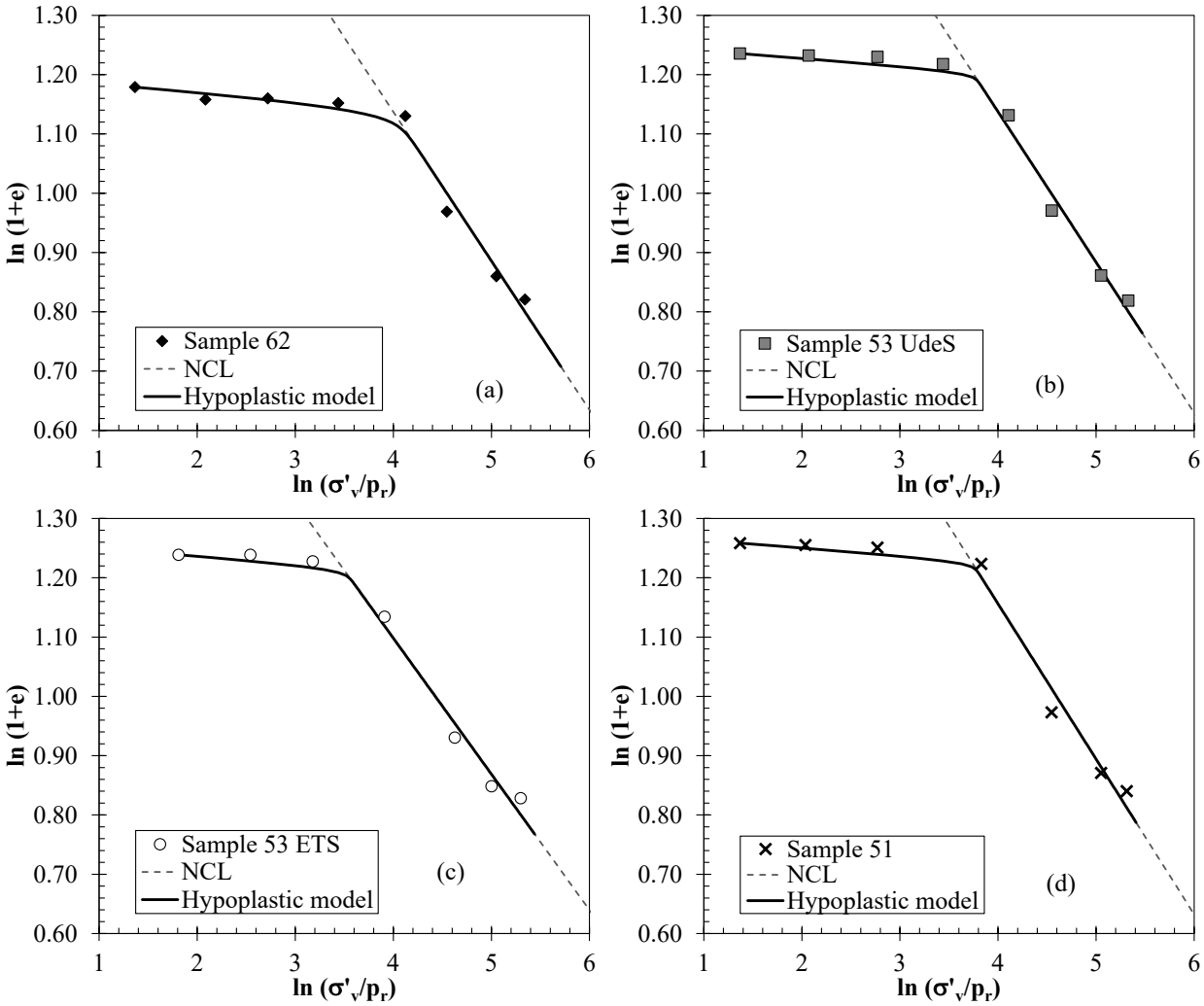

Figure 3-32 Consolidation results from Elbeggo et al. (2019). Sample :(a)62 ;(b) 53 UdeS; (c) 53 ETS; (d) 51

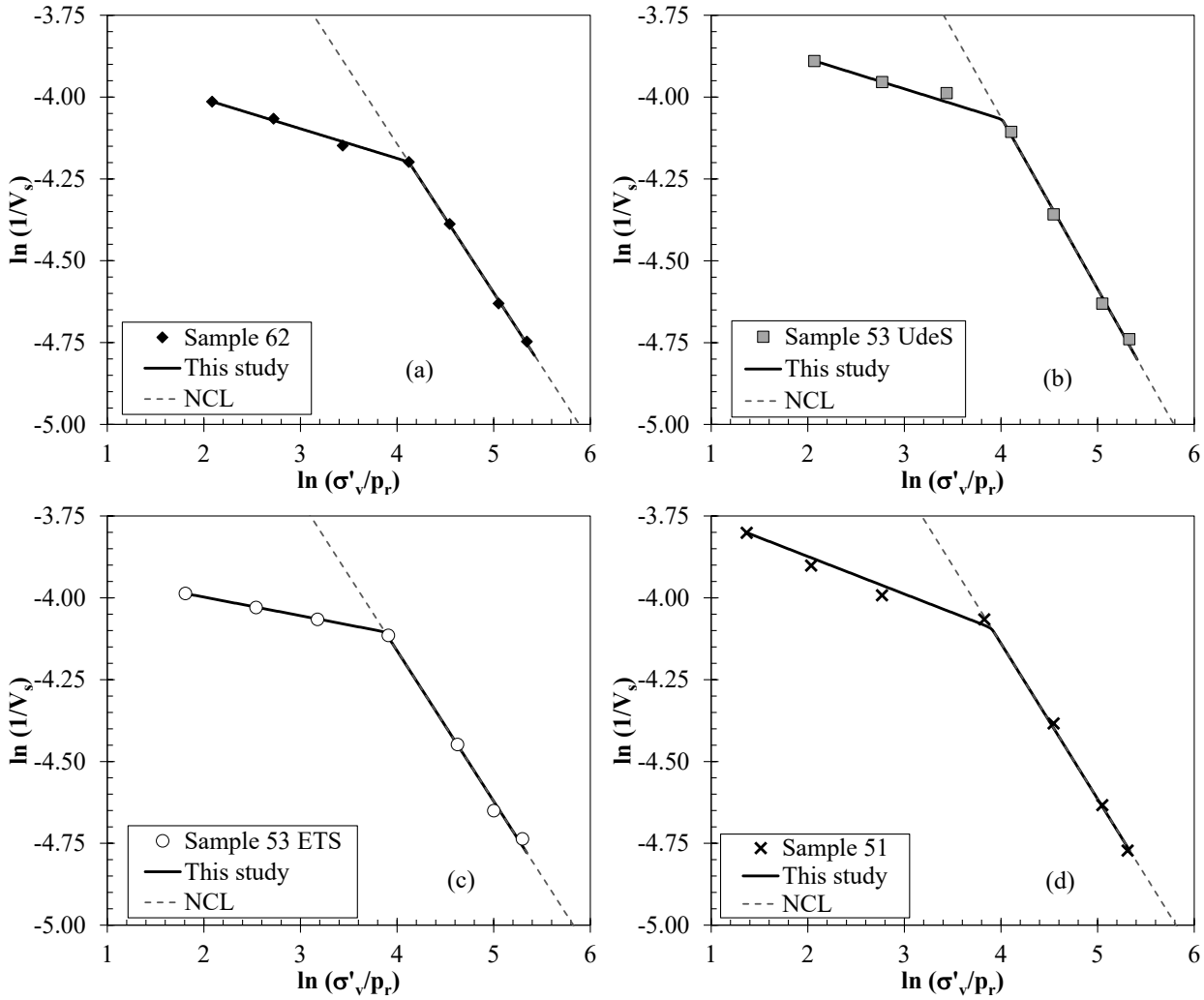

Figure 3-33 Comparison of test results. c Sample :(a)62 ;(b) 53 UdeS; (c) 53 ETS; (d) 51

Table 3-8 Parameters estimated from the Zhao (2016) test results used in Figure 3-34 and Figure 3-35

Sample ID	N	λ^*	κ^*	N_{V_s}	$\lambda^*_{V_s}$	$\kappa^*_{V_s}$
BP-CRS-BE_T4	0.7672	0.0264	0.0040	-2.4717	0.2919	0.0600
BP-CRS-BE_T5	0.8068	0.0326	0.0050	-3.1307	0.3206	0.1000
BP-CRS-BE_T6	0.8417	0.0348	0.0050	-3.2512	0.3083	0.0900

Table 3-9 Parameters estimated from the Zhao (2016) test results used in Figure 3-36 and Figure 3-37

Sample ID	N	λ^*	κ^*	N_{V_s}	$\lambda^*_{V_s}$	$\kappa^*_{V_s}$
Sample62	2.1424	0.2513	0.006	-2.327	0.4541	0.05
Sample53_UdeS	2.1527	0.2538	0.0055	-1.964	0.5244	0.05
Sample53_ETS	2.0154	0.2293	0.006	-2.325	0.4592	0.03
Sample51	2.2038	0.2619	0.0055	-2.240	0.4747	0.07

CHAPTER 4

GEOPHYSICS BASED APPROACH TO PREDICT TRIAXIAL UNDRAINED AND DRAINED COMPRESSIVE BEHAVIOR IN COHESIVE SOILS

4.1 INTRODUCTION

Geophysical measurements, such as seismic wave velocities (e.g., shear wave and compression wave velocities) and electrical conductivity (EC), are routinely used to perform geotechnical and hydrologic site characterization. These measurements allow the determination of subsurface characteristics such as material types and thicknesses, groundwater regime, bedrock depth, and geologic contacts. In addition, geophysical methods have also been applied to estimate engineering properties and soil parameters, usually through empirical correlations. Soil conditions in terms of compaction (Besson et al. 2013; Ni et al. 2018; Hua et al. 2020; Romero-Ruiz et al. 2022), unit weight, effective stresses (Ghorbani et al. 2012; Duan et al. 2019; Owusu-Nimo and Boadu 2020), strength and stiffness (Donohue et al. 2011; Tong et al. 2018; Díaz-Curiel et al. 2020; Cheshomi and Khalili 2021), slope stability (Crawford et al. 2019; Hojat et al. 2019), are some of the practical applications of geophysical measurements. In addition, these techniques are readily adapted to remote sensing platforms. Thus, allowing for the possibility to remotely sense the subsurface conditions and mechanical behavior (Whitlow et al. 2019; Gaber et al. 2020).

Shear wave velocity, V_s, is a geophysical measurement that can be used effectively for in-situ soil characterization and prediction of deformation and shear behavior for soils. Several techniques, invasive and non-invasive, are currently available to determine this property. In situ methods such as the cross-hole method (ASTM 2014), downhole method (ASTM 2019), uphole method (Bang and Kim 2007), seismic dilatometer test (SDMT) (Marchetti et al. 2008), seismic cone penetration test (Stolte and Cox 2020), spectral analysis of surface waves (SASW) (Wang et al. 2020), multi-channel analysis of surface wave (MASW) (Ni et al. 2018) are commonly used. On the other hand, shear wave velocities are determined in the laboratory with methods such as bender elements (BE), torsional shear, resonant column, piezoelectric ring-actuator technique (P-RAT) (Lee and

Santamarina 2005; Elbeggo et al. 2019; Khosravi et al. 2020). However, the BEs method is the most common for V_s determination in lab testing.

Shear wave velocity is affected by parameters as pore structure (grain size distribution and grain shape), degree of saturation, stress state, and state history (Hardin and Black 1968; Santamarina et al. 2001; Vardanega and Bolton 2013). As these parameters also affect the strength and deformation behavior of soil (Robertson et al. 1995; Cho et al. 2006), the shear wave velocity of soil can be considered as a proxy of mechanical behavior. Due to its rapid determination over large subsurface areas, a shear wave velocity is a valuable tool in geotechnical engineering practice. In several studies, in-situ measurements of V_s have been used as an input variable to evaluate various geotechnical quantities of interest. V_s has been used to evaluate soil sample disturbance (Landon et al. 2007; Donohue and Long 2010), index properties (L'Heureux and Long 2017), compression and stiffness properties (L'Heureux and Long 2017), strength measurements (L'Heureux and Long 2017; Oh et al. 2017; Trafford and Long 2020), triaxial results (Black et al. 2009; Muttashar and Bryson 2020), bearing capacity (Tezcan et al. 2006; Ghavami et al. 2019), preconsolidation pressure (Duan et al. 2019).

This study presents an approach to estimating triaxial soil behavior based on shear wave velocity measurements. Based on triaxial drained and undrained test results with bender elements, normalized relationships between shear wave velocity V_s and mean effective stress, p', are defined. A hypoplastic constitutive model (Mašín 2005) in terms of stress invariants is presented, and guidance on using this model for stress-controlled testing is given. By using the normalized relationships as input for the constitutive model under a stress-controlled setting, triaxial variables such as deviatoric strain and stress, volumetric strain, and excess porewater pressure can be determined as a function of shear wave velocities. It is expected that geotechnical operations may benefit from the methodology presented herein. The significance of this aspect is that the full range of mechanical behavior for soil may be potentially predicted at any point in a three-dimensional soil mass using geophysical techniques that are readily adapted to remote sensing platforms. The proposed methodology is specific to soils ranging from silts to lean clays.

4.2 TEST PROCEDURE AND MATERIALS

Triaxial testing was conducted in six resedimented samples prepared from three different materials to develop a geophysical-based model to predict compression behavior in undrained and drained conditions. Table 4-1 presents the index properties of these tested materials from the state of Kentucky. Figure 4-1 shows the grain size distribution of the tested materials, which according to the properties in Table 4-1, are predominantly silt. The traditional resedimentation technique applies static weights to the slurry to consolidate the sample (Germaine and Germaine 2009). Although this approach produces a uniform sample, the density of the sample is not controlled. For this study, the sample density was controlled by compressing the slurry to a targeted height at a very low displacement rate. Displacement rates ranged between 0.025 and 0.019 mm/min, depending on samples being predominantly silt or predominantly clay, respectively. These rates were slow enough to allow excess porewater pressures to dissipate during the preparation process. Also, the vertical load corresponding to the displacement was recorded during this process. Low vertical load corresponded to low displacement rate and vice versa. The maximum vertical loads exerted on the samples during the precompression process ranged between 50 and 70 kPa.

During triaxial testing, bender element (BE) measurements were taken to determine shear wave velocities. Bender elements are piezoelectric devices that allow seismic wave velocity estimations based on input signals propagated through the tested sample. For this study, input signals were propagated in a vertical direction, in which one Bender Element was attached to the lower platen of the triaxial cell, and the other was embedded on the top surface of the sample. Based on both input, and output signals from the BE, the travel time of the seismic wave was determined. Finally, the shear wave velocity was determined as the ratio between the sample's vertical length and the signal's travel time at the time of the BE test.

Table 4-1 Index properties of tested materials

Sample Material	Fines (%)	Clay (%)	Silt (%)	CF/SF	LL (%)	PI (%)
S1	75.5	9.3	66.2	0.140	30.0	20.5
S2	60	11.5	48.5	0.237	31.0	22.0
S3	51	7.2	43.8	0.164	31.5	20.8

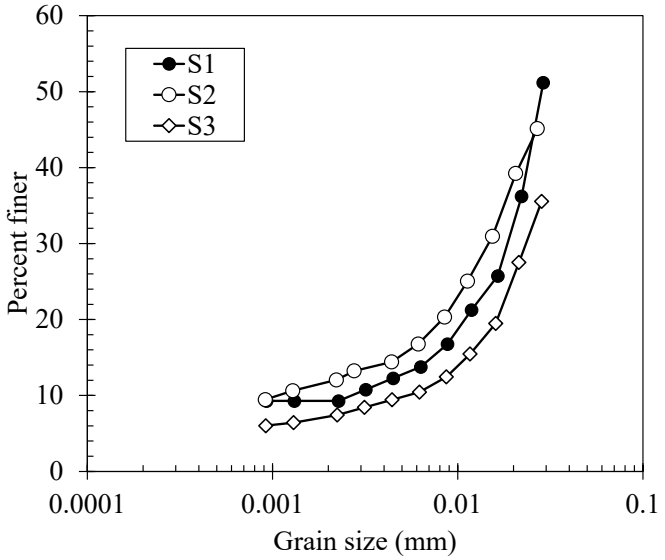

Figure 4-1 Grain size distribution of the tested materials

4.3 TRIAXIAL COMPRESSION TESTING RESULTS

Figure 4-2 presents the triaxial test results for the tested samples. Undrained strength was lower than drained strength in the three materials. In addition, there is a considerable difference in the axial strain at the maximum deviatoric stress, q, between drained and undrained tests. For undrained testing, the peak stress was reached at strain values of less than 2%. While for drained testing, this stress was reached at strain values of around 16%. Friction angles, V_s, used in the calculation presented later in this study were determined based on the results shown in Figure 4-2.

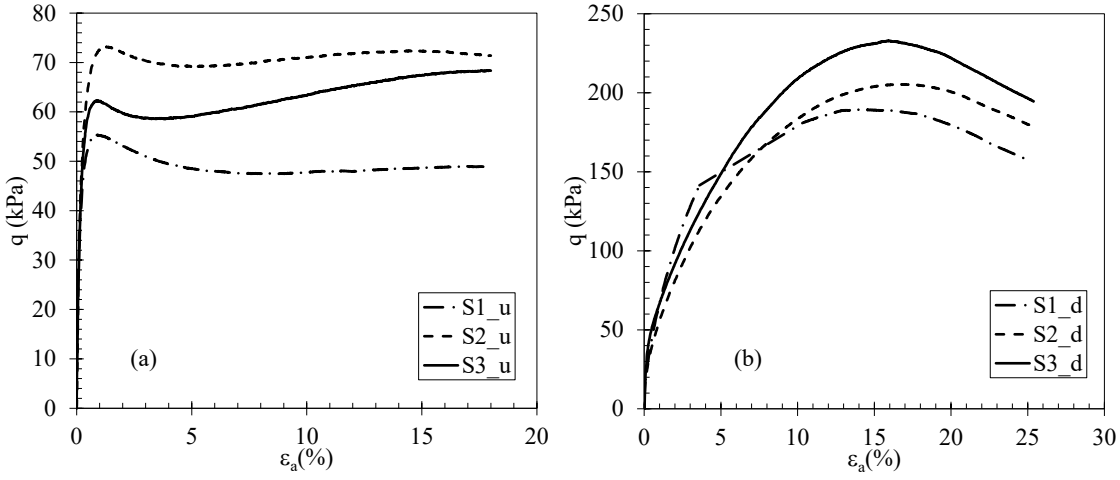

Figure 4-2 Stress strain response of the tested samples: (a) Undrained tests and (b) Drained tests

4.4 SHEAR WAVE MEASUREMENTS DURING TRIAXIAL COMPRESSION

Previous research by Muttashar and Bryson (2020) showed that triaxial behavior under undrained conditions could be predicted based on measurements of shear wave velocities V_s. For samples of normally consolidated soils, Figure 4-3 shows the typical variation of mean effective stress, p' and V_s during shearing starting at point A. As observed from the figure, both quantities decrease during the tests with increasing strain and the development of excess pore water pressure. In this figure, p'_0 and V_{s0} are the mean effective stress and shear wave velocity at the beginning of shearing.

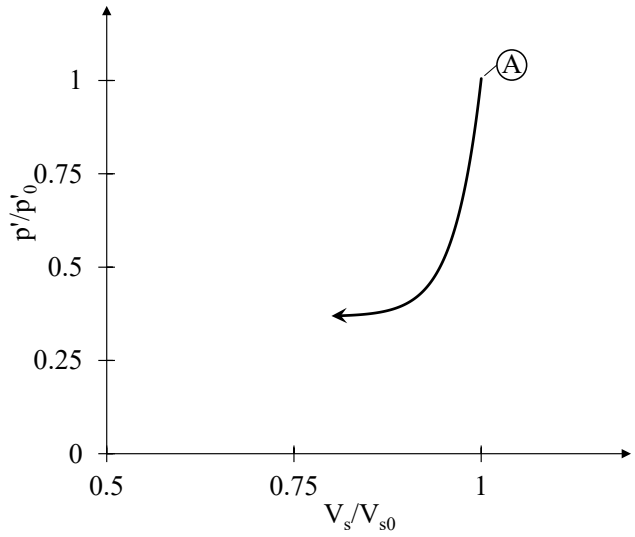

Figure 4-3 Normalized relationship between mean effective stress p' and shear wave velocity Vs

The observed behavior was described by a two-term power function of the form

$$\frac{p'}{p'_0} = C_1 + C_2\left(\frac{V_s}{V_{s0}}\right)^{C_3} \tag{4-1}$$

$C_1, C_2,$ and C_3 are fitting coefficients related to the initial state conditions. Therefore, these coefficients were taken as functions of the initial void ratio, e_0, of the samples. Using Eq (1), Cam clay models were adapted to predict stress-strain behavior within a critical state framework. Given the current variety of methods to measure shear wave velocities in the field, this approach is attractive for estimating construction performance, in terms of strain and deviatoric stresses, based on continuous monitoring V_s

. To improve the prediction capabilities of the previous approach, it is required to also observe the variation of the p' and V_s during drained testing. In this way, both limiting conditions of soil behavior, undrained and drained loading, can be approximated by measuring V_s by using field methods.

Figure 4-4 presents the evolution of normalized mean effective stress $\left(p'/p'_0\right)$ and normalized shear wave velocity during triaxial testing $\left(V_s/V_{s0}\right)$ of all the tested samples. An automated collection system was used at each point in time to estimate a single shear-wave travel time and consequently determine V_s. Because only one measurement was taken each time, signal stacking was not implemented during the triaxial testing. Signal stacking requires measuring the output signal multiple times and averaging the recorded signals to improve the signal-to-noise ratio and to determine a more reliable shear-wave travel time. For the undrained tests, the output signals were consistent, as observed by the smooth variation of $\left(V_s/V_{s0}\right)$ in Figure 4-4 (a), Figure 4-4(c), and (e). For the drained tests, a lower signal-to-noise ratio was observed, as seen in Figure 4-4 (b), (d), and specially Figure 4-4(f) by the sudden changes in $\left(V_s/V_{s0}\right)$ in some deformation values. However, discernible patterns can be extracted from the measured data in both test conditions.

In Figure 4-4, for the samples of material S1, some V_s measurements were not taken during shearing. The gap between the V_s measurements was connected with straight lines to show the measured trend. In Figure 4-4 (b), this corresponds to emptying the triaxial pump to accommodate the volume changes in the sample for S1_d. In the undrained tests, Figure 4-4 (a), (c), and (e) show the results for samples S1_u, S2_u, and S3_u, respectively. The normalization pairs $\left(p'_0, V_{s0}\right)$ for S1_u, S2_u, and S3_u were $\left(204.7\ kPa, 233.5\, m/s\right), \left(207.3\ kPa, 234.8\, m/s\right)$, and $\left(205.3\ kPa, 212.3\, m/s\right)$, correspondingly. Notice that the target p'_0 in all the tests was $206.9\ kPa$; however, slight variations with respect to this value were observed as the corresponding V_{s0} values were taken some seconds after the beginning of shearing. The maximum variation between the target p'_0 and the first p'_0 value corresponding to the V_{s0} was 1.03%.

In the undrained tests, decay in both normalized quantities with increasing axial strain is observed. This behavior is consistent with the development of excess pore pressures and reduction in confining pressure p'. Nevertheless, a disparity in the behavior was noticed. The normalized mean effective stress reached a minimum value between 4% and 6%. This minimum corresponds to the point at which the samples reached the critical state. After this point, p'/p'_0 increases as the samples follow the critical state line. This behavior is not observed in the normalized shear wave velocities; after this point, the measured V_s/V_{s0} values seemed to reach a plateau value. In all cases, the reduction in p'/p'_0 was most significant than the reduction in V_s/V_{s0} at the end of the tests. While p' decreased between 54% and 67%, the shear wave just decreased between 24% and 34%. In general, at the end of the test p'/p'_0 was around half of V_s/V_{s0}.

Figure 4-4 (b), (d), and (f) show the observed evolution of p'/p'_0 and V_s/V_{s0} in the drained tests. The initial conditions (p'_0, V_{s0}) for S1_d, S2_d, and S3_d were taken as $(211.2\ kPa, 231.1 m/s)$, $(207.0\ kPa, 227.8 m/s)$, and $(214.1\ kPa, 209.3 m/s)$, correspondingly. Like the undrained tests, both normalized variables follow a common trend. As the axial strain increased up to 16% around failure, normalized shear wave and mean effective stress increased monotonically. After this point, both variables p'/p'_0 and V_s/V_{s0} decreased simultaneously. This behavior highlights a closer agreement between p'/p'_0 and V_s/V_{s0} for the drained tests. While the mean effective stress increased between 28% and 32%, the shear wave velocity increased between 17% and 31% from the beginning of shearing until the peak value in p'/p'_0 was reached. Based on all test results, V_s/V_{s0} exhibited a smaller range of variation than p'/p'_0. Notice that the previous discussion did not refer to the effect of e_0 in the shear wave measurements. This fact was not considered in the functional relationships presented in the next sections between p'/p'_0 and V_s/V_{s0} are assumed to take this reported effect implicitly.

Dutta et al. (2021) observed the variation of V_s through drained triaxial compression tests on loose, medium, and dense sands. A distinctive peak in the shear wave

velocities was associated with the strain at which the samples transitioned from contraction to dilation. For the test conducted here, dilation behavior was not observed as the samples were normally consolidated. The peak in V_s was associated with the peak in mean effective stress. However, in all the cases, a drop in V_s was observed after the peak. For the medium and dense sands, this drop in V_s rendered the measured velocities to values less than the initial conditions. This prominent variation in V_s was not observed in the tests herein. In all the cases, the V_s at the end of the test was larger than the one at the beginning of shearing.

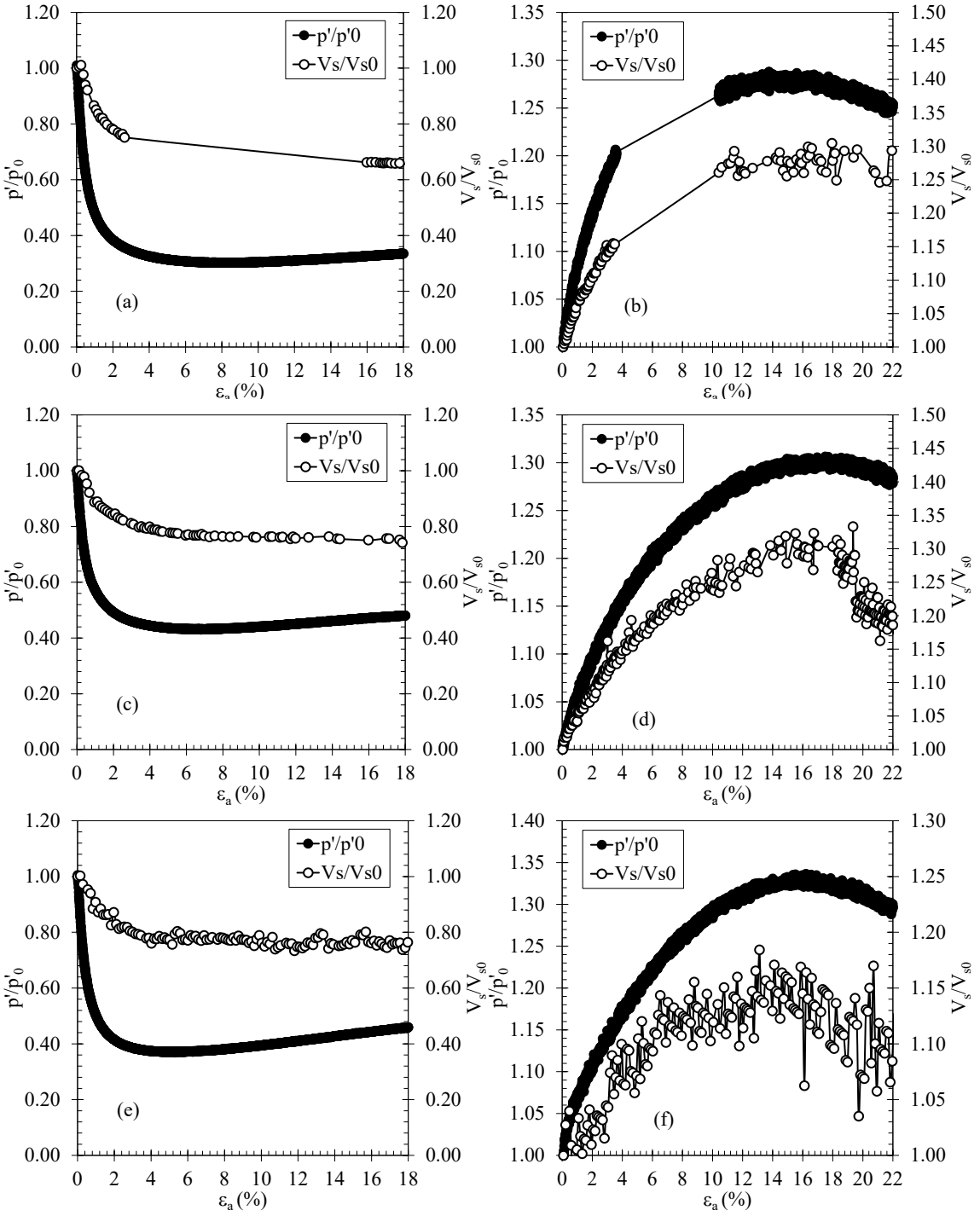

Figure 4-4 Evolution of normalized mean effective stress p' and shear wave velocity Vs during triaxial testing for samples: (a) S1_u; (b) S1_d; (c) S2_u; (d) S2_d; (e) S3_u; (f) S3_d.

Figure 4-5 shows the variation of the normalized variables p' and V_s. As previously noted, a similar behavior was observed for the three different materials. As

observed in this figure in the open circles, the undrained behavior is consistent with the reported by Muttashar and Bryson (2020) and can be described by Eq (1). This equation captures the monotonic reduction in both variables as undrained shearing occurs. However, the use of this equation to represent the observed drained behavior is not satisfactory. This equation will suggest a disproportionate increase in p'/p'_0 with minor variations in V_s/V_{s0} during drained loading.

Because of the axes' definition in Figure 4-5, the typical power function $\left[V_s = \alpha \cdot (p')^{\beta}\right]$ used by several researchers (Santamarina et al. 2001{Cha, 2014 #3)} to relate shear wave velocities and mean effective stress plots with an opposite curvature, this curvature is more pronounced in the undrained tests than in the drained. Although the material behavior after failure is not strictly considered in the following analyses, the relative variation of V_s/V_{s0} with respect to p'/p'_0 exhibited two distinctive responses as seen in Figure 4-5. For drained shearing, after the material reaches its maximum p'/p'_0, there is a significant decrease in V_s/V_{s0} with respect to measured p'/p'_0 values. The opposite response is exhibited in undrained loading, V_s/V_{s0} remains nearly constant while p'/p'_0 increased.

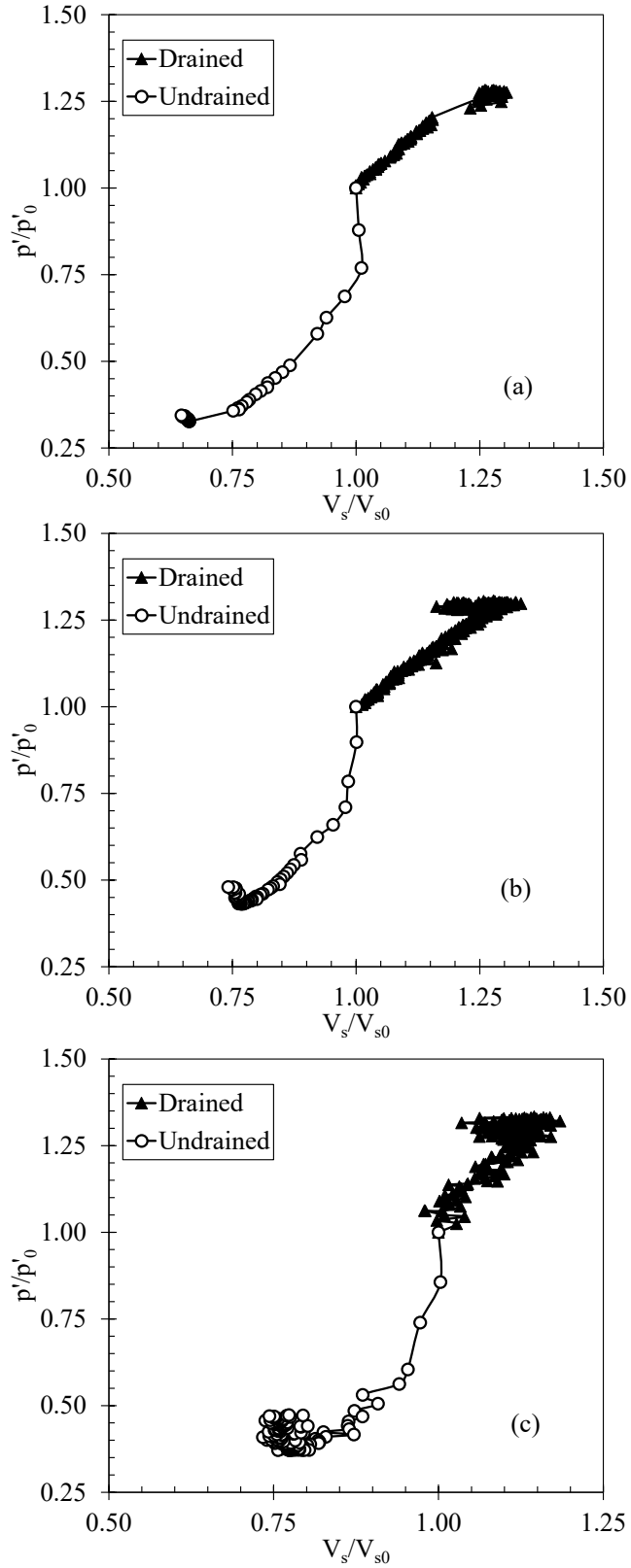

Figure 4-5 Observed variation of normalized mean effective stress p' versus normalized shear wave velocity Vs for: (a)S1; (b) S2; and (c) S3

To describe both regimes, undrained and drained triaxial compression, the calculated values p'/p'_0 and V_s/V_{s0} in Figure 4-5 were taken until the failure points, as shown in Figure 4-6 with the legend data. Then, a curve was fitted through the previous points. The following curve definition provided a satisfactory agreement with the measured data.

$$\frac{p'}{p'_0} = C_1 + \frac{C_2}{\left(\frac{C_4 V_{s0}}{V_s}\right)^{C_3} + 1} \tag{4-2}$$

C_1, C_2, C_3 and C_4 are fitting coefficients to describe the variation of both normalized variables. Table 4-2 presents the collected coefficients for the three materials tested under undrained and drained conditions. From Figure 4-6, it is observed a satisfactory agreement between the measured data and the predicted with Eq. (4-2) until the maximum p'/p'_0 in drained loading and minimum p'/p'_0 in undrained loading. Although the curves do not pass strictly through the initial conditions represented in by the point $(1,1)$, they are very close to this point, as seen in Figure 4-6. This discrepancy might be attributed to slight variations in the void ratios for each material at the beginning of the undrained and drained tests.

It is recognized the power relationship between mean effective stress and shear wave velocity is well represented by Eq (2) in the undrained tests. On the other hand, Eq (2) will describe an opposite curvature for the drained portion of the curve (p'/p'_0 >1), especially near the failure point of the sample in the drained triaxial (maximum p' and q), as the values of V_s/V_{s0} keep increasing without significant change in normalized p'. A modification to the original shape described by Eq. (4-2) is presented in the following section to increase the predicting capabilities of the presented approach.

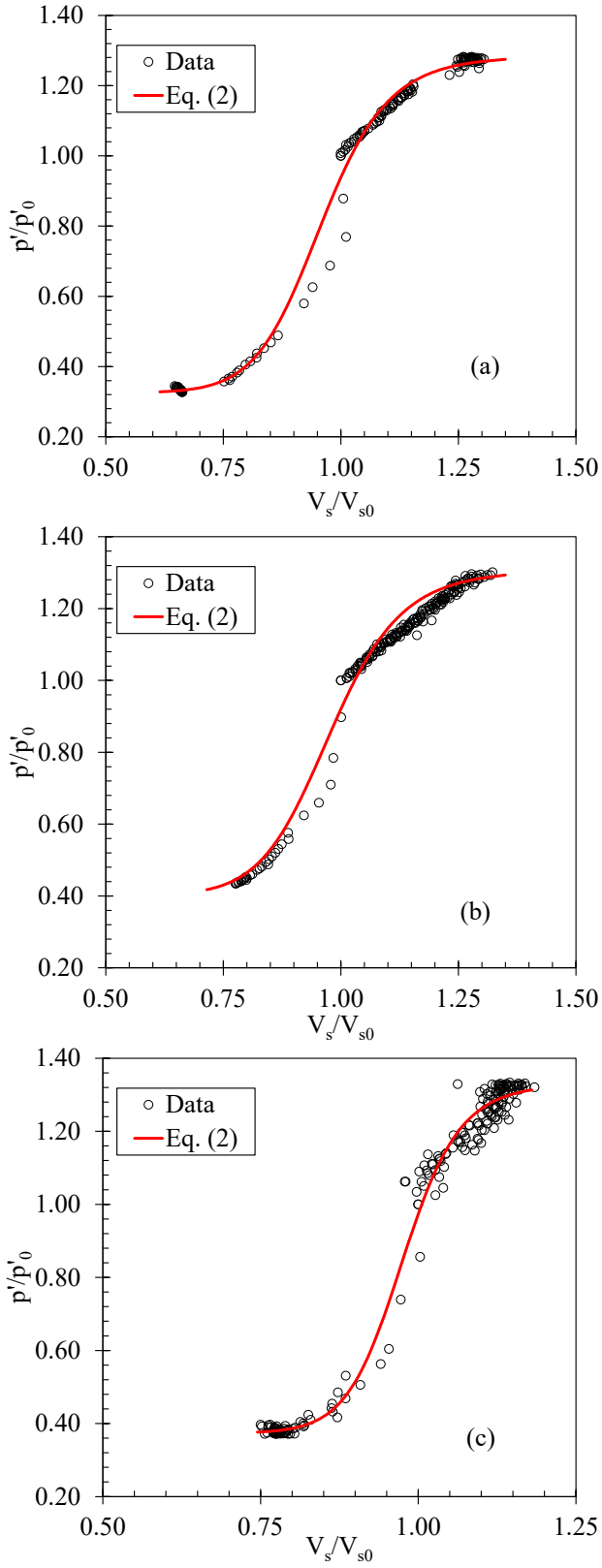

Figure 4-6 Fitted curve through measured normalized variables p' and Vs for: (a)S1; (b) S2; and (c) S3

Table 4-2 Collected coefficient using Eq. (4-2) for the measured data

Sample Material	C1	C2	C3	C4	R^2
S1	0.37654	0.92533	23.31907	0.97417	0.988
S2	0.40192	0.87784	12.92395	0.97777	0.992
S3	0.37387	0.95471	21.65260	0.97611	0.996

To evaluate the usefulness of Eq. (4-2) for other soils. It was fitted through the dataset presented by Muttashar and Bryson (2020). This dataset included only undrained triaxial tests; therefore, a bounding value was necessary to fit Eq. (4-2). This value was taken as the average failure point in the drained tests conducted in this study. Thus, the point $p'/p'_0 = 1.3 \quad V_s/V_{s0} = 1.24$ was added to the Muttashar and Bryson (2020) measurements. Figure 4-7 shows the predicted variation of the normalized variables with Eq. (4-2) and the reported for sample 1. As seen from this figure, Eq. (4-2) successfully capture the variation of both variables in the undrained portion of the curve. The bounding point in the drained portion of the curve was also added to the figure. A similar process was used for the other samples reported by (Muttashar and Bryson 2020); Table 4-3 presents the estimated coefficients of Eq (2) for this dataset. As observed by the high coefficient of determination, Eq (2) is appropriate to establish the relationship between normalized shear wave and mean effective stress.

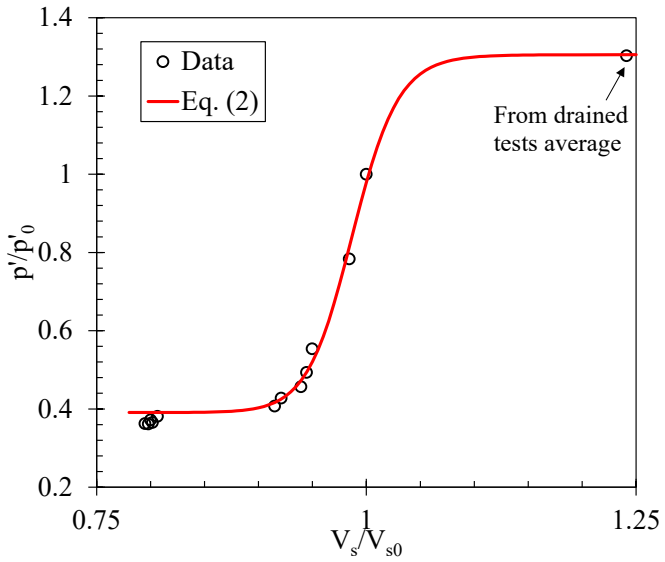

Figure 4-7 Eq. (4-2) fitted through data (Sample 1) from Muttashar and Bryson (2020).

Figure 4-8 shows the effect of each parameter on the curve represented by Eq. (4-2). C_1 controls the lower limit of the curve (Figure 4-8 (a)); therefore, it is related to the undrained behavior of the material. C_2 reflects the material behavior on drained testing as it limits the upper portion of the curve, as seen in Figure 4-8 (b). C_3 represents the slope of the transition behavior between undrained and drained triaxial testing. Finally, C_4 represents a horizontal translation on the entire curve because of the normalization process at the beginning of triaxial with respect to initial conditions V_{s0} , and p'_0, this coefficient should be close to 1.0, as confirmed by the estimates in Table 4-2 and Table 4-3.

Table 4-3 Collected coefficient using Eq. (4-2) with data from Muttashar and Bryson (2020)

Sample	C1	C2	C3	C4	R^2
S#1	0.371	0.935	43.300	0.986	0.996
S#2	0.443	0.866	141.153	0.997	0.989
S#3	0.355	0.950	130.364	0.994	0.984
S#4	0.425	0.880	40.281	0.986	0.995
S#5	0.380	0.931	20.218	0.969	0.998
S#6	0.328	0.987	16.698	0.956	0.996
S#7	0.360	0.948	32.832	0.981	0.994
S#8	0.289	1.026	17.621	0.958	0.998

Now that a function that relates shear waves with mean effective stresses has been established, a constitutive model can be used to obtain the relationship between normalized shear wave velocities and other triaxial measurements as strains (volumetric, deviatoric), stress (deviatoric), and excess water pressures. This study will use a Hypoplastic clays model to estimate triaxial behavior based on measured shear wave variation. The analysis presented herein corresponds to normally consolidated soils.

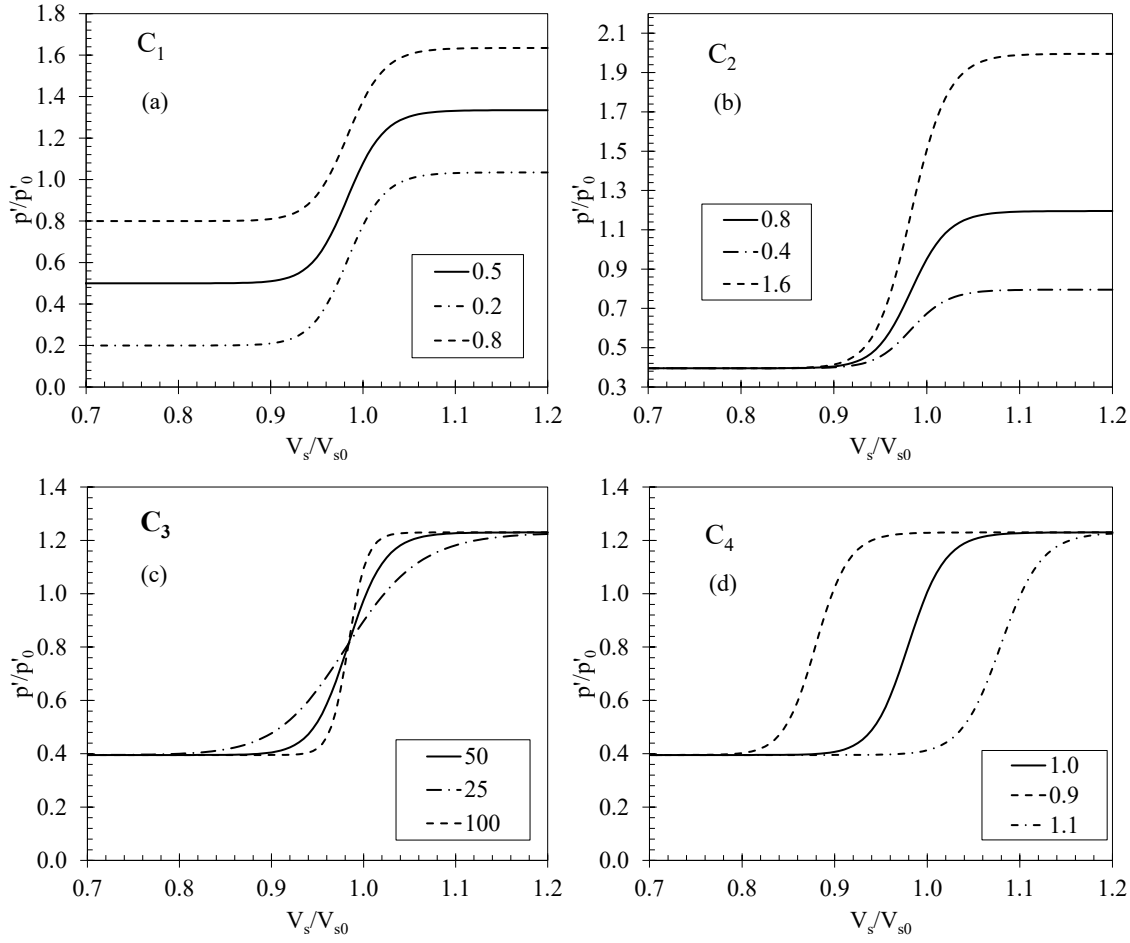

Figure 4-8 Parameter's interpretation (a) C_1; (b) C_2;(c) C_3; and (d) C_4

4.5 HYPOPLASTIC BASIC MODEL

The hypoplasticity constitutive model for clays proposed by Mašín (2005) is an advanced model that uses the basic principles of critical state soil mechanics to predict the different features of soil behavior as critical state, stiffness upon loading and reloading, the influence of over consolidation on peak strength (Mašín 2009). Because the model is not based on an elastoplastic framework, strains are not decomposed into elastic and plastic components. The yield function distinguishing between loading and unloading is not adopted. This model requires only five parameters, namely ϕ_c, N, λ^*, κ^* and r. ϕ_c is the friction angle at the critical state. The parameters N and λ^* control the position of the virgin compression line; κ^* defines the bulk modulus at over consolidation states. r

controls the shear modulus. The hypoplastic constitutive equation (Mašín 2005)is described by a non-linear tensorial equation that relates the stress rate with strain rate as

$$\dot{\sigma} = f_s \boldsymbol{L} : \dot{\varepsilon} + f_s f_d \mathbf{N} \left\| \dot{\varepsilon} \right\| \tag{4-3}$$

Where $\dot{\sigma}$ is the stress rate, $\dot{\varepsilon}$ is the strain rate, $\boldsymbol{L}$ and $\mathbf{N}$ are constitutive tensors of fourth and second order, respectively. f_s and f_d are scalar factors that depend on the state variables σ and void ratio e. The scalar quantity $\left\| \dot{\varepsilon} \right\|$ is the Euclidian norm of the tensor $\dot{\varepsilon}$. The tensorial formulation given by Eq. (4-3) can be simplified for axisymmetric conditions (i.e., triaxial testing) using the procedure highlighted by Niemunis (2002) and the stress invariants mean effective stress rate $\dot{p}'$ and deviatoric stress rate $\dot{q}$

$$\dot{p}' = \left(\dot{\sigma}'_1 + 2\dot{\sigma}'_3 / 3 \right) \text{ and } \dot{q} = \dot{\sigma}'_1 - \dot{\sigma}'_3 \tag{4-4}$$

where $\dot{\sigma}'_1$ and $\dot{\sigma}'_3$ correspond to the axial and radial effective stress rates. The volumetric and deviatoric strain rates are defined as

$$\dot{\varepsilon}_v = \dot{\varepsilon}_1 + 2\dot{\varepsilon}_3 \text{ and } \dot{\varepsilon}_s = 2/3\left(\dot{\varepsilon}_1 - \dot{\varepsilon}_3 \right) \tag{4-5}$$

where $\dot{\varepsilon}_1$ and $\dot{\varepsilon}_3$ correspond to the axial and radial strain rates.

According to Niemunis (2002), Eq. (4-3) can then be written as

$$\dot{t} = f_s \overline{\boldsymbol{L}}\, d + f_s f_d \overline{\mathbf{N}} \sqrt{d^T \mathrm{C}\, d} \tag{4-6}$$

where $\dot{t} = \begin{Bmatrix} \dot{p}' \\ \dot{q} \end{Bmatrix}$, $d = \begin{Bmatrix} \dot{\varepsilon}_v \\ \dot{\varepsilon}_s \end{Bmatrix}$, and $\mathrm{C} = \begin{bmatrix} \frac{1}{3} & 0 \\ 0 & \frac{3}{2} \end{bmatrix}$

By substituting the previous definition of invariants into the original formulation given by Mašín (2005). The constitutive tensors $\overline{\boldsymbol{L}}$ and $\overline{\mathbf{N}}$ can be simplified for axisymmetric conditions as

$$\overline{\boldsymbol{L}} = \begin{bmatrix} \dfrac{c_2 a^2}{3} + c_1 & \dfrac{c_2 \eta a^2}{3} \\ \dfrac{c_2 \eta a^2}{3} & \dfrac{9c_1}{2} + \dfrac{c_2 \eta^2 a^2}{3} \end{bmatrix} \tag{4-7}$$

$$\overline{\boldsymbol{N}} = \begin{bmatrix} \dfrac{\left(\left(\left(-4c_2\eta^2 - 9c_2\right)F^2 + 2c_1\eta^2\right)Ya^3 - 27c_1F^2Ya\right)\sqrt{3}}{\left(\left(2\eta^2+9\right)Fa^2 + 27F^3\right)\sqrt{\dfrac{\left(4\eta^4+18\eta^2\right)a^6 + 108\eta^2F^2a^4 + \left(648\eta^2+729\right)F^4a^2}{\left(4\eta^4+36\eta^2+81\right)F^2a^4 + \left(108\eta^2+486\right)F^4a^2 + 729F^6}}} \\ \dfrac{\left(\left(\left(-4c_2\eta^3 - 9c_2\eta\right)F^2 - 9c_1\eta\right)Ya^3 - 54c_1\eta F^2Ya\right)\sqrt{3}}{\left(\left(2\eta^2+9\right)Fa^2 + 27F^3\right)\sqrt{\dfrac{\left(4\eta^4+18\eta^2\right)a^6 + 108\eta^2F^2a^4 + \left(648\eta^2+729\right)F^4a^2}{\left(4\eta^4+36\eta^2+81\right)F^2a^4 + \left(108\eta^2+486\right)F^4a^2 + 729F^6}}} \end{bmatrix} \tag{4-8}$$

where $\eta = q/p'$ is the current stress ratio. To implement the model by (Mašín 2005), additional variables are required. The additional variables a, F, Y, c_1 and c_2 defined in the original publication of the model and shown in Eq (7) and Eq (8) are given in the supplemental equations of this chapter .

In the presented approach, the mean effective stress p' is the main input for the calculation as this is derived from the measurement of shear wave velocities using Eq. (4-2). In drained analysis, the calculation is stress-controlled as the mean effective stress and mean deviatoric stress rates are known. On the other hand, in undrained analysis, the calculation is considered mixed controlled as the mean effective stress rate and the volumetric strain rate are known quantities. For both situations, Eq. (4-6) must be solved incrementally for the vector of strain increments d. The next section will highlight the procedure to obtain the complete triaxial response based on input. Because the model does not include any rate dependency in the constitutive tensors $\overline{\boldsymbol{L}}$ and $\overline{\mathbf{N}}$, strain and stress rates are analogous to strain and stress increments.

4.6 DRAINED TRIAXIAL CONDITIONS

In this case, $\dot{t}$ is completely known as $\dot{q} / \dot{p}' = 3$. For a small increment in stresses represented by the vector $\dot{t}$, Eq (6) is solved for d (i.e., strain increments), as shown by Niemunis (2002). By using the current stress conditions, the following variables are defined

$$\overline{\boldsymbol{A}} = f_s \overline{\boldsymbol{L}}^{-1} \dot{t} \tag{4-9}$$

$$\overline{\boldsymbol{B}} = f_s f_d \overline{\boldsymbol{L}}^{-1} \overline{\mathbf{N}} \tag{4-10}$$

Then, the variable x is determined as the positive root of the quadratic equation

$$a_{coeff} x^2 + b_{coeff} x + c_{coeff} = 0 \tag{4-11}$$

with $a_{coeff} = \overline{B}^T C \ \overline{B} - 1, b_{coeff} = -\left(\overline{A}^T C \ \overline{B} + \overline{B}^T C \ \overline{A} \right)$, and $c_{coeff} = \overline{A}^T \ C \ \overline{A}$. Finally, d is given as

$$d = \overline{A} - x\overline{B} \tag{4-12}$$

with the vector d determined, the values of the current strains can be determined as

$$\varepsilon_v = \varepsilon_{v_{prev}} + \dot{\varepsilon}_v \tag{4-13}$$

$$\varepsilon_s = \varepsilon_{s_{prev}} + \dot{\varepsilon}_s \tag{4-14}$$

where $\dot{\varepsilon}_v$ and $\dot{\varepsilon}_s$ are the components of the vector d. $\varepsilon_{v_{prev}}$ and $\varepsilon_{s_{prev}}$ are the previous values of strain components. The invariants p' and q are updated based on previously defined stress increment $\dot{t}$.

$$p' = p'_{prev} + \dot{p}' \tag{4-15}$$

$$q = q_{prev} + \dot{q} \tag{4-16}$$

The change in the void ratio is determined as $de = -(1+e)\dot{\varepsilon}_v$.

4.7 UNDRAINED TRIAXIAL CONDITIONS

The mean effective stress $\dot{p'}$ is known in this case, but the deviatoric stress rate is $\dot{q}$ unknown. Because there is no volume change during undrained loading, $\dot{\varepsilon}_v = 0$. Eq (6) is then solved for $\dot{q}$ and $\dot{\varepsilon}_s$. We define the variables

$$P = f_s \overline{L}_{1,1}^{-1} \left(\dot{p} \right) \tag{4-17}$$

$$Q = f_s f_d \overline{L}_{1,2}^{-1} \overline{N}_1 \tag{4-18}$$

The variable x is determined by solving Eq (11) with the following coefficients $a_{coeff} = Q^T C_{2,2}\ Q - 1$, $b_{coeff} = -\left(P^T C_{2,2} Q + Q^T C_{2,2} P \right)$, and $c_{coeff} = P^T C_{2,2} P$.

The required quantities $\dot{q}$ and $\dot{\varepsilon}_s$ are given as

$$\dot{\varepsilon}_s = P - Qx \tag{4-19}$$

$$\dot{q} = f_s \overline{L}_{2,2}\, \dot{\varepsilon}_s + \overline{N}_2 x \tag{4-20}$$

4.8 MODELING OF THE COMPRESSION TRIAXIAL TESTING

4.8.1 Undrained compression tests

With the constitutive model previously presented and the relationship between normalized shear waves and normalized mean effective stress defined by Eq. (4-2), the variation of normalized shear waves and triaxial measurements can be obtained for a given set of material parameters. The hypoplastic clay parameters (N, λ^*, κ^*) for the tested samples were estimated based on the online application ExCalibre (Kadlíček et al. 2022). However, it was observed that a value of the parameter κ^* between 2-3 times the given by ExCalibre better represents the measured data. Additionally, the parameter r used in this study was approximated based on the obtained estimated values of λ^*, κ^* and ν given by ExCalibre. The ϕ_c was calculated based on the measured data. Table 4-4 presents the input parameters used in calculating the triaxial response in the six samples (i.e., two for each

material type). In this table, the suffix _ u and _d refer to the undrained and drained tests, respectively.

Table 4-4 Input parameters for the calculation of triaxial response

Sample	ϕ_c	N	λ^*	k^*	r	e_0
S1_u	19.10	0.577	0.018	0.004	0.40	0.62
S1_d	18.40	0.570	0.020	0.004	0.40	0.61
S2_u	19.53	0.657	0.044	0.004	0.21	0.53
S2_d	19.50	0.657	0.044	0.004	0.40	0.52
S3_u	20.40	0.554	0.025	0.004	0.19	0.54
S3_d	21.21	0.590	0.025	0.007	0.19	0.59

Figure 4-9 presents the measured, and the estimated undrained response for sample S3_u as this is representative of the observed behavior in undrained loading. The corresponding stress-strain curve and the stress path are shown in Figure 4-10. Figure 4-9 (a) shows the variation of axial strain ε_a, which for undrained loading is equal to ε_s, and V_s/V_{s0}. From the figure, predicted and measured axial strains are very close up to an ε_a of 1.5%. After this point, a greater change of V_s/V_{s0} is associated with strain until the axial strain of 2.21%. At this point, the sample reaches the critical state line defined by ϕ_c and observed in the leftmost point of the predicted stress path shown in Figure 4-10 (b).

On the other hand, the critical state line is reached around an ε_a of 4% based on the measured data. By using the previous formulation of the hypoplastic model, the point of failure is determined by observing the variable x. Imaginary values of x will be calculated for p' values less than the one given at the critical state line. Notice that in Figure 4-9(a), a straight dashed line was added at the predicted failure point to illustrate the variation of V_s/V_{s0} based on the measured response. As seen in the measured data, there are minor variations of V_s/V_{s0} while the sample continues straining after failure. Figure 4-9(b) shows the measured and predicted deviatoric stress. Concerning the normalized shear wave, the measured response is slightly stiffer at the beginning of shearing; however, both curves exhibit the same behavior. It is observed in Figure 4-9 (b) that the predicted response reaches a constant value of q; this value corresponds to the value at the critical state line when the failure occurs. After this point, the stress-strain curve can be

approximated by the dashed line shown in Figure 4-10 (a), which represents critical state conditions. Notice that the presented triaxial test results correspond to a strain-controlled test; therefore, it is possible to obtain measurements well after the material has reached failure. In Figure 4-10 (b), the measured stress path shows an increase in the deviatoric stress as the sample follows the critical state line. This behavior, after failure, is reflected in Figure 4-9 (b) by an increase in q with minor variations of V_s/V_{s0} . Because the proposed methodology is stress-controlled, the calculation process ends at failure at the critical state line.

Figure 4-9 (c) shows the variation of the excess pore pressure and normalized shear wave velocity. As seen from the figure, there is close agreement between the measured and predicted response until the failure of the sample. Nonetheless, there is a decrease in the measured excess pore pressure, which is not captured by the proposed method as it represents post-failure behavior.

The estimated stress path for undrained test S3_u is shown in Figure 4-10 (b). A close agreement between the calculated and the measured data is observed, with a slightly stiffer response of the predicted data. It is convenient to highlight that the presented approach is closely linked to the constitutive model used. As long as the constitutive model provides a satisfactory representation of the soil behavior, the presented approach will give an acceptable description of the soil response.

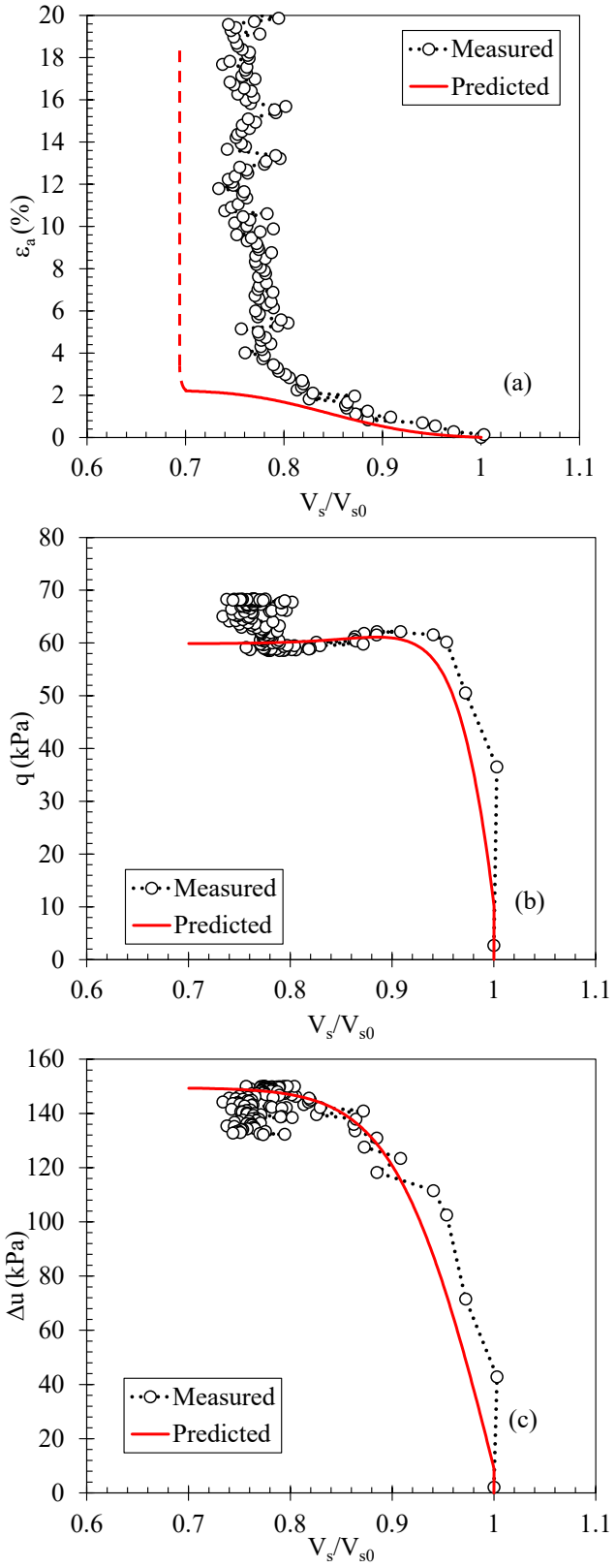

Figure 4-9 Predicted and measured undrained triaxial test response (S3) in terms of: (a) axial strain $\varepsilon_a=\varepsilon_s$;(b) deviatoric stress; and (c) excess pore water pressure Δu

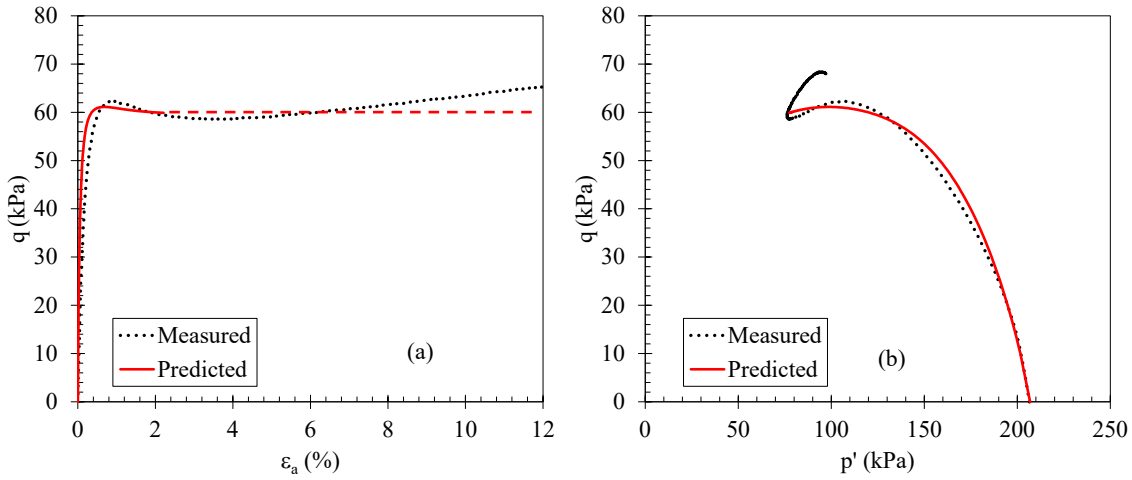

Figure 4-10 Predicted and measured undrained stress-strain response for S3

4.8.2 Drained compression tests

As previously stated, Eq (2) has a couple of drawbacks in the domain of normalized shear wave representing drained testing (i.e., $V_s/V_{s0} > 1$). First, the curvature of Eq. (4-2) for V_s/V_{s0} near failure of the material is oppositive to the commonly observed power relationship between effective stresses and shear wave velocities. Second, because the curve is asymptotic to the normalized value $p'/p'_0 = C_1 + C_2$, the calculated values of p' from measured wave velocities and used for the calculation of the other test measurements $\varepsilon_a, \varepsilon_{vol}, q$, may not represent the material behavior until failure.

The following modification to the function given by Eq. (4-2) is proposed. First, Eq. (4-2) is fitted through the measured data. Second, the horizontal point $\left(V_s/V_{s0}^*\right)$ at which p'/p'_0 is equal to $0.95 \cdot (C_1 + C_2)$ is determined. Finally, each value in the original curve represented by Eq. (4-2) and greater than V_s/V_{s0}^* is reflected with respect to a straight line starting at V_s/V_{s0}^* and with a slope of $m = 1$. The procedure is given as follows: Determine the constant c as

$$c = p'/p'^*_0 - V_s/V_{s0}^* \tag{4-21}$$

where $p'/p'_0{}^{*} = 0.95 \cdot (C_1 + C_2)$. For each normalized wave velocity point within the interval of interest $\left(V_s/V_{s0} > V_s/V_{s0}{}^{*}\right)$, calculate the variable d

$$d = \frac{V_s/V_{s0} - p'/p'_0 - c}{2} \tag{4-22}$$

The transformed coordinates of each point are given as

$$V_s/V_{s0\,(new)} = 2d - V_s/V_{s0} \tag{4-23}$$

$$p'/p'_{0\,(new)} = 2d - p'/p'_0 + 2c \tag{4-24}$$

Figure 4-11(a) shows the original curve, represented by the dashed line, and the modified, represented by the solid line. Notice that the previous modification procedure only affects the drained portion of Eq. (4-2). Figure 4-11(b) shows the measured normalized variation in S3 as given in Figure 4-6 but with the modified curve. As seen from the figure, a slightly better agreement between the measured data and the predicted is achieved with the previous procedure. In addition, the normalized curve, in conjunction with the constitutive model, will allow the calculation of triaxial behavior until failure.

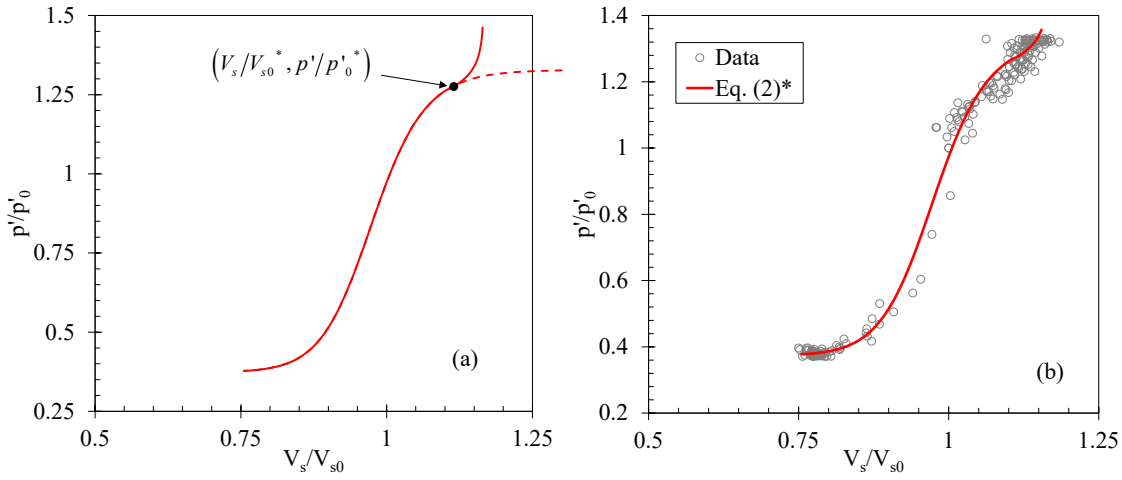

Figure 4-11(a) modified version of Eq.(4-2); (b) S3 data and modified version of Eq. (4-2)

Figure 4-12 presents the measured and predicted response on the drained test for sample S3_d in terms of axial strain, deviatoric stress, and volumetric strain as a function of normalized wave velocity. Figure 4-13 shows the measured and predicted stress-strain curves and volumetric strain variation. Figure 4-12(a) shows the variation of axial strain

ε_a estimated from the calculated ε_v and ε_s based on the presented methodology for drained loading. As seen in the figure, there is good agreement between the measured and predicted behavior. Nevertheless, predicted values tended to be smaller than the measured; this result is reflected in the stiffer response of the predicted stress-strain curve shown in Figure 4-13(a). The initial stiffness of the material and the failure load are correctly estimated by the presented approach (Figure 4-13(a)). The observed discrepancy between measured and predicted behavior is closely related to the constitutive model used. More advanced formulations of the hypoplastic model may give a better match between measured and predicted responses.

Figure 4-12(b) shows the variation of deviatoric stress, q , and normalized shear wave velocities, V_s/V_{s0} . The measured data corresponds to all the normalized velocities until the end of the test. It is observed that V_s/V_{s0} increases until q reaches the failure value of 232.9 kPa at $\varepsilon_a = 15.8\%$. After this point, q decreases to the final value of 194.6 kPa; similarly, V_s/V_{s0} decreases but in a more erratic fashion. This erratic behavior after failure is also seen in Figure 4-12(a) for $\varepsilon_a > 15.8\%$. Volumetric changes measured and predicted by the presented approach are shown in Figure 4-12(c). The variation of the volumetric strain is well represented by the proposed approach, although noticeable discrepancies are observed for volumetric strains between 0.55% and 1.5%. From this figure, it is observed that once the material reaches a state of constant volumetric deformation, in this case $\varepsilon_v \approx 3\%$, there is an extensive variation in the normalized shear wave, V_s/V_{s0} . However, this variation is considered of little significance in this study because it represents conditions beyond the failure of the material.

Figure 4-13(b) shows the simultaneous variation of axial strain and volumetric strain for this drained test. In the figure, the predicted response correctly replicates the measured one. Nonetheless, the measured volumetric strain is between 0.2-%-0.5% less than the predicted, with the maximum values of 3.04% and 3.23% for the measured and predicted response, respectively. The presented approach satisfactorily predicts the axial strain $\varepsilon_a = 10.1\%$ at which the sample exhibited a constant volumetric deformation. The stress path for this test is not presented as this is known, given by a straight line starting at

the initial mean effective stress, p', at the beginning of the test (206.6 kPa) and finishing at the invariant values of 232.9 kPa and 284.12 kPa for p' and q, respectively.

It has been recognized that the void ratio, e, also affects the relationship between effective stresses and shear wave propagation (Hardin and Richart 1963{Santamarina, 2001 #6)}. For undrained loading, as there are no volume changes during the deformation process, effective stresses may have a more direct relation with shear waves. On the other hand, for drained loading, in this study, the explicit effect of e is not V_s defined. It is assumed that this effect is implicit in the coefficients $\left(C_1 ... C_4\right)$ used in Eq. (4-2).

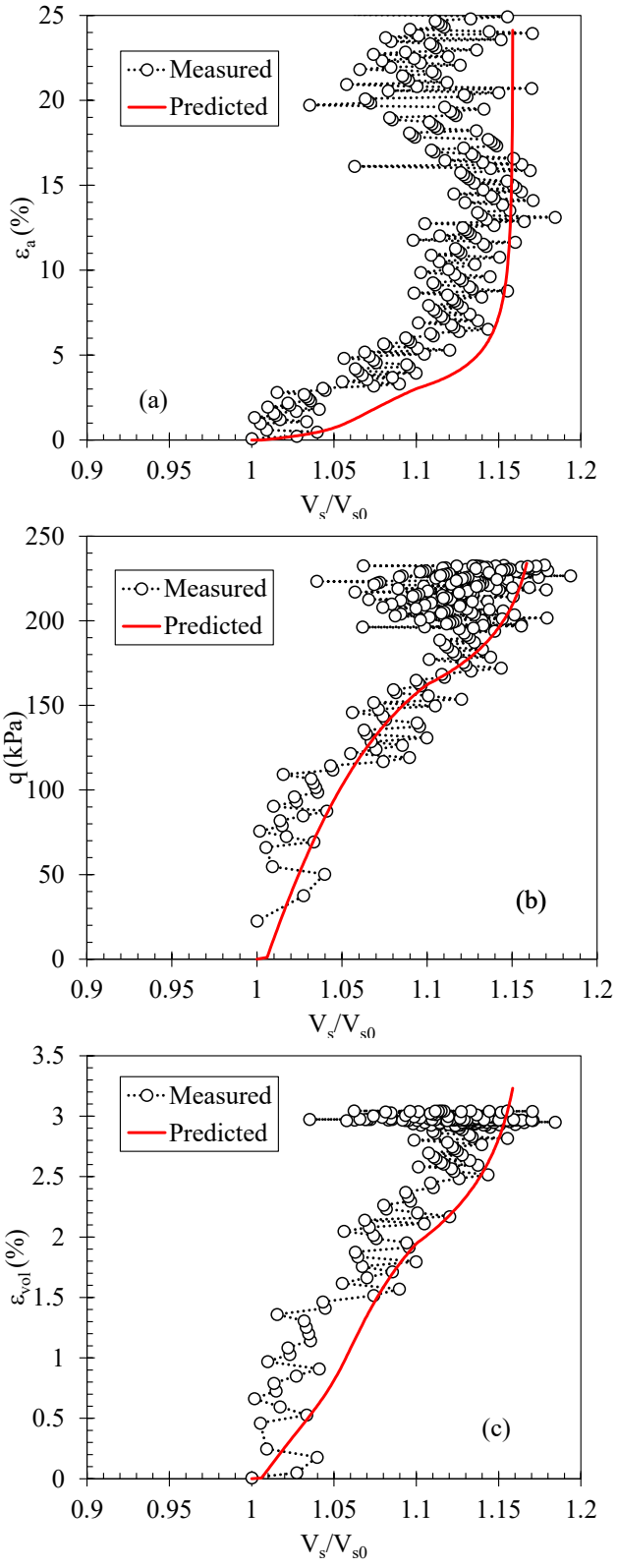

Figure 4-12 Predicted and measured drained triaxial test response (S3_d) in terms of:(a) deviatoric strain ;(b) deviatoric stress; and (c) volumetric strain

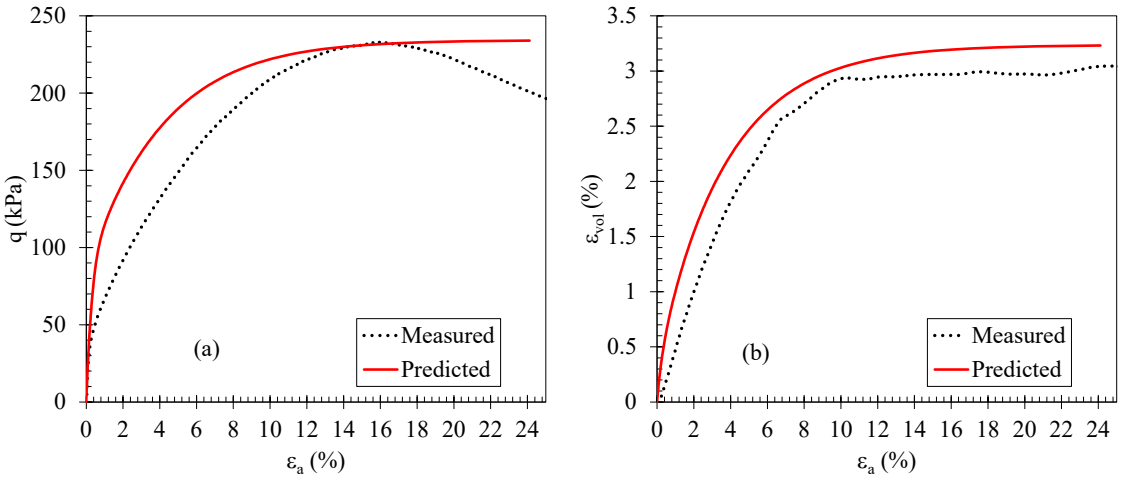

Figure 4-13 Predicted and measured drained stress-strain response for S3_d

4.9 UNDRAINED TRIAXIAL TESTING FROM LITERATURE

The results of two representative triaxial tests conducted by Muttashar and Bryson (2020) using bender elements are presented and compared with the proposed approach in Figure 4-14. The measured stress-strain responses and the stress paths these tests are shown in Figure 4-15 and Figure 4-16, respectively. Samples S#1 and S#8 were selected as they represent the maximum (93.6) and minimum (43.5) percentage of fines, respectively. Table 4-5 summarizes the hypoplastic parameters used in the calculation of the undrained triaxial response. The comparison of the proposed approach for the prediction of the rest of the samples is provided in the supplemental data.

From Figure 4-14, it is observed, in general, a satisfactory agreement between the measured and the predicted results. The variation of deviatoric strain shown in Figure 4-14(a) and Figure 4-14(b) is in good agreement with the measured normalized shear wave velocity. Although for sample S#8, the predicted ε_a did not match the measured after a strain of 2%, as also seen in the stress-strain response shown in Figure 4-15(b). This strain corresponds to the failure of the material. The deviatoric stress, q, is well predicted in both samples until its maximum values are reached, as seen in Figure 4-14(c) and Figure 4-14(d). S#8 exhibited gradual softening behavior after failure. However, this post-failure behavior is not captured with the presented approach, as stress-controlled calculations cannot estimate strain softening during loading. In terms of excess porewater pressures, the predicted results for S#1 are exceedingly well (Figure 4-14(e)). Nonetheless, in sample

S#8, excess pore pressures were underpredicted. A maximum pressure variation of 40 kPa was observed in Figure 4-14 (f).

Figure 4-15 shows the measured and predicted stress-strain curves for the two representative samples from Muttashar and Bryson (2020). In both cases, the predicted initial stiffness of the samples is in excellent agreement with the measured. However, in S#1, as the material moves to failure, the predicted response is slightly stiffer than the measured. In S#8, the tangent stiffness of the material is predicted very well until the maximum deviatoric stress is reached. The predicted stress paths for S#1 and S#8 are shown in Figure 4-16. In sample S#1, the predicted deviatoric stress q is slightly below the measured for a given mean effective stress p' (Figure 4-16(a)). However, this difference is less noticeable near the failure of the sample. In S#8, from the initial p' 345 kPa until a p' value of approximately 300 kPa, q is underestimated. After this point, the deviator stress is slightly overestimated until failure (Figure 4-16(b)). Note that the measured post-failure behavior in S#8 is not captured with the presented formulation.

Table 4-5 Input parameters for the calculation of triaxial response of the samples tested by Muttashar and Bryson (2020)

Sample	ϕ_c	N	λ^*	k^*	r	e_0
S#1	15.3	0.83	0.045	0.007	0.45	0.79
S#2	14.5	0.98	0.079	0.012	0.60	0.69
S#3	14.88	0.70	0.06	0.01	0.36	0.43
S#4	15.3	0.68	0.048	0.012	0.86	0.50
S#5	15.1	0.57	0.031	0.009	0.90	0.49
S#6	21	0.25	0.019	0.004	0.20	0.15
S#7	15.4	0.72	0.056	0.009	0.37	0.50
S#8	13.8	0.38	0.03	0.005	0.35	0.23

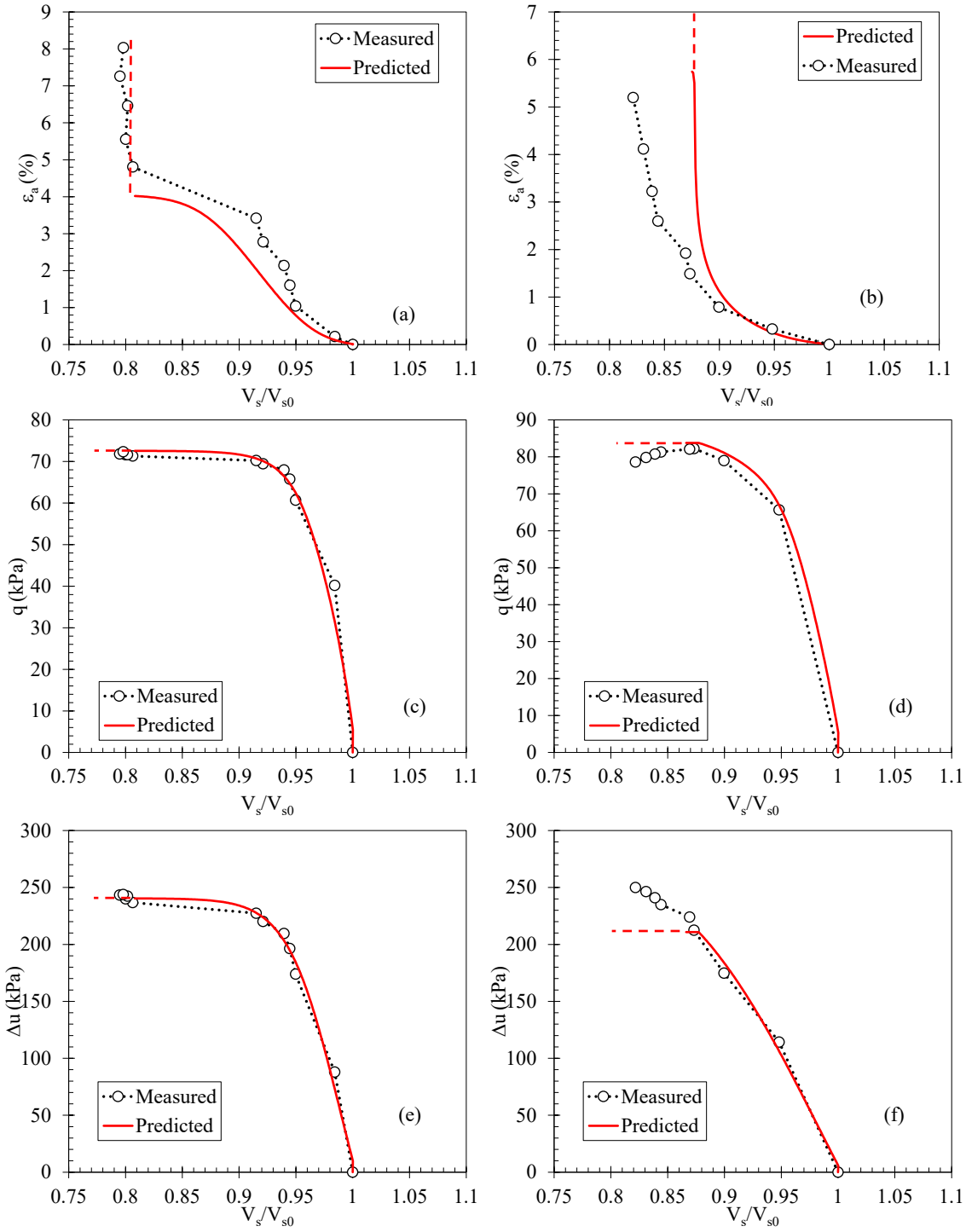

Figure 4-14 Predicted and measured undrained triaxial test response for Samples S1 and S8 (Muttashar and Bryson (2020)) in terms of :(a) and (b) deviatoric strain ;(c) and (d) deviatoric stress; (e) and (f) excess pore water pressure.

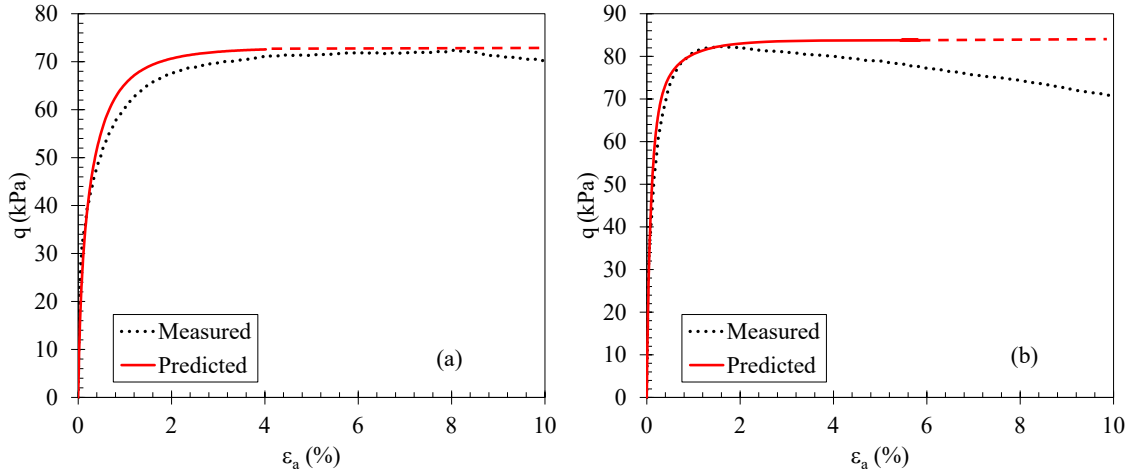

Figure 4-15 Predicted and measured undrained stress-strain response for: (a) S1; and (b) S8

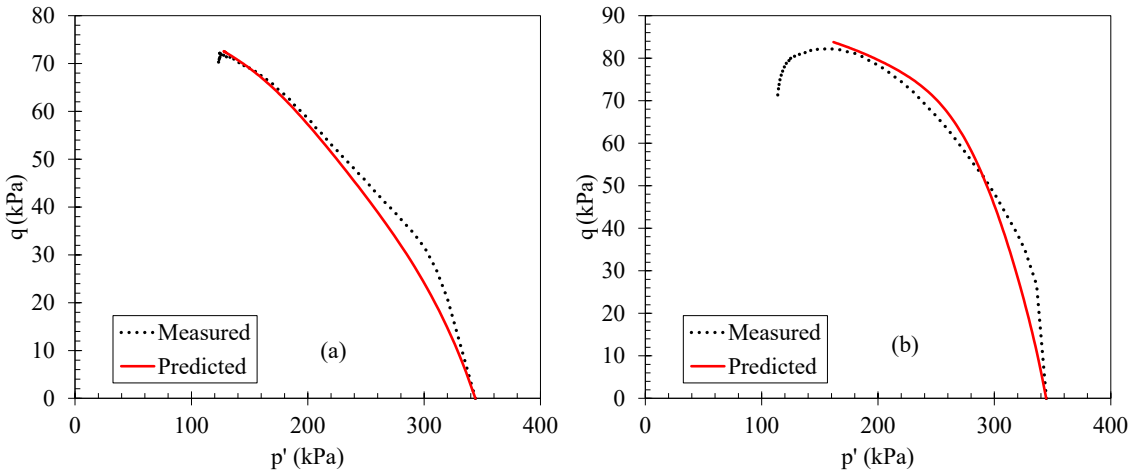

Figure 4-16 Predicted and measured undrained stress path for:(a) S1; and (b) S8

4.10 VARIATION OF NORMALIZED THE COEFFICIENTS C_1, C_2 AND C_3

To provide some guidance in selecting the coefficients used in Eq. (2). Figure 4-17 shows the variation of these coefficients with respect to the material model parameter λ^* and the initial void ratio e_0. The relationship between coefficients is also presented in the figure.

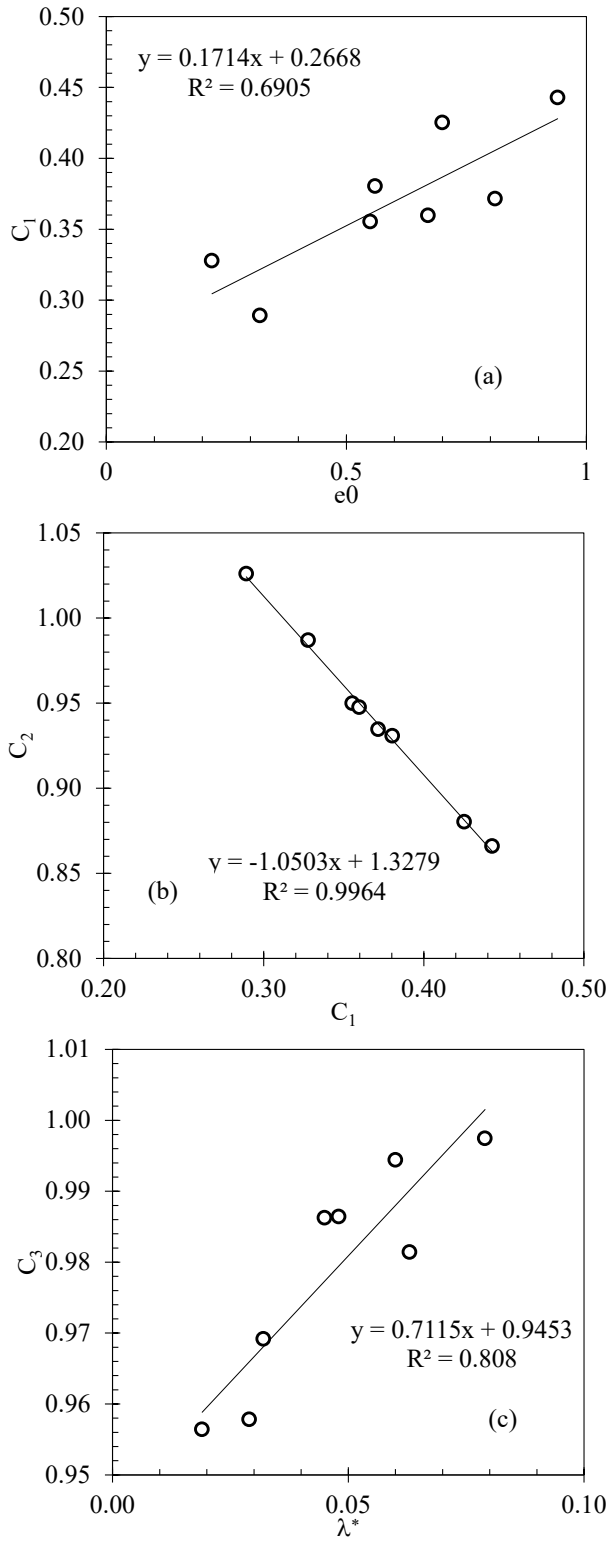

Figure 4-17 Variation of coefficients of Eq (2)

As seen in Figure 4-17 (a), C_1 seems to be related to the initial condition before shearing of the material. At the same time, there is a very clear relationship between C_1 and C_2 for all the samples tested by Muttashar and Bryson (2020). On the other hand, C_3, which controls the slope of the middle portion of the normalized curve, seems to be related to the slope of the normally consolidated line for the soil in consideration λ^*. As these two variables control the stiffness of the material, they are likely to be connected. However, a more conclusive statement is not possible due to the limited points in the dataset. Finally, C_4 can be assumed as 1. A linear relationship is presented for all the coefficients (Table 4-3) in Figure 4-17 to provide a rough estimate in case Eq. (4-2) cannot be developed from laboratory measurements of shear wave velocities V_s. The observed trends are given as

$$C_1 = 0.1714 e_0 + 0.2668 \tag{4-25}$$

$$C_2 = -1.0503 C_1 + 1.3279 \tag{4-26}$$

$$C_3 = 0.7115 \lambda^* + 0.9453 \tag{4-27}$$

4.11 SUPPLEMENTAL EQUATIONS FOR THIS CHAPTER

This section presents the rest of the hypoplastic formulation presented by Mašín (2005) in terms of the invariants p' and q

$$\tan\psi = \frac{\sqrt{2}}{3}\eta \tag{4-28}$$

$$\cos 3\theta = \frac{-\sqrt{6}\cdot\dfrac{2\eta^3}{243}}{\left(\dfrac{2\eta^2}{27}\right)^{3/2}} \tag{4-29}$$

$$F = \sqrt{\frac{1}{8}\tan^2\psi + \frac{2-\tan^2\psi}{2+\sqrt{2}\tan\psi\cos 3\theta}} - \frac{1}{2\sqrt{2}}\tan\psi \tag{4-30}$$

$$f_d = \left(\frac{p'}{p_{cr}}\right)^{\alpha} \tag{4-31}$$

$$p_{cr} = \frac{\exp^{\frac{N-\ln(1+e)}{\lambda^*}}}{2} \tag{4-32}$$

$$a = \frac{\sqrt{3}\left(3-\sin\phi_c\right)}{2\sqrt{2}\sin\phi_c} \tag{4-33}$$

$$\alpha = \frac{1}{\ln 2}\ln\left(\frac{\lambda^*-\kappa^*}{\lambda^*+\kappa^*}\left(\frac{3+a^2}{a\sqrt{3}}\right)\right) \tag{4-34}$$

$$c_1 = \frac{2\left(3+a^2-2^{\alpha}a\sqrt{3}\right)}{9r} \tag{4-35}$$

$$c_2 = 1+\left(1+c_1\right)\frac{3}{a^2} \tag{4-36}$$

$$f_s = \frac{3p'}{\lambda^*\left(-\left(a\cdot 2^{\alpha}\sqrt{3}\right)+a^2+3\right)} \tag{4-37}$$

$$I_1 = 3p' \tag{4-38}$$

$$I_2 = \frac{q^2}{3} - 3p'^2 \tag{4-39}$$

CHAPTER 5
SUMMARY AND CONCLUSIONS

In chapter 2 a deformation-based method for the design of the excavation support systems was proposed. This approach starts with tolerable damage represented as crack width that is assumed to develop only in infill walls. The crack width previously determined was related to the ground distortions based on simplified assumptions of soil-structure interaction. Ground distortion was related to the described relative stiffness ratio R. This ratio takes into consideration the stiffness and strength of the soil, the bending stiffness of the wall, and the excavation stability number.

In the presented approach, the required stiffness of the retaining wall is determined based on tolerable damage, and without the need for iterations in the process. It is advisable to mention that the design procedure proposed in this study applies to excavations in reasonably homogeneous clay deposits and further validation of this methodology is currently pursued by the authors. In cases in which the required section is excessive, as with very small, normalized crack widths, it is recommended to increase the damage tolerance if possible or to improve ground conditions.

Chapter 3 presented a geophysics-based approach was developed to estimate consolidation processes by using shear wave velocity, V_s. By defining the parameters N_{Vs}, λ^*_{Vs} and κ^*_{Vs}, the complete stress history of the material could be approximated based on V_s. The validation of the proposed showed that regardless of the V_s direction and source, the calculated consolidation results were in good agreement with the measured data.

Comparison of the presented approach suggests the approach is acceptable for effective stresses varying between 50 kPa and 2980 kPa. Practical implications of this study are expected in field monitoring of engineering projects. The results of this study are especially applicable to stage construction in soft soils. The presented methodology gives the ability to predict the variation of effectives stresses, which can be correlated to volumetric strains and deformations, based on initial estimation of ground conditions and measurements of V_s. Further investigation of the relationship between the material

parameters N , λ^* and κ^* and the analogous parameters N_{Vs} , λ^*_{Vs} is necessary to improve the relevance of the proposed.

Chapter 4 presented a novel approach to estimating triaxial behavior based on shear wave velocity measurements. A satisfactory agreement was observed between measured and predicted triaxial variables as a function of the normalized shear wave velocity. Nevertheless, a better approximation was obtained for the undrained than drained tests. The performance of the proposed method (i.e., Eq. (4-2)) appears to be limited to the ability of the constitutive model to predict soil behavior. In that sense, the hypoplastic clay model was adequate to model the behavior of the tested materials. To adapt the presented formulation to additional improvements of the hypoplastic model presented here (Mašín 2005). Eq. (4-6)-Eq. (4-20) will need to be redefined for the specific constitutive model. Only normally consolidated samples were studied herein; therefore, for overconsolidated soils, the proposed relationship may not be applicable.

In light of the measured and predicted results comparison, this approach is considered practical for geotechnical field monitoring in which the total stress path of the soil are similar to those obtained in triaxial compression testing. The presented formulation of the hypoplastic model for clays in terms of invariants is practical for spreadsheet implementation. Because the hypoplastic model describe soil behavior in terms of total strains, the presented approach does not allow the calculation of elastic and plastic strains explicitly. Additional aspects of the proposed approach need further investigation. For instance, the normalized relationship between effective stresses and shear wave velocities for triaxial extension testing or other stress paths commonly found in geotechnical engineering practice. In addition, the explicit effect of the void ratio on the proposed normalized curves needs further research, given that the presented results were obtained for a small range of initial void ratios for the different material types.

.

APPENDICES

APPENDIX A

Cost Based Design Considerations for Excavation Support Systems

A.1 INTRODUCTION

A major concern for projects involving deep excavations in urban areas is the potential of excavation-induced damage to adjacent buildings and utilities. Thus, stiff excavation support systems are required to execute the work. Traditional studies focus on the design of these support systems as a function of performance. However, few studies focus on the design of support systems as a function of costs. The objective of this study is to develop a preliminary design approach that relates excavation support system performance design to material and labor costs. This approach contributes to pushing the frontiers of performance-based excavation support systems design by incorporating cost data in the design process.

Construction cost data and other economic parameters for this study were based on bare costs from RSMeans Building Construction Cost Data 2018 (RSMeans, 2018) for sheet pile systems. For this study, a simplified assumption was made that costs increase with increasing weight per area of the excavation support wall element. This assumption is based on the data presented in Table A-1. The table lists three different sheet pile systems characterized by height of the excavation (e.g., 15 ft, 20 ft, 25 ft) and by the weight of the sheet pile per area of the wall (e.g., 22 lbf/sf of wall, 27 lbf/sf of wall, 38 lbf/sf of wall). In Table A-1, the Daily Output represents the typical number of units the designated crew will install in a normal 8-hour day. The Labor Hours represent the number of labor-hours required to install one unit of work (i.e., one square ft). Table A-1 provides the bare costs for driving the sheet pile and leaving it in place and the bare costs to drive, extract, and salvage the sheet pile wall. For this study, it was assumed that the wall would be left in place. The costs associated with installing the supports (e.g., wales, struts, anchors) were assumed to be 20 percent of the total bare cost.

Table A-1 RSMeans 2018 bare cost data for three sheet pile systems based on excavation depth and weight per area of wall.

Sheet Pile System	Daily Output	Labor Hrs.	Material ($/sf)	Labor ($/sf)	Equipment ($/sf)	Total+Supp ($/sf)
15' Excavation, 22 lbf/sf, left in place	983	0.065	18.4	3.41	3.62	30.52
Drive, extract & salvage	545	0.117	5.8	6.15	6.55	
20' Excavation, 27 lbf/sf, left in place	960	0.067	23	3.49	3.71	36.24
Drive, extract & salvage	485	0.132	7.55	6.9	7.35	
25' Excavation, 38 lbf/sf, left in place	1000	0.064	34	3.35	3.56	49.09
Drive, extract & salvage	553	0.116	10.3	6.05	6.45	

Daily output in units of sf/day; sf = square ft; 1 sf/day = 0.093 m^2/day; 1 lbf/sf = 4.883 kg/m^2.

It is acknowledged that the costs presented in this paper only represent the sum of material and installation costs for steel sheet pile walls, driven to limited depths. Additional cost associated with the installations of a sheet pile wall in an urban environment such as the cost for dewatering, excavating in varying soil conditions, and providing support for adjacent infrastructure during the excavation are not included. It is also acknowledged that other types of excavation support systems (e.g., soldier pile and lagging walls, tangent and secant pile walls, diaphragm walls) require different types and quantities of materials and have different labor requirements. Consequently, the costs associated with these other excavation support systems may differ significantly from the costs presented herein. The intent of this effort was not to provide cost data that were highly representative of all excavation support systems and soil conditions. The intent of the study was to provide a basis for a cost-based design approach for excavation support systems.

In order to develop a cost-based design approach that was somewhat independent of time, the bare costs were tied to an economic index that would allow comparison of the current value of a US dollar with the equivalent value of some future US dollar. For this study, the bare costs were adjusted using the US Gross Domestic Product (GDP) deflator index. The GDP deflator is a price index that measures inflation or deflation in an economy by calculating a ratio of nominal GDP to real GDP. The nominal GDP is the market value

of all final goods produced in a geographical region, usually a country. That market value depends on the quantities of goods and services produced and their respective prices. In contrast, real gross domestic product accounts for price changes that may have occurred due to inflation. In other words, real GDP is nominal GDP adjusted for inflation. Real GDP reflects changes in real production. If there is no inflation or deflation, nominal GDP will be the same as real GDP.

The bare costs were adjusted for annual inflation by multiplying the bare costs of the base year (i.e., 2018) by a ratio of the average annual GDP deflator of the future year to the average annual GDP deflator of the base year. This is given as:

$$C_{adj} = C_i \left(\frac{DI_{Fut}}{DI_{Bas}} \right) \tag{A-1}$$

where C_{adj} = the base costs adjusted for annual inflation; C_i = the unadjusted total bare costs; DI_{Fut} = the GDP deflator index for the future year; DI_{Bas} = the GDP deflator index for the base year (i.e., 2018). The average annual deflator index for 2018 was 110.42 and for 2019 it is 112.345. The data provided by RSMeans (i.e., Table A-1) only included three sheet pile sections, characterized by nominal weights (i.e., 107.43 kg/m^2, 131.84 kg/m^2, 185.55 kg/m^2). The applicability of the RSMeans data was extended to other sheet pile sections by fitting a regression line through the data. Fig. A-1 shows the relationships obtained from this effort for the total bare costs and the bare costs normalized with the 2018 deflator index (i.e., C_i / DI_{Bas}).

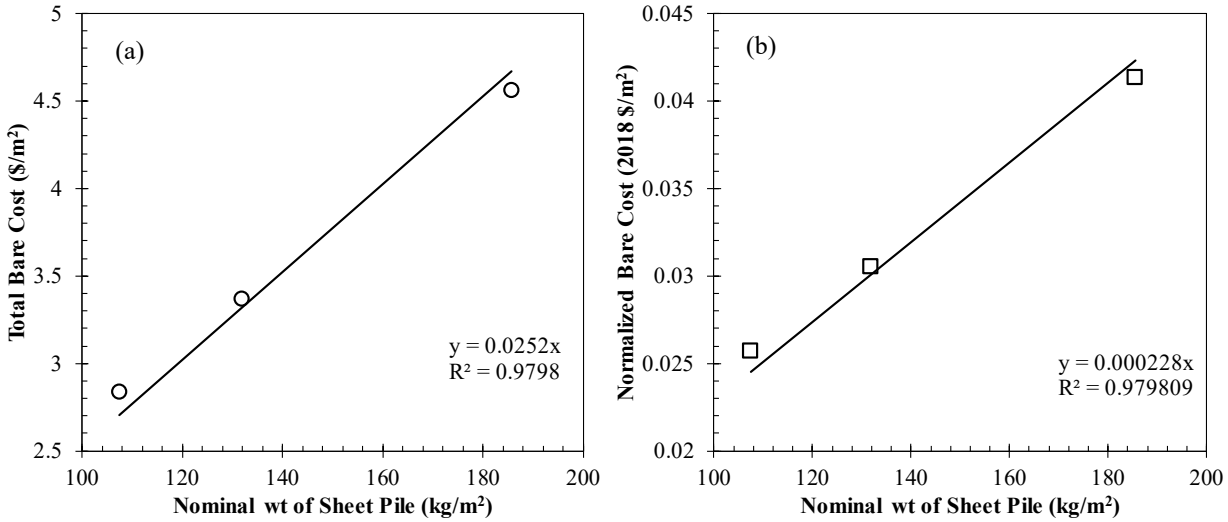

Fig. A-1 General relationship for costs as a function of nominal weight: (a) Total bare cost of sheet pile systems; (b) Bare cost of sheet pile systems normalized with the 2018 deflator index.

The function to extend the total bare cost is given as

$$C_i = 0.0252\omega \tag{A-2}$$

The function to extend the bare cost of sheet pile systems normalized with the 2018 GDP deflator index is given as

$$\frac{C_i}{DI_{Bas}} = 2.28\times10^{-4}\omega \tag{A-3}$$

where ω is the nominal weight of the sheet pile in units of kg/m^2. The base costs adjusted for annual inflation are obtained by multiplying the results of Eq. (A-3) by the GDP deflator index for the current year.

A.2 DEFORMATION-BASED DESIGN WITH COST CONSIDERATIONS

The proposed design approach utilizes a deformation-based methodology that considers system costs. Fig. A-2 illustrates the proposed design methodology for deep excavations. The proposed approach considers excavation-related damage to adjacent infrastructure resulting from induced building distortions. Damage in this context is defined as cracking in the infill walls of the adjacent buildings. The building distortions are the results of ground distortions, which result from ground movements.

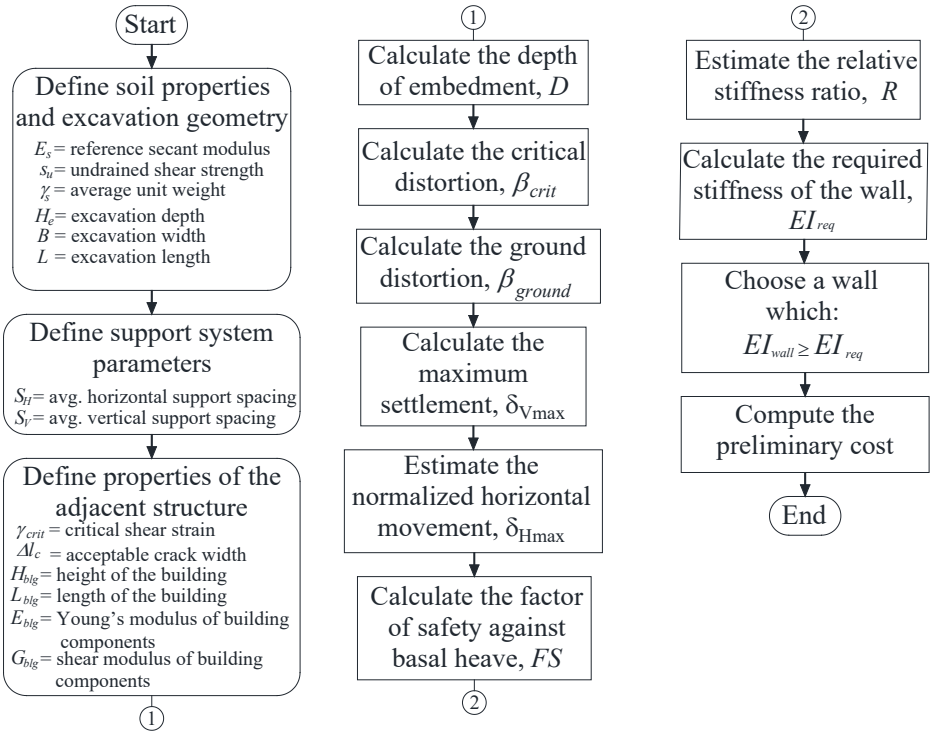

Fig. A-2 Deformation-based design approach that considers system costs

The induced settlement profile adjacent to the excavation is estimated based on the empirical profiles. The excavation support system and the maximum lateral displacement are related through the System Stiffness Ratio, R , developed by Bryson and Zapata-Medina (2012). The proposed methodology in this subsection allows the designer to estimate a bare cost of the support system based on a tolerable crack width in an adjacent infrastructure. Aspects related with the calculation of the bare costs are discussed in subsequent sections herein.

A.3 DAMAGE TO ADJACENT INFRASTRUCTURE

Several quantification criteria have been proposed to evaluate the effects of excavation on adjacent buildings (Burland et al. 1977; Boone et al. 1999; Son and Cording 2005; Halim and Wong 2012). Damage classification is determined based on specific variables, such as maximum crack width, shear and bending strains, principal strains and building tilt. For this study, the maximum crack width was selected as the variable to

characterize the damage to infill walls. Kotheimer and Bryson (2009) presented a normalized crack width approximation for infill walls,

$$\frac{\Delta l_c}{L_{\text{infill}}} = \eta\left(\beta_{meas} - \beta_{crit}\right)\frac{H_{\text{infill}}}{\sqrt{{H_{\text{infill}}}^2 + {L_{\text{infill}}}^2}} \tag{A-4}$$

where Δl_d = estimated crack width ; β_{meas} = measured or anticipated ground distortion; β_{crit} = critical distortion of the infill wall; η = flexibility factor; H_{infill} = height of the infill wall and L_{infill} = length of the infill wall. β_{meas} is the differential settlement of two points of divided by the distance between the two points. The points typically correspond to the foundation locations of the adjacent structure.

In this approach, the crack width is proportional to a flexibility factor. This factor accounts for the condition of the infill wall section. It ranges from 0.5 for a solid wall to 1.0 for a highly punctured wall. In cases where the infill wall is surrounded by a concrete frame (i.e., rigid connection), the calculation of the normalized crack width is based on a length corresponding to half of the infill wall length.

The critical distortion for each infill wall of a multistory building is computed based on the laminate beam approach suggested by Finno et al. (2005) as,

$$\beta_{crit_i} = \left(\frac{{L_{\text{infill}}}^2\left(GA_v\right)_i}{8EI} + \frac{\left(GA_v\right)_i}{\overline{GA_v}}\right)\gamma_{crit_i} \tag{A-5}$$

where $\overline{GA_v}$ = equivalent shear stiffness of the structure; $\left(GA_v\right)_i$ = shear stiffness of the each infill wall; EI =, bending stiffness of the structure; γ_{crit_i} = critical shear strain of the wall material of each floor. See Finno et al. (2005) for more details about the laminate beam.

A.4 INDUCED VERTICAL MOVEMENTS

In this study, damage in adjacent infrastructure was determined by the induced settlement profile. Several methods have been suggested to estimate settlement distribution behind an excavation support wall (Clough 1990; Hsieh and Ou 1998; Kung et al. 2007). These methods considered the characteristics of the excavation and the excavated soil to

evaluate the final induced movements. However, Finno et al. (2002) suggested that for the assumption of undrained deformation (i.e. no volume change) in excavated clay layers, the settlement profile can be estimated from the lateral movement of the wall. Bryson et al. (2018) presented a simplified approach to estimate the lateral wall movements in clayey deposits based on the undrained shear strength (Stiff Clay, $s_u > 50\ kPa$; Medium Clay, $25\ kPa \le s_u \le 50\ kPa$; and Soft Clay, $s_u < 25\ kPa$). Using this assumption, the modified settlement profiles for the different clays are shown in Fig. A-3. In this figure, the distance from the excavation was normalized with respect to the height of the wall.

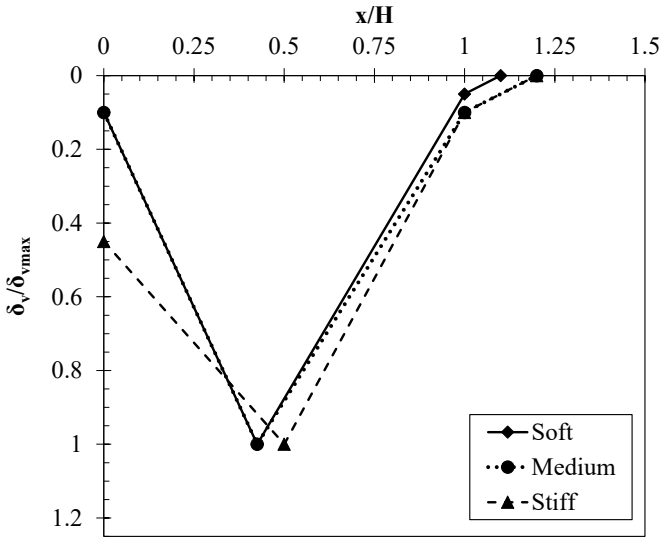

Fig. A-3 Normalized induced settlement distribution.

A.5 LATERAL WALL MOVEMENTS

For this study, the maximum lateral movement of the wall was estimated based on the Relative Stiffness Ratio, R, presented by Bryson and Zapata-Medina (2012) as

$$R = \frac{E_s}{E} \cdot \frac{s_h \cdot s_v \cdot H}{I} \cdot \frac{\gamma_s H_e}{s_u} \tag{A-6}$$

where E_s = elastic modulus of the soil; E = elastic modulus of the wall ; s_h = average horizontal support spacing; s_v = average vertical support spacing; I = moment of inertia per unit length of the wall; H_e = excavation depth; γ_s = average unit weight of the

soil; H = height of the wall; s_u = undrained shear strength of the soil at the bottom of the excavation. According to Bryson and Zapata-Medina (2012) the maximum lateral movement is related to R as

$$\frac{\delta_{H(\max)}}{H}(\%) = 0.275 \times FS^{-0.9322} R^{(0.2585-0.0351 \times FS)} \tag{A-7}$$

where FS = factor of safety against basal heave. Maximum ground settlement can be related to the maximum lateral wall movement using the approximate relationship

$$\frac{\delta_{H(\max)}}{H} = 0.9221 \left(\frac{\delta_{V(\max)}}{H} \right)^{0.7696} \tag{A-8}$$

A.6 METHODOLOGY APPLICATION

A hypothetical excavation is used to illustrate the methodology. The methodology presented in Fig. A-2 was applied to an adjacent structure corresponding to one-story building. Several possible crack widths were pre-defined, and the corresponding preliminary cost associated with the excavation support system was calculated. Fig. A-4 presents the excavation and soil properties, as well as the properties of the building section.

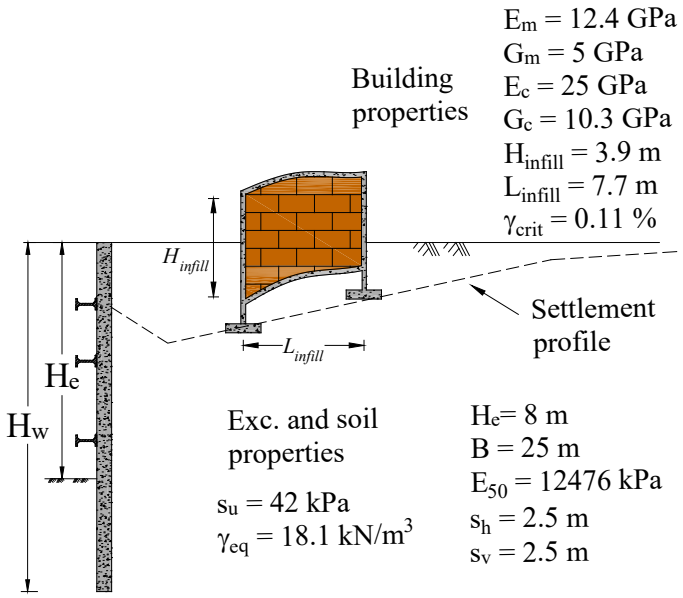

Fig. A-4 Excavation and adjacent building properties for the application of the methodology

Using the laminate beam approximation (Eq. A-5) for a single infill wall with no openings bounded by a strip foundation and a beam, the critical distortion was estimated

as $\beta_{crit} = 0.00161$. The ground distortions were calculated by inputting the pre-defined crack widths into Eq. (A-4). For the calculation, η was assumed as 1.0. The properties of the wall were taken from Fig. A-4. The building was assumed to be located in the sagging (or trough) portion of the settlement profile, at a distance greater than the distance to the maximum induced settlement. The maximum settlement that represents the calculated distortion is given as,

$$\delta_{V\max} = \beta_{ground}\left(\frac{0.575H}{0.9}\right) \tag{A-9}$$

Based on the calculated maximum settlements, the normalized horizontal displacements were calculated for each crack width from Eq. (A-8). Then, from Eq. (A-7) the Relative Stiffness Ratio corresponding to these displacements was computed. The required bending stiffness of the support system was determined from Eq. (A-6), assuming a sheet pile wall with a modulus of elasticity $E = 200GPa$. The required wall moment of inertia was subsequently determined for each crack width. Table A-2 summarizes the results of the calculation process. Because only the damage characteristics of the adjacent structure were modified and not the excavation, all the calculations presented on this table correspond to a single factor of safety against basal heave of 1.7.

Table A-2 Required moment of inertia for each assumed crack width

Δl_c (mm)	$\Delta l_c / L'$	β_{ground}	$\delta_{v(\max)}$ (mm)	δ_{h_norm}	R_{req}	EI_{req} (MN*m^2/m)	I_{req} (cm^4/m)
2	0.0006	0.00234	15.0	0.214	3.40	790.2	395109
3	0.0008	0.00271	17.3	0.239	5.97	450.3	225125
5	0.0013	0.00344	22.0	0.287	15.08	178.2	89112
7	0.0018	0.00417	26.7	0.334	31.84	84.4	42212
9	0.0023	0.00491	31.4	0.378	59.55	45.1	22570
10	0.0026	0.00527	33.7	0.399	78.70	34.2	17080

$L' = L_{\text{infill}}/2$

Fig. A-5 shows the variation of the moment of inertia as a function of the crack width. As shown, the crack widths in the adjacent infrastructure significantly increase with increasing flexibility of the support wall (characterized by a decreasing moment of inertia). Also, the figure illustrates that the relationship between support system stiffness and the induced damages is highly non-linear. Burland et al. (1977) stated that crack widths less

than 5 mm were categorized as slight damage to infill walls. The implication of Fig. A-4 is that an excavation support system with a flexural rigidity greater than around $150 \cdot 10^3 cm^4/m$ would not result in any relevant gain in performance for the hypothetical excavation. It is understood at this point that a different curve will be obtained for a different excavation or adjacent building characteristics.

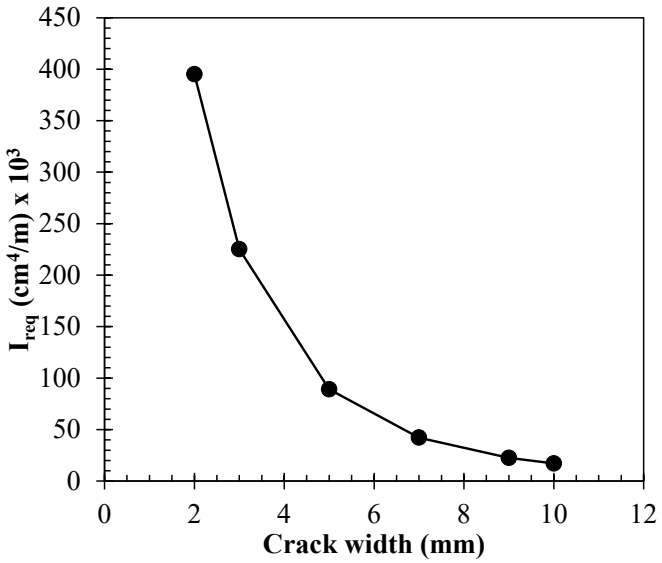

Fig. A-5 Variation of the required moment of inertia as a function of the infill crack width

A simple relationship between the required moment of inertia and the nominal weight of the sheet pile was calculated using appropriate sheet pile sections chosen from the Nucor-Skyline (2019) Product manual. Estimated anticipated crack widths for the hypothetical excavation were calculated by going in the reversed order of the steps used to develop Fig. A-5.Table A-3 summarizes the results of this calculation. Costs for the AZ sheet pile sections were calculated using the Eq. (A-2) for the bare cost and Eq. (A-3) for the normalized bare costs.

Table A-3 Selected sheet pile wall sections for each crack width and their associated normalized bare cost.

Section**	I (cm^4/m)	Nominal Wt (kg/m^2)	Bare Costs ($/$m^2$)	Normalized Bare Cost (2018) ($/$m^2$)	Crack width (mm)
PAZ48/NZ19	425697	245	6.17	0.0558	1.88
PAZ42/NZ19	252623	204	5.14	0.0465	2.70
AZ 38-770N	94840	181	4.55	0.0412	4.89
AZ 20 800	45050	111	2.79	0.0252	6.80
AZ 14-770	23300	103	2.60	0.0235	8.98
AZ 12-770	21430	94	2.38	0.0215	9.25

**Nucor-Skyline (2019)

The variation of the normalized bare cost with the moment of inertia and the variation of the normalized bare cost with the tolerable crack width are shown in Fig. A-6. For performance-based designs, the designer must choose a support system design that prevents damage to the adjacent infrastructure and must be cost effective. Although Fig. A-5 represents a specific excavation with limited support system options, it quantitatively shows the prospect of achieving both the damage prevention and cost effectiveness objectives in a single design process.

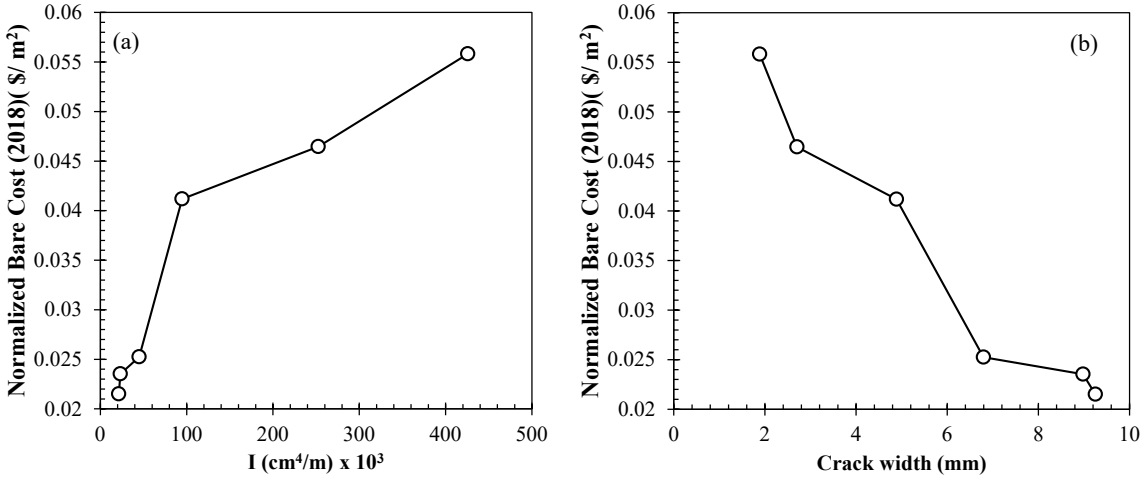

Fig. A-6 Variation of the normalized bare cost as a function of: (a) moment of inertia; (b) crack width.

A.7 CONCLUSIONS

The main objective of this study was to propose a preliminary cost-based approach for the design of the excavation support systems. This approach starts with tolerable damage represented as crack width; this crack width is assumed to develop only in infill walls. The previously determined crack width was related to the ground distortions based on simplified assumptions of soil-structure interaction. The excavation induced movements were related to the support system characteristics by using System Stiffness Ratio, R . After the required section of the wall was determined, the associated cost was computed with the simplified relationship presented.

In the presented approach, the required stiffness of the retaining wall is determined based on tolerable damage, and without the need for iterations in the process. It is advisable to mention that the design procedure proposed in this study applies to brace excavations in

reasonably homogeneous clay deposits and nearby structures on shallow foundations. Also, it does not considered aspects as dewatering and long-term behavior of the excavated soil.

APPENDIX B

Simplified Strut-Based Model for Cracking of Infill Walls Due to Excavation-Induced Distortions

B.1 INTRODUCTION

In the context of deep excavation in modern cities, characterized by densely populated areas, the estimation of damage to adjacent infrastructure due to deep cuts is paramount. The damages induced by a deep excavation are directly related to cost overages associated with the project. Monetary losses associated with distress in existing facilities not only affect the direct agents involved in the excavation activities (i.e., owners, contractors, adjacent infrastructure owners) but also the community in general. Also, utilities are often encountered during the excavation process, and the efforts required to relocate and protect these affected utilities increase project time and construction costs. For these reasons and additional aspects (e.g., potential lawsuits by the adjacent infrastructure owners), the estimation of damage due to excavation-induced movements is a topic of significant interest for the geo-construction community.

The common practice for estimating excavation-related damage is to assume greenfield movements are applied directly to the structure adjacent to the excavation, without any soil-structure interaction analysis. The adjacent structure has been traditionally idealized by models ranging from mechanics of materials approximations (Son and Cording 2005; Kotheimer and Bryson 2009) to deep or laminate beams (Boscardin and Cording 1989; Boone et al. 1999; Finno et al, 2005). Theoretically, these approximation models may apply to a multitude of adjacent buildings by varying the building stiffness in the selected model to account for the type of structure. However, for frame buildings this approach may not be appropriate given the interaction between the frames and the infill walls (Mainstone 1974). A more appropriate approach is to model the infill wall as one or several struts compressed during the movement of the bounding frame (El-Dakhakhni et al. 2003).

Although a very refined numerical model that accounts for complete soil-structure interaction can be used to determine a reasonable approximation of the damage caused by excavation, this type of estimation is restricted to the specifics of the modeling process.

These specifics include the soil model, building representation, and excavation sequence, among others. Also, when preliminary damage costs are required, a high-fidelity model of the excavation process can be time-consuming and impractical. These issues make the approximation models attractive to perform a preliminary estimate of the possible excavation-induced damage. In this study, a simplified strut model proposed by Di Trapani et al. (2018) for modeling infill walls was applied to determine the likelihood of cracking in infill walls when subject to ground distortions.

The original purpose of the model proposed by Di Trapani et al. (2018) was for infill walls subjected to horizontal displacements. However, other researchers (Qian and Li 2017) have also used the apparent equivalence between the infill walls and compressive struts for frames subjected to vertical displacement. A database of published pushdown tests in infill walls was collected; the computed cracking distortion using the method of Di Trapani et al. (2018) was compared with the measured distortions. A brief discussion of the results is presented at the end of the paper.

B.2 SIMPLIFIED STRUT MODEL FOR INFILL WALL AND THE BOUNDING FRAME

Fig 1. Shows a part of a frame structure subjected to the ground distortions caused by excavation, and the equivalent strut assumed for the infill walls. Although urban excavations also induced horizontal movements, it is assumed that the foundation of the structure is rigid rigidly connected to limit the damage caused by these types of movements. Therefore, only building distortions caused by the induced settlement profile are considered. Implicit in Fig. B-1 is that the strut model can be used to model the infill walls on any floor of the structure given the characteristic of the bounding frame surrounding the wall.

Several struts' models are present in literature. One-strut models (Mainstone 1974; Saneinejad and Hobbs 1995) and three-strut models (El-Dakhakhni et al. 2003) are the most common. However, models considering more struts to represent the infill wall are also available, especially to model infills with openings due to doors or windows (Asteris et al. 2016). These struts models have been implemented largely to estimate the ultimate capacity of a frame considering the influence of the non-structural infill wall. Nonetheless, the focus of this study is the cosmetic damage caused by excavation, and only

displacements that cause initial cracking of the wall are of interest. For this study, only full infill walls are considered.

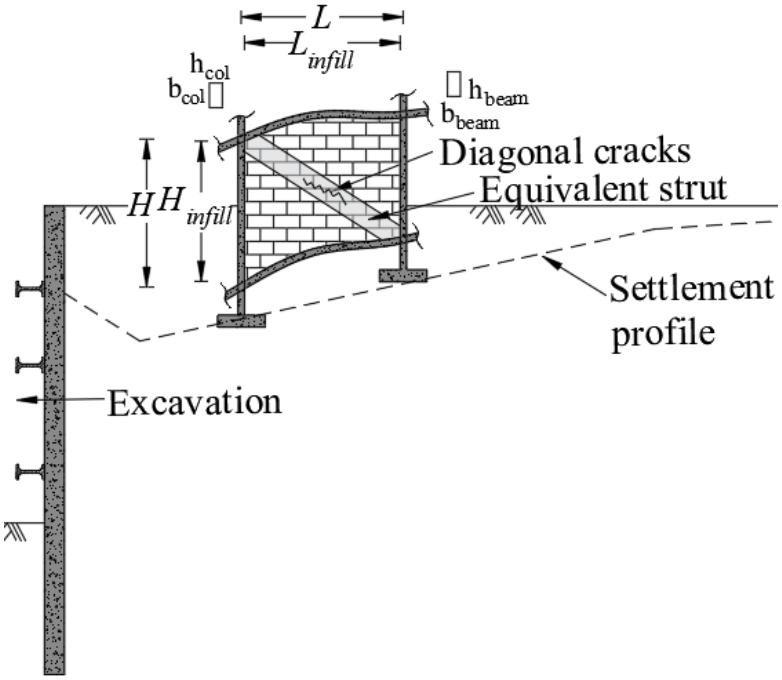

Fig. B-1 Framed building, induced settlement, and equivalent strut

This study intents to estimate the ground distortions that can cause cracking. Therefore, a load-displacement curve of the equivalent strut is necessary to determine the threshold of damage. Di Trapani et al. (2018) presented a stress-strain relationship for modeling the response of the equivalent struts. This relationship was based on the failure modes of cracking or corner crushing of infill walls. This stress-strain curve is shown in Fig. B-2. The curve is defined by four parameters given as peak stress f_{md0}, peak strain ε_{md0}, ultimate stress f_{mdu}, and ultimate strain ε_{mdu}. These four empirical parameters were determined through collected experimental data sets complemented with results from finite element simulations. These parameters were related to the geometrical and mechanical characteristics of an infilled frame using numerical correlations. Different types of masonry units were collected for the correlations as solid and hollow clay units as well as brick units.

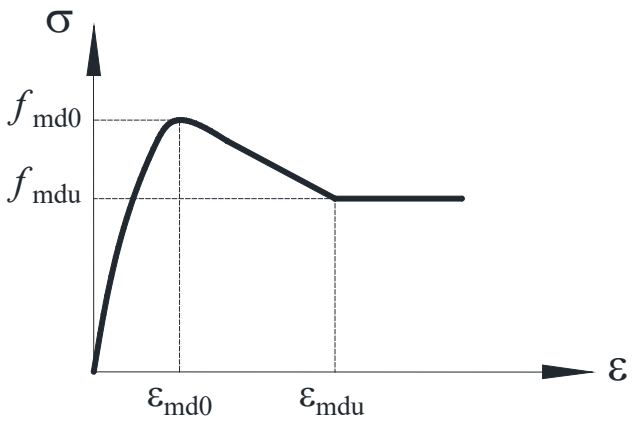

Fig. B-2 Stress-strain curve for the equivalent strut after Di Trapani et al. (2018)

In the context of this study, only the peak strain ε_{md0} is of interest. Up to this point, the behavior of the strut is assumed elastic, it is recognized that ε_{md0} does not represent the actual strain observed along the diagonal of the infill wall but merely an empirical parameter to idealize the infill behavior. Therefore, the accuracy of this parameter to represent the development of tension cracks in the loaded diagonal needs further validation. According to Di Trapani et al. (2018) normalized peak strain of the equivalent strut is given by,

$$\frac{\varepsilon_{md0}}{\varepsilon_{m0}} = 3.024\gamma^{0.347} \tag{B-1}$$

where ε_{m0} is the peak masonry strain (assumed as 0.0015) and γ is an empirical parameter. The γ parameter is calculated as,

$$\gamma = \left(\frac{{f_{mdu}}^2}{f_{md0}}\right)\left(\frac{E_c}{\tilde{E}_m^{1.5}}\right) \tag{B-2}$$

where E_c is the Young modulus of the concrete and $\tilde{E}_m$ is and equivalent Young modulus of the masonry. The $\tilde{E}_m$ parameter is calculated as,

$$\tilde{E}_m = \sqrt{E_{m1} \cdot E_{m2}} \tag{B-3}$$

where E_{m1} and E_{m2} are the Young moduli of masonry along the horizontal and vertical direction, respectively. The interested reader may refer to Di Trapani et al. (2018)

for the further details about the process to obtained f_{md0} and f_{mdu}, in this paper the calculated values are presented with a collected database.

B.3 INDUCED DISTORTION BY THE ADJACENT EXCAVATION

Fig. B-3 presents the assumed deformation of a section of a framed building (i.e. dashed lines) when subjected to an induced differential settlement δ. Considering the shown deformation, the ground distortion β can be expressed as

$$\beta = \frac{\delta}{L} = \frac{\varepsilon_d l_d}{L \sin\alpha} \tag{B-4}$$

where ε_d is the strain along the diagonal of the infill wall; l_d is the distance between the nodes of the frame. Thus, to estimate the cracking distortion caused by induced movements (i.e., distortion at which the *first crack* occurs), the strain ε_d is substituted by the peak strain of the strut ε_{md0} as

$$\beta = \frac{l_d \varepsilon_{m0} \cdot 3.204\gamma^{0.347}}{L \sin\alpha} \tag{B-5}$$

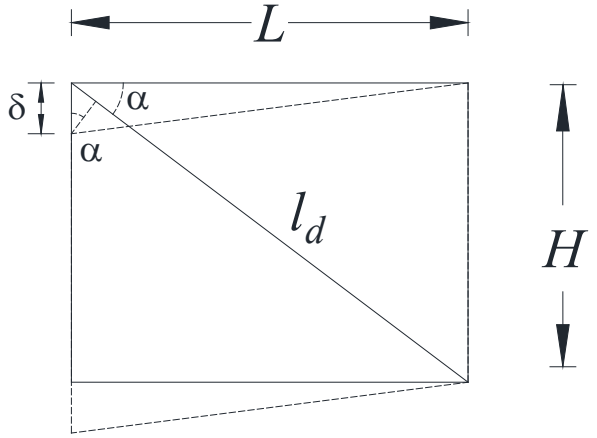

Fig. B-3 Assumed deformation of the infill wall and the frame

B.4 DATABASE AND MODEL VALIDATION

The presented approximation to calculate the ground distortion that initiates cracking was compared with published pushdown tests conducted in infilled frames. The main information of the collected database, including the infill characteristics, are shown

in Table B-1 and Table B-2. The deformation of the specimens (i.e., frames) during the pushdown tests is analogous to the deformation mechanism assumed during a deep excavation (Fig. B-1). It should be noted that the collected pushdown tests for the development of the database were reported as being conducted using scale wall specimens. Therefore, further verification is required using full-size pushdown tests.

Table B-1 Collected database of pushdown tests in infill walls and frames

Reference	Specimen ID	t (mm)	H_{infill} (m)	H (m)	L_{infill} (m)	L (m)	b_{col} (mm)	h_{col} (mm)	b_b (mm)	h_b (mm)
Qian and Li (2017)	WNS[(a)]	90	0.685	0.825	1.65	1.8	150	150	90	140
	WSS	90	0.685	0.825	1.65	1.8	150	150	90	140
	WNL	90	0.685	0.825	2.25	2.4	150	150	90	140
Li et al. (2019)	1	63.5	0.95	1.1	1.5	1.7	200	200	100	150
	2	63.5	0.95	1.1	1.5	1.7	200	200	100	150
Brodsky (2018)	1	100	1.4	1.6	2.045	2.145	200	100	100	200
	2	100	1.4	1.6	2.045	2.245	100	200	100	200
	3	100	1.4	1.6	2.045	2.245	100	200	100	200
	4	100	1.4	1.6	2.045	2.245	100	200	100	200
	5	100	1.4	1.6	2.045	2.245	100	200	100	200
	6	100	1.4	1.6	2.045	2.245	100	200	100	200
	7	100	1.4	1.6	2.045	2.145	200	100	100	200

[(a)]WNS= No seismic designed infilled frame with short span; WSS=Seismic designed infilled frame with short span; WNL= No seismic designed infilled frame with long span. *Refer to Fig. B-1 for definition of dimension variables

Table B-2 Additional parameters of the collected database shown in Table B-1

Reference	Specimen ID	f'_m (MPa)	$\tilde{E}_m$ [(a)] (MPa)	f_c' (MPa)	E_c [(b)] (MPa)	f_{md0} (MPa)	f_{mdu} (MPa)
Qian and Li (2017)	WNS	10.5	7350	33.8	27325	2.72	1.28
	WSS	10.5	7350	34.3	27526	2.71	1.28
	WNL	10.5	7350	33.3	27122	2.31	1.17
Li et al. (2019)	1	12.8	8960	41.3	30205	3.68	1.05
	2	12.8	8960	31.8	26504	3.73	1.05
Brodsky (2018)	1	9.44	6608	27.4	24602	2.74	1.02
	2	9.44	6608	28.3	25003	2.75	1.00
	3	9.44	6608	28.3	25003	2.75	1.00
	4	1.77	1239	27.0	24422	1.02	0.32
	5	1.77	1239	26.8	24331	1.02	0.32
	6	1.77	1239	28.2	24959	1.02	0.32

7	9.44	6608	26.6	24240	2.75	1.02

(a) Assumed as $\tilde{E}_m = 700 f'_m$.

(b) Assumed as $E_c = 4700 f_c'$.

Table B-3 presents the measured distortions and the calculated using the presented approach (β_{cal}). As can be seen in all the cases, the measured distortion at which cracking was observed is less than the calculated. Therefore, the strut model overestimates the critical distortion in the infill walls. This overestimation of the critical distortion can be a result of the assumed parameters of the infill wall, when not given, and the strut simplification reflected on the empirical equations proposed by Di Trapani et al. (2018).

A Monte Carlo (MC) simulation was conducted to study the variation on the predicted critical distortion when a minor modification was applied to the presented approach. In this case, the peak strain in the strut model was reduced by a factor of 1/3 based on the overestimation seen for the previous results. In the MC simulation, the compressive strengths of the masonry and the concrete were the only random variables considered; the geometric characteristics of the frames were assumed constants. The reported strength values from the databased were considered as the mean values of strength. The standard deviation the masonry was taken as 0.48 MPa (Kaushik et al. 2007); and for the concrete was 0.127 times its compressive strength (Gao et al. 2018). A total of 1000 random values were generated for the estimation of the critical distortion considering that the compressive strength of the masonry and the concrete are normally distributed (Xiao et al. 2005).

Table B-3 Measured and calculated distortion on infill walls

Reference	Specimen ID	δ @ 1st crack (mm)	β_{mea} (10^{-3})	β_{cal} (10^{-3})	$\mu_\beta^{(b)}$ (10^{-3})	$\sigma_\beta^{(b)}$ (10^{-3})
Qian and Li (2017)	WNS	2.00	1.11	3.31	1.10	0.03
	WSS	1.80	1.00	3.32	1.10	0.03
	WNL	2.40	1.00	4.27	1.43	0.04
Li et al. (2019)	1	1.0	0.59	1.83	0.61	0.02
	2	1.0	0.59	1.74	0.58	0.02
Brodsky (2018)	1	1.40	0.65	2.27	0.76	0.02
	2	2.00[(a)]	0.89	2.15	0.72	0.02
	3	3.30	1.47	2.15	0.72	0.02
	4	4.50	2.00	3.29	1.12	0.12

5	0.90	0.40	3.29	1.11	0.12
6	2.00[(a)]	0.89	3.32	1.12	0.11
7	1.5[(a)]	0.70	2.25	0.75	0.02

[(a)]Estimated [(b)] $1/3\varepsilon_{md0}$

Fig. B-4 shows the relative frequency and the cumulative frequency for the first crack obtained from the Monte Carlo analysis. It appears that the critical distortion, when considered as random variable, follows a normal probability distribution. Further analysis on this aspect were not considered because the main used of the MC analysis in this paper was to ascertain if the presented approach could give likely values of critical distortions.

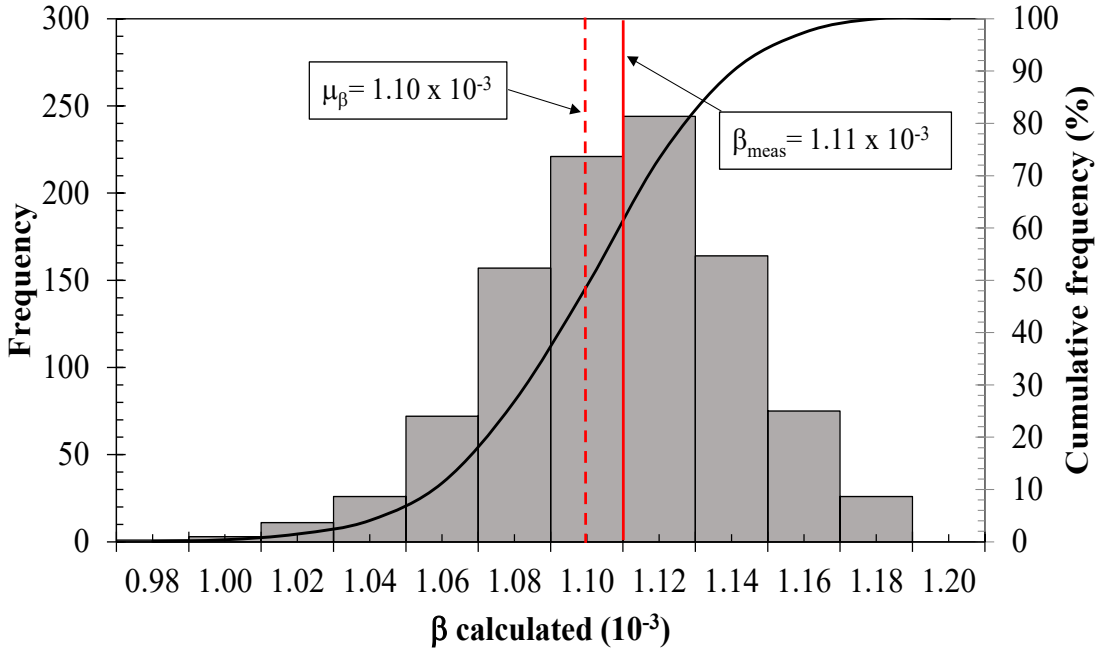

Fig. B-4 Monte Carlo simulation for the first test

As seen from this figure, the histogram reflects that the expected value (i.e., calculated mean) of the cracking distortion is smaller than the measured from the test, which is represented by the red line. As seen from the figure, for this test, the measured distortion at first cracking appears between the values estimated in the MC simulation. Although, the measured distortion is not the expected value from the calculation (i.e., mean cracking distortion). This result is considered satisfactory, it tends to be on the safest side of damage prediction. Following the same approach for the other tests on the database. Table B-3 presents the estimated mean and standard deviation for each test of the database.

Fig. B-5 shows the measured versus the mean calculated cracking distortion for the tests from the database. It is observed that lines corresponding to $\beta_{meas} = 0.6 - 1.5\mu_{\beta cal}$ bound most of the data where β_{meas} the measured critical distortion; and $\mu_{\beta cal}$ is the expected value from the MC analysis. This figure also shows the limit suggested by Bjerrum (1963) for cracking, $\beta_{crack} = 1/300$, it appears that the critical distortion is less than this limit. However, because this limit was suggested base on full infill walls and the results of this analysis were based on scaled models, further validation of this conclusion is warranted through push-down testing in full infill walls.

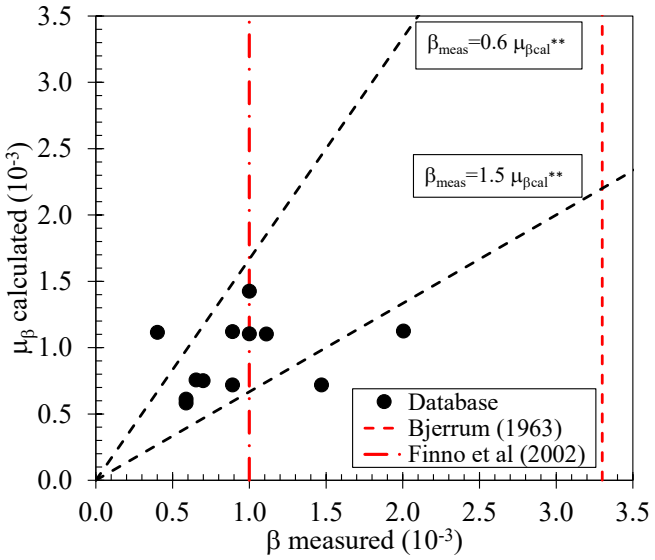

Fig. B-5 Measured distortion versus mean distortion from MC simulation

Analytical variation of the critical distortion can be computed based on Eq. (B-5) for several infill properties and geometries. Fig. B-6 presents the variation of β for typical concrete compressive strength between 21-42 MPa, masonry compressive strength between 5-15 MPa and for three different aspect ratio of infill walls. Results are presents in terms of the parameter γ which this describes the relation between the mechanical properties of the concrete and the masonry as well as the effect of empirical factors f_{md0} and f_{mdu} used in the calculation of β. As expected, the critical distortion increases as a function of γ for the same infill geometry. In addition, with the increase of the length of the infill wall, the values of β also increases based on the presented approach.

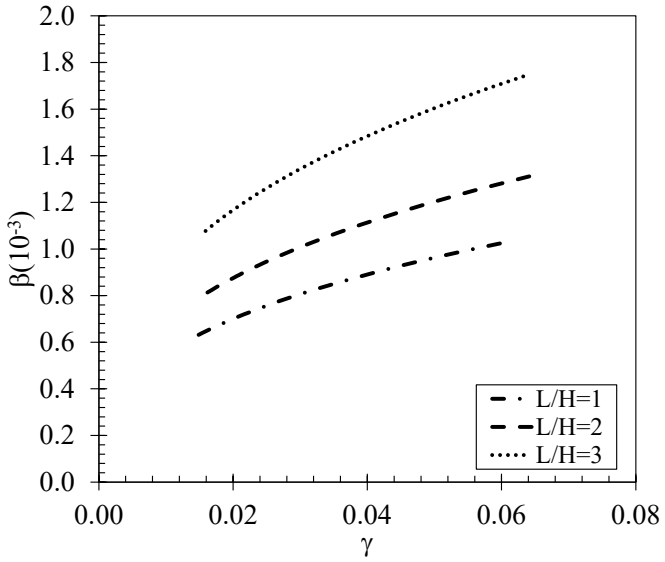

Fig. B-6 Variation of β_{lc} with the parameter γ

B.5 CONCLUSIONS

This paper presents the evaluation of a strut model for computing the cracking distortion in an infill wall. The proposed approach was found conservative in light of another cracking limit. Although the original development of the strut model was based on horizontally loaded frames, using a factor of 1/3 for the cracking strain of the masonry gives results that are considered satisfactory as damage approximation. The presented approach was applied on a database of plane frames; the effect of transverse beams and RC slabs on the calculated distortion was not included. In addition, it is recommended the validation of this approach with full size infill walls. The Monte Carlo simulation showed that some measured cracking distortions were within the expected cracking distortions values using the assumed standard deviations of concrete and masonry strength. In most of the cases, the calculated critical distortion was close to the recommended values to prevent any damage of 1/1000 suggested by Finno et al. (2002).

APPENDIX C

Example Deformation-Based Excavation Support System Design Method Selected Material Properties for Testing

Input parameters of the soil

$s_u := 42\ kPa \quad \gamma := 18.1\ \frac{kN}{m^3} \quad H_e := 10\ m \quad B := 25\ m$

$E_s := 12476\ kPa = 12.476\ MPa$

Input parameters of the infill wall

$E_m := 12.4\ GPa \quad G_m := 4.96\ GPa \quad \gamma_{crit} := 0.11\%$

$E_c := 24.8\ GPa \quad G_c := 10.3\ GPa$

$H_w := 3.86\ m \quad L_w := 2 \cdot H_w = 7.72\ m$

Design process

Calculation of the depth of embedment

$N_s := \frac{\gamma \cdot H_e}{s_u} = 4.31$

$\frac{B}{H_e} = 2.5$

$D := min\left(H_e \cdot 55.825 \cdot e^{2.0104 \cdot \ln\left(\frac{B}{H_e}\right) - \frac{1}{N_s} \cdot 4.35 \cdot \ln\left(\frac{B}{H_e}\right) - \frac{1}{N_s} 22.949}, H_e\right) = 6.8\ m$

$H_{wall} := D + H_e = 16.8\ m$

Calculation of the critical distortion

y_i (m)	h_i (m)
0	0
3.86	3.86

$H := h_{i_{length(h_i)-1}} = 3.86\ m$

$A_{1i_0} := 0.22\ m^2$

$A_{1i_1} := 0.22\ m^2$

$A_{1i} = \begin{bmatrix} 0.22 \\ 0.22 \end{bmatrix} m^2$

Fig. C-1 Input soil and excavation properties. Mathcad calculation sample

$$\sum A_{1i} = 0.44\ m^2$$

$$\lambda H := \frac{A_{1i} \cdot h_i}{\sum A_{1i}} = 1.93\ m$$

$$I := A_{1i} \cdot \left(h_i - \lambda H\right)^2 = 1.6\ m^4$$

$$\lambda := \frac{\lambda H}{H} = 0.5$$

$$ii := 1 \qquad ratio1f_1 := \operatorname{abs}\left(\frac{y_{i_{ii}}}{I} \cdot \sum_{j=ii}^{\operatorname{length}(h_i)-1} A_{1i_j} \cdot \left(\lambda H - h_{i_j}\right)\right) = 1$$

$$ratio1f := \text{for } j \in 1..\operatorname{length}(h_i) - 1$$
$$\quad ii \leftarrow j$$
$$\quad ratio_j \leftarrow \operatorname{abs}\left(\frac{y_{i_{ii}}}{I} \cdot \sum_{j=ii}^{\operatorname{length}(h_i)-1} A_{1i_j} \cdot \left(\lambda H - h_{i_j}\right)\right)$$
$$\quad ratio$$

$$ratio1f = \begin{bmatrix} 0 \\ 1 \end{bmatrix} \qquad \sum ratio1f = 1$$

Shear Stiffness of the wall

$$GA1f_{v_0} := 0\ kN$$

$$GA1f_{v_1} := G_m \cdot 3.86\ m \cdot 12\ in = 5.84\ GN$$

Equivalent Shear Stiffness

a=percentage opening in a wall

$$a1f_0 := 0 \qquad a1f_1 := 0$$

$$GA1f'_v := \overrightarrow{GA1f_v \cdot \left(1 - a1f\right)} = \begin{bmatrix} 0 \\ 5.8 \end{bmatrix} GN$$

$$\frac{y_{i_1}}{H} \cdot ratio1f_1 \cdot \frac{1}{GA1f'_{v_1}} = 0.171\ \frac{1}{GN}$$

Fig. C-2 Laminated beam approach and equivalent shear stiffness. Mathcad calculation sample

$$\sum_{ii=1}^{\text{length}(h_i)-1} \frac{y_{i_{ii}}}{H} \cdot ratio1f_{ii} \cdot \frac{1}{GA1f'_{v_{ii}}} = 0.171 \ \frac{1}{GN}$$

$$GA_{eqv} := \frac{1}{\sum_{ii=1}^{\text{length}(h_i)-1} \frac{y_{i_{ii}}}{H} \cdot ratio1f_{ii} \cdot \frac{1}{GA1f'_{v_{ii}}}} = 5.84 \ GN$$

Equivalent bending stiffness

$$EI_{eqv} := E_c \cdot I = 41 \ GN \cdot m^2$$

$$L := \begin{bmatrix} 0 \ m \\ L_w \end{bmatrix} = \begin{bmatrix} 0 \\ 7.72 \end{bmatrix} m$$

Fixed frame

$$\beta := \text{for } k \in 1..\text{length}(L)-1 \quad \text{for } j \in 1..\text{length}(A_{1i})-1 \quad \beta_{j,k} \leftarrow \left(\frac{\left(\frac{L_k}{2}\right)^2 \cdot GA1f'_{v_j}}{8 \cdot EI_{eqv} \cdot ratio1f_j} + \frac{GA1f'_{v_j}}{ratio1f_j \cdot GA_{eqv}} \right) \cdot (\gamma_{crit}) \quad \beta$$

$$\beta = \begin{bmatrix} 0 & 0 \\ 0 & 0.00139 \end{bmatrix}$$

Critical distortion

$$\beta_{crit} := 0.00139$$

$$\Delta l_c := 4 \ mm$$

$$L' := \frac{L_w}{2} = 3.86 \ m \qquad \text{<---fixed frame}$$

$$\frac{\Delta l_c}{L'} = 0.001$$

$$\eta := 1.0$$

$$\beta_{meas} := \frac{\Delta l_c}{L'} \cdot \frac{1}{\eta} \cdot \frac{\sqrt{L'^2 + H_w^{\ 2}}}{H_w} + \beta_{crit} = 0.00286$$

Fig. C-3 Equivalent bending stiffness and critical distortion. Mathcad calculation sample

Computing the maximum settlement induced that represents the calculated distortion. Based on the trilinear plots

$$\delta_{Vmax} := \beta_{meas} \cdot \frac{0.575 \cdot H_{wall}}{0.9} = 30.648 \ mm$$

The normalized horizontal deformation corresponds to

$$\delta_{Vmax\_norm} := \frac{\delta_{Vmax}}{H_{wall}} \cdot 100 = 0.182$$

$$\delta_{Hmax\_norm} := \left(0.9221 \cdot \left(\delta_{Vmax\_norm}\right)^{0.7696}\right) = 0.249$$

Computing the factor of safety against basal heave based on the modified Terzaghi equation

$$N_c := 5.14 \quad s_u = 42 \ kPa$$

$$FS_{BH} := \frac{N_c \cdot s_u + \sqrt{2} \cdot s_u \cdot \left(\frac{H_{wall}}{B}\right) + 2 \cdot s_u \cdot \left(\frac{D}{B}\right)}{\gamma \cdot H_e} = 1.539$$

Calculate the required relative stiffness ratio

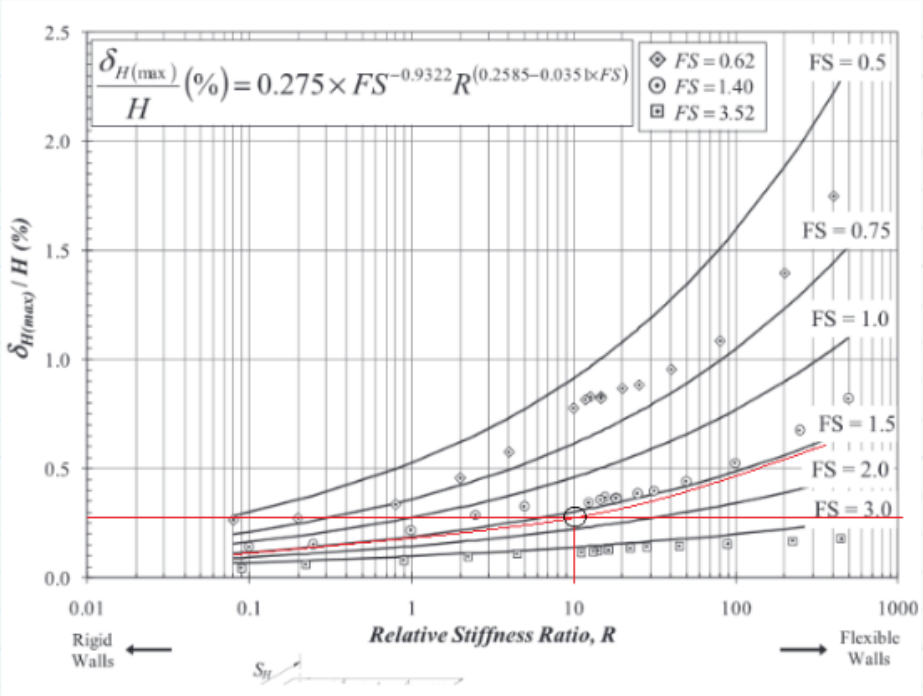

Fig C-4 Normalized settlement and relative stiffness ration (R). Mathcad calculation sample

$R_{req} = 4.395$ $R_{req} := 4.5$

Required bending stiffness of the wall

$s_h := 5\ m$ $s_v := 2.5\ m$

$$EI_{req} := \frac{E_s \cdot s_h \cdot s_v \cdot H_{wall}}{R_{req}} \cdot \frac{\gamma \cdot H_e}{s_u} = 2508977\ \frac{kN \cdot m^2}{m}$$

For a steel wall

Assuming $E_{steel} := 200\ GPa$

Required inertia $$I_{req} := \frac{EI_{req}}{E_{steel}} = 1254488\ \frac{cm^4}{m}$$

Select a section

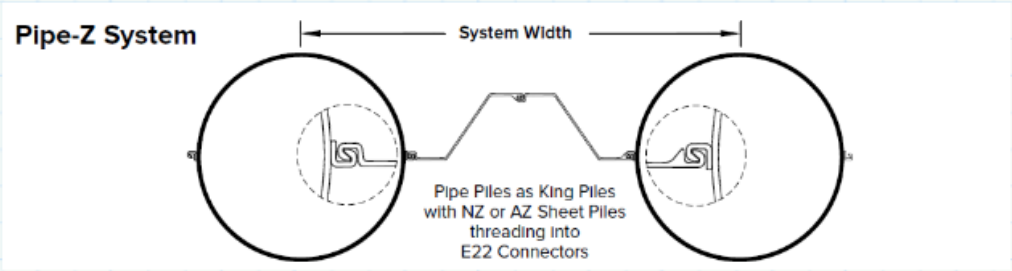

Pipe-Z System Combination Sample	Sheet Pile Section	PROPERTIES OF PIPE PILE			PROPERTIES OF COMBINED WALL							COATING
		Outside Diameter	Wall Thickness	Pipe Weight	System Width	System Inertia	Section Modulus	WEIGHT (Sheet Pile Length/Pipe Length) 100%	80%	60%	Cross Sectional Area	Both Sides of Wall
		in mm	in mm	lb/ft kg/m	in mm	in⁴/ft cm⁴/m	in³/ft cm³/m	lb/ft² kg/m²	lb/ft² kg/m²	lb/ft² kg/m²	in²/ft cm²/m	ft²/ft m²/m
PAZ66/AZ38-700N	AZ 38-700N	66.00 1676.40	1.000 25.4	694.85 1034.08	123.48 3136	10793 1473880	327.1 17584	85.4 417.1	81.8 399.6	78.3 382.1	25.10 531.3	31.72 9.67

$F_y := 415\ MPa$ A 572 Grade 60

$F_b := 0.6 \cdot F_y$ $F_b = 249\ MPa$

Fig. C-5 Required bending stiffness and wall selection. Mathcad calculation sample

$I_{dgn} := 1473880 \ \frac{cm^4}{m}$

$I_{dgn} > I_{req} = 1$

$S_{dgn} := 17584 \ \frac{cm^3}{m}$

Recalculating the Rdgn

$R_{dgn} := \frac{E_s \cdot s_h \cdot s_v \cdot H_{wall}}{E_{steel} \cdot I_{dgn}} \cdot \frac{\gamma \cdot H_e}{s_u} = 3.83016$ $\qquad \frac{\gamma \cdot H_e}{s_u} = 4.31$

Maximum capacity of the wall

$M_{max} := F_b \cdot S_{dgn} = 4378.4 \ \frac{kN \cdot m}{m}$

Average uniform loading assuming simply support

$p := \frac{8 \cdot M_{max}}{s_v^2} = 5604.4 \ kPa$ $\qquad s_v = 2.5 \ m$

Based on the reduction factor ξ, the apparent pressure to design the struts and the wales will be given by

$\xi := 0.047$

$p_{eqv} := p \cdot \xi = 263.4 \ kPa$

This load will be applied to the wales in order to calculate the maximum bending moments in the wale

$M_{wale} := 0.67 \cdot \frac{p_{eqv} \cdot s_h^2}{12} \cdot s_v = 919.2 \ kN \cdot m$ $\qquad$ 0.67 from Load reduction Teng (1962)

$P_{axial} := 0.67 \cdot p_{eqv} \cdot \frac{s_h}{2} \cdot s_v = 247.967 \ kip$

Try W30x191

$F_y := 36 \ ksi$

$A := 56.1 \ in^2$ $\qquad r_x := 12.8 \ in$ $\qquad r_y := 3.46 \ in$ $\qquad S := 600 \ in^3$

Fig. C-6 Equivalent pressure for the struts and wales design. Mathcad calculation sample

$$f_a := \frac{P_{axial}}{A} = 30.475\ MPa$$

$L_x := s_h = 5\ m$ $\qquad$ $L_y := s_h = 5\ m$

$k_x := 1.0$ $\qquad$ $k_y := 1.0$

$$k_x \cdot \frac{L_x}{r_x} = 15.379 \qquad k_y \cdot \frac{L_y}{r_y} = 56.9$$

$$F_a := 0.6 \cdot F_y = 148.927\ MPa$$

$$f_b := \frac{M_{wale}}{S} = 93.5\ MPa$$

Check for compact section

$$\lambda_p := \frac{65}{\sqrt{36}} = 10.833$$

$\lambda_p > 7.04 = 1$ $\qquad$ Good!!

$$F_b := 0.6 \cdot F_y = 148.927\ MPa$$

$c_m := 1.0$ $\qquad$ $E_{steel} = 200\ GPa$

$$F'_e := \frac{12}{23} \cdot \frac{\pi^2 \cdot E_{steel}}{\left(k_x \cdot \frac{L_x}{r_x}\right)^2} = 4354.422\ MPa$$

$$\frac{f_a}{F_a} + \frac{c_m \cdot f_b}{\left(1 - \frac{f_a}{F'_e}\right) F_b} = 0.837$$ $\qquad$ Good

$$\frac{f_a}{0.6 \cdot F_y} + \frac{f_b}{F_b} = 0.832$$ $\qquad$ Good

Fig. C-7 Wale checking. Mathcad calculation sample

APPENDIX D

Stress controlled MATLAB implementation of the Hypoplastic Clay model (Mašín 2005)

```
function [Invariants,e_strain,e_void_] = hypo_stress_controlled(p_init,q_init,dpmax,e0,parms,Test_type)

%% Model parameters
phi         = parms(1);
lambda      = parms(2);
kappa       = parms(3);
Nparam      = parms(4);
rparam      = parms(5);

%%
phic = phi/180*3.14159265358979;% critical state friction angle in radians

% nsteps=5000;
% dp=dpmax/nsteps;% increment in the mean effective stress(fixed increment)

if  Test_type==1
    dp=0.05;
    nsteps=dpmax/dp;
else
    dp=-0.05;
    nsteps=dpmax/dp;
end

%%
e_v=0;
e_s=0;
e_strain=[e_v e_s];% strain invariants
   %% Calculation
   Sigma=[p_init;q_init];
   Invariants=Sigma';
   e_void=e0;
   e_void_(1)=e_void;

   if Test_type==1
       %% Drained loading
       dq=dp*3;
       for jj=1:nsteps

           p=Sigma(1);
           q=Sigma(2);
           eta=q/p;

           tanpsi=sqrt(2)*abs(q)/(3*abs(p));

           if eta==0
               eta=0.0000001;
               cos3theta=(-sqrt(6)*2*eta*eta*eta/243)/((2*eta*eta/27)^1.5);
           else
               cos3theta=(-sqrt(6)*2*eta*eta*eta/243)/((2*eta*eta/27)^1.5);
           end

           F=sqrt((tanpsi*tanpsi/8)+((2-tanpsi*tanpsi)/(2+sqrt(2.)*tanpsi*cos3theta)))-(tanpsi/(2*sqrt(2.)));

           a=sqrt(3.)*(3-sin(phic))/(2*sqrt(2.)*sin(phic));
```

Fig. D-1 Function definition and drained calculation

```
        pcr=exp((Nparam-log(1+e_void))/lambda)/2;
        alpha_power=log((lambda-kappa)*(3+a*a)/((lambda+kappa)*a*sqrt(3.)))/log(2.);

        fd=(p/pcr)^alpha_power;
        fdi=2^alpha_power;
        c1 = (1 + (a*a)/3 - fdi*a/(sqrt(3.)))/(1.5 * rparam);
        c2 = 1. + (1. - c1)*(3. / (a * a));

        fs=(3*p./lambda)/(3 + a*a - a*sqrt(3.)*fdi) ;

        Lmatrix(1,1)=c2*a*a/3+c1;
        Lmatrix(1,2)=c2*eta*a*a/3;
        Lmatrix(2,1)=Lmatrix(1,2);
        Lmatrix(2,2)=c2*eta*eta*a*a/3+9*c1/2;

        L_bar=fs*Lmatrix;

        I1=3*p;
        I2=q*q/3-3*p*p;
        I3=(-2*q*q*q/27+(p*q*q/3-p*p*p))*-1;

        Yield=(sqrt(3.)*a/(3+a*a)-1)*((I1*I2+9*I3)*(1-sin(phic)*sin(phic)))/(8*I3*sin(phic)*sin(phic))+sqrt(3.)*a/(3+a*a);
        if Yield>= 0.999
            return
        end
    N11aux1=-(Yield*a*sqrt(3)*(((4*c2*eta*eta+9*c2)*F*F-2*c1*eta*eta)*a*a+27*c1*F*F));
    N11aux2=F*((2*eta*eta+9)*a*a+27*F*F)*sqrt((a*a*((4*eta*eta*eta*eta+18*eta*eta)*a*a*a*a+...
        108*eta*eta*F*F*a*a+(648*eta*eta+729)*F*F*F*F)/(F*F*((2*eta*eta+9)*a*a+27*F*F)^2)));
    N_vector(1,1)=N11aux1/N11aux2;

    N21aux1=-(eta*Yield*a*sqrt(3)*(((4*c2*eta*eta+9*c2)*F*F+9*c1)*a*a+54*c1*F*F));
    N21aux2=F*((2*eta*eta+9)*a*a+27*F*F)*sqrt((a*a*((4*eta*eta*eta*eta+18*eta*eta)*a*a*a*a+...
        108*eta*eta*F*F*a*a+(648*eta*eta+729)*F*F*F*F)/(F*F*((2*eta*eta+9)*a*a+27*F*F)^2)));
    N_vector(2,1)=N21aux1/N21aux2;

    N_bar=fs*fd*N_vector;

    C=[1/3 0;0 3/2];

    dSigma=[dp;dq];

    A_vector=L_bar\dSigma;
    B_vector=L_bar\N_bar;

    % Coefficients of quadratic equation
    a_coeff=B_vector'*C*B_vector-1;
    b_coeff=-A_vector'*C*B_vector-B_vector'*C*A_vector;
    c_coeff=A_vector'*C*A_vector;

    % solving for positive root x;

    x=(-b_coeff-sqrt((b_coeff^2)-4*a_coeff*c_coeff))/(2*a_coeff);

      % increase of strain invariants

      de_strain=A_vector-x*B_vector;

      de_v=de_strain(1);
      de_s=de_strain(2);

      Sigma=Sigma+dSigma;%       stress invariants
      de_void=(1+e_void)*-de_v;
      e_void=e_void+de_void;
      e_v=e_v+de_v;
      e_s=e_s+de_s;
      e_strain(jj+1,:)=[e_v e_s];
      Invariants(jj+1,:)=Sigma';
      e_void_(jj+1)=e_void;
end
```

Fig. D-2 Drained calculation (cont.)

```
else
    %% Undrained loading
    for jj=1:nsteps
        de_v=0;% volumetric strain
        p=Sigma(1);
        q=Sigma(2);
        eta=q/p;

        tanpsi=sqrt(2)*abs(q)/(3*abs(p));

        if eta<=0
            eta=0.0000001;
            cos3theta=(-sqrt(6)*2*eta*eta*eta/243)/((2*eta*eta/27)^1.5);
        else
            cos3theta=(-sqrt(6)*2*eta*eta*eta/243)/((2*eta*eta/27)^1.5);
        end

        F=sqrt((tanpsi*tanpsi/8)+((2-tanpsi*tanpsi)/(2+sqrt(2.)*tanpsi*cos3theta)))-(tanpsi/(2*sqrt(2.)));

        a=sqrt(3.)*(3-sin(phic))/(2*sqrt(2.)*sin(phic));

        pcr=exp((Nparam-log(1+e_void))/lambda)/2;
        alpha_power=log((lambda-kappa)*(3+a*a)/((lambda+kappa)*a*sqrt(3.)))/log(2.);

        fd=(p/pcr)^alpha_power;
        fdi=2^alpha_power;
        c1 = (1 + (a*a)/3 - fdi*a/(sqrt(3.)))/(1.5 * rparam);
        c2 = 1. + (1. - c1)*(3. / (a * a));
        fs=(3*p./lambda)/(3 + a*a - a*sqrt(3.)*fdi) ;

        Lmatrix(1,1)=c2*a*a/3+c1;
        Lmatrix(1,2)=c2*eta*a*a/3;
        Lmatrix(2,1)=Lmatrix(1,2);
        Lmatrix(2,2)=c2*eta*eta*a*a/3+9*c1/2;

        L_bar=fs*Lmatrix;

        I1=3*p;
        I2=q*q/3-3*p*p;
        I3=(-2*q*q*q/27+(p*q*q/3-p*p*p))*-1;

        Yield=(sqrt(3.)*a/(3+a*a)-1)*((I1*I2+9*I3)*(1-sin(phic)*sin(phic)))/(8*I3*sin(phic)*sin(phic))+sqrt(3.)*a/(3+a*a);

        if Yield>= 0.999
            return
        end

        N11aux1=-(Yield*a*sqrt(3)*(((4*c2*eta*eta+9*c2)*F*F-2*c1*eta*eta)*a*a+27*c1*F*F));
        N11aux2=F*((2*eta*eta+9)*a*a+27*F*F)*sqrt((a*a*((4*eta*eta*eta*eta+18*eta*eta)*a*a*a*a+...
            108*eta*eta*F*F*a*a+(648*eta*eta+729)*F*F*F*F)/(F*F*((2*eta*eta+9)*a*a+27*F*F)^2)));
        N_vector(1,1)=N11aux1/N11aux2;

        N21aux1=-(eta*Yield*a*sqrt(3)*(((4*c2*eta*eta+9*c2)*F*F+9*c1)*a*a+54*c1*F*F));
        N21aux2=F*((2*eta*eta+9)*a*a+27*F*F)*sqrt((a*a*((4*eta*eta*eta*eta+18*eta*eta)*a*a*a*a+...
            108*eta*eta*F*F*a*a+(648*eta*eta+729)*F*F*F*F)/(F*F*((2*eta*eta+9)*a*a+27*F*F)^2)));
        N_vector(2,1)=N21aux1/N21aux2;
        N_bar=fs*fd*N_vector;

        C=[1/3 0;0 3/2];

        Pmatrix=(L_bar(1,2).^-1)*(dp-L_bar(1,1)*de_v);
        Qmatrix=(L_bar(1,2)^-1)*N_bar(1,1);

        % Coefficients of quadratic equation

        a_coeff=Qmatrix'*C(2,2)*Qmatrix-1;
        b_coeff=-Qmatrix'*C(2,1)*de_v-de_v*C(1,2)*Qmatrix-Pmatrix'*C(2,2)*Qmatrix-Qmatrix'*C(2,2)*Pmatrix;
        c_coeff=de_v*C(1,1)*de_v+Pmatrix'*C(2,1)*de_v+de_v*C(1,2)*Pmatrix+Pmatrix'*C(2,2)*Pmatrix;

        % solving for positive root x;
        x=roots([a_coeff b_coeff c_coeff]);
        %   x=x(x>0);
        x=(-b_coeff+sqrt((b_coeff^2)-4*a_coeff*c_coeff))/(2*a_coeff);
        % increase in deviatoric strain

        de_s=Pmatrix-Qmatrix*x;

        % increase in deviatoric stress

        dq=L_bar(2,1)*de_v+L_bar(2,2)*de_s+N_bar(2)*x;

        dSigma=[dp;dq];% increase in the stress invariants

        Sigma=Sigma+dSigma;%       stress invariants

        de_void=(1+e_void)*-de_v;
        e_void=e_void+de_void;
        e_v=e_v+de_v;
        e_s=e_s+de_s;
        e_strain(jj+1,:)=[e_v e_s];
        Invariants(jj+1,:)=Sigma';
        e_void_(jj+1)=e_void;
    end
end
```

Fig. D-3 Undrained calculation

APPENDIX E

This appendix shows a sample calculation of the methodology shown in CHAPTER 3

N_{Vs}	-2.4717
I^*_{Vs}	0.2919
k^*_{Vs}	0.06
p'0	142

Vs0	68.4028

												This study
dVs*	dVs	Vsf	ln(1/Vsf)	dpe	pe_new	σnini	fd=-sn/pe	(λ+κ / 2λκ)*dεn	fd*(λ−κ / 2λκ)*|dεn|	dσn	$σn_{end}$	ln (σn)
-0.0005	0.034201	68.44	-4.2259	0.697	407.34	-142	0.349	-0.005	1.16E-03	-0.713	-142.713	4.961
-0.0005	0.03422	68.47	-4.2264	0.698	408.03	-142.713	0.35036	-0.005	1.16E-03	-0.717	-143.430	4.966
-0.0005	0.03424	68.51	-4.2269	0.699	408.73	-143.430	0.35152	-0.005	1.16E-03	-0.720	-144.151	4.971
-0.0005	0.03425	68.54	-4.2274	0.700	409.43	-144.151	0.35268	-0.005	1.17E-03	-0.724	-144.875	4.976
-0.0005	0.03427	68.57	-4.2279	0.701	410.13	-144.875	0.35384	-0.005	1.17E-03	-0.728	-145.602	4.981
-0.0005	0.03429	68.61	-4.2284	0.703	410.84	-145.602	0.35501	-0.005	1.18E-03	-0.731	-146.334	4.986
-0.0005	0.03430	68.64	-4.2289	0.704	411.54	-146.334	0.35619	-0.005	1.18E-03	-0.735	-147.069	4.991
-0.0005	0.03432	68.68	-4.2294	0.705	412.25	-147.069	0.35736	-0.005	1.18E-03	-0.739	-147.808	4.996
-0.0005	0.03434	68.71	-4.2299	0.706	412.95	-147.808	0.35854	-0.005	1.19E-03	-0.742	-148.550	5.001
-0.0005	0.03436	68.75	-4.2304	0.707	413.66	-148.550	0.35973	-0.005	1.19E-03	-0.746	-149.296	5.006
-0.0005	0.03437	68.78	-4.2309	0.709	414.37	-149.296	0.36092	-0.005	1.19E-03	-0.750	-150.046	5.011
-0.0005	0.03439	68.81	-4.2314	0.710	415.08	-150.046	0.36211	-0.005	1.20E-03	-0.754	-150.800	5.016
-0.0005	0.03441	68.85	-4.2319	0.711	415.79	-150.800	0.36331	-0.005	1.20E-03	-0.757	-151.557	5.021
-0.0005	0.03442	68.88	-4.2324	0.712	416.50	-151.557	0.36451	-0.005	1.21E-03	-0.761	-152.319	5.026
-0.0005	0.03444	68.92	-4.2329	0.713	417.21	-152.319	0.36571	-0.005	1.21E-03	-0.765	-153.084	5.031
-0.0005	0.03446	68.95	-4.2334	0.715	417.93	-153.084	0.36692	-0.005	1.21E-03	-0.769	-153.853	5.036
-0.0005	0.03448	68.99	-4.2339	0.716	418.64	-153.853	0.36813	-0.005	1.22E-03	-0.773	-154.626	5.041
-0.0005	0.03449	69.02	-4.2344	0.717	419.36	-154.626	0.36935	-0.005	1.22E-03	-0.777	-155.402	5.046
-0.0005	0.03451	69.06	-4.2349	0.718	420.08	-155.402	0.37057	-0.005	1.23E-03	-0.781	-156.183	5.051
-0.0005	0.03453	69.09	-4.2354	0.720	420.80	-156.183	0.37179	-0.005	1.23E-03	-0.785	-156.967	5.056
-0.0005	0.03455	69.12	-4.2359	0.721	421.52	-156.967	0.37302	-0.005	1.23E-03	-0.788	-157.756	5.061
-0.0005	0.03456	69.16	-4.2364	0.722	422.24	-157.756	0.37425	-0.005	1.24E-03	-0.792	-158.548	5.066
-0.0005	0.03458	69.19	-4.2369	0.723	422.97	-158.548	0.37549	-0.005	1.24E-03	-0.796	-159.345	5.071
-0.0005	0.03460	69.23	-4.2374	0.725	423.69	-159.345	0.37673	-0.005	1.25E-03	-0.800	-160.145	5.076
-0.0005	0.03461	69.26	-4.2379	0.726	424.42	-160.145	0.37798	-0.005	1.25E-03	-0.804	-160.950	5.081
-0.0005	0.03463	69.30	-4.2384	0.727	425.14	-160.950	0.37923	-0.005	1.26E-03	-0.808	-161.758	5.086
-0.0005	0.03465	69.33	-4.2389	0.728	425.87	-161.758	0.38048	-0.005	1.26E-03	-0.813	-162.571	5.091
-0.0005	0.03467	69.37	-4.2394	0.729	426.60	-162.571	0.38174	-0.005	1.26E-03	-0.817	-163.387	5.096
-0.0005	0.03468	69.40	-4.2399	0.731	427.33	-163.387	0.38300	-0.005	1.27E-03	-0.821	-164.208	5.101
-0.0005	0.03470	69.44	-4.2404	0.732	428.06	-164.208	0.38426	-0.005	0.001	-0.825	-165.033	5.106
-0.0005	0.03472	69.47	-4.2409	0.733	428.80	-165.033	0.38553	-0.005	0.001	-0.829	-165.862	5.111
-0.0005	0.03474	69.51	-4.2414	0.734	429.53	-165.862	0.38681	-0.005	0.001	-0.833	-166.695	5.116
-0.0005	0.03475	69.54	-4.2419	0.736	430.27	-166.695	0.38809	-0.005	0.001	-0.837	-167.532	5.121
-0.0005	0.03477	69.58	-4.2424	0.737	431.00	-167.532	0.38937	-0.005	0.001	-0.842	-168.374	5.126
-0.0005	0.03479	69.61	-4.2429	0.738	431.74	-168.374	0.39066	-0.005	0.001	-0.846	-169.219	5.131
-0.0005	0.03481	69.64	-4.2434	0.740	432.48	-169.219	0.39195	-0.005	0.001	-0.850	-170.069	5.136

Fig. E-1 Sample calculation of Consolidation based on Shear wave measurements

APPENDIX F

This appendix shows the PowerShell routine used to trigger automatically the Bender Elements during triaxial testing. Part of the code was adapted from the following sources:

- https://stackoverflow.com/questions/39353073/how-i-can-send-mouse-click-in-powershell.
- https://github.com/stridergdm/SimpleTalk_PowerShell-Scripts/tree/master/Countdown%20Timer

```
$cSource = @'
using System;
using System.Drawing;
using System.Runtime.InteropServices;
using System.Windows.Forms;
public class Clicker
{
//https://msdn.microsoft.com/en-
us/library/windows/desktop/ms646270(v=vs.85).aspx
[StructLayout(LayoutKind.Sequential)]
struct INPUT
{
    public int        type; // 0 = INPUT_MOUSE,
                            // 1 = INPUT_KEYBOARD
                            // 2 = INPUT_HARDWARE
    public MOUSEINPUT mi;
}

//https://msdn.microsoft.com/en-
us/library/windows/desktop/ms646273(v=vs.85).aspx
[StructLayout(LayoutKind.Sequential)]
struct MOUSEINPUT
{
    public int    dx ;
    public int    dy ;
    public int    mouseData ;
    public int    dwFlags;
    public int    time;
    public IntPtr dwExtraInfo;
}

//This covers most use cases although complex mice may have additional
buttons
//There are additional constants you can use for those cases, see the
msdn page
const int MOUSEEVENTF_MOVED      = 0x0001 ;
const int MOUSEEVENTF_LEFTDOWN   = 0x0002 ;
const int MOUSEEVENTF_LEFTUP     = 0x0004 ;
const int MOUSEEVENTF_RIGHTDOWN  = 0x0008 ;
const int MOUSEEVENTF_RIGHTUP    = 0x0010 ;
const int MOUSEEVENTF_MIDDLEDOWN = 0x0020 ;
const int MOUSEEVENTF_MIDDLEUP   = 0x0040 ;
const int MOUSEEVENTF_WHEEL      = 0x0080 ;
const int MOUSEEVENTF_XDOWN      = 0x0100 ;
const int MOUSEEVENTF_XUP        = 0x0200 ;
const int MOUSEEVENTF_ABSOLUTE   = 0x8000 ;

const int screen_length = 0x10000 ;

//https://msdn.microsoft.com/en-
us/library/windows/desktop/ms646310(v=vs.85).aspx
[System.Runtime.InteropServices.DllImport("user32.dll")]
```

```
       extern static uint SendInput(uint nInputs, INPUT[] pInputs, int cbSize);

       public static void LeftClickAtPoint(int x, int y)
       {
           //Move the mouse
           INPUT[] input = new INPUT[3];
           input[0].mi.dx =
x*(65535/System.Windows.Forms.Screen.PrimaryScreen.Bounds.Width);
           input[0].mi.dy =
y*(65535/System.Windows.Forms.Screen.PrimaryScreen.Bounds.Height);
           input[0].mi.dwFlags = MOUSEEVENTF_MOVED | MOUSEEVENTF_ABSOLUTE;
           //Left mouse button down
           input[1].mi.dwFlags = MOUSEEVENTF_LEFTDOWN;
           //Left mouse button up
           input[2].mi.dwFlags = MOUSEEVENTF_LEFTUP;
           SendInput(3, input, Marshal.SizeOf(input[0]));
       }
       }
       '@
       Add-Type -TypeDefinition $cSource -ReferencedAssemblies
System.Windows.Forms,System.Drawing


       # ------------------------------------


       # get GDSBES process
       $GDS = Get-Process GDSBES -ErrorAction SilentlyContinue
       if ($GDS) {
         # try gracefully first
         $GDS.CloseMainWindow()
         # kill after five seconds
         Sleep 5
         if (!$GDS.HasExited) {
           $GDS | Stop-Process -Force
         }
       }
       Remove-Variable GDS


       function Show-Process($Process, [Switch]$Maximize)
       {
         $sig = '
           [DllImport("user32.dll")] public static extern bool
ShowWindowAsync(IntPtr hWnd, int nCmdShow);
           [DllImport("user32.dll")] public static extern int
SetForegroundWindow(IntPtr hwnd);
         '

         if ($Maximize) { $Mode = 3 } else { $Mode = 4 }
         $type = Add-Type -MemberDefinition $sig -Name WindowAPI -PassThru
         $hwnd = $process.MainWindowHandle
         $null = $type::ShowWindowAsync($hwnd, $Mode)
         $null = $type::SetForegroundWindow($hwnd)
       }


       [Clicker]::LeftClickAtPoint(512,1029)


       Start-Sleep -s 5

       [System.Windows.Forms.SendKeys]::SendWait("%(o)")

       Start-Sleep -s 2

       [Clicker]::LeftClickAtPoint(699,458)
       [Clicker]::LeftClickAtPoint(699,458)

       Start-Sleep -s 2

       [System.Windows.Forms.SendKeys]::SendWait("144")
```

```
        Start-Sleep -s 2

        [System.Windows.Forms.SendKeys]::SendWait("%(n)")

        Start-Sleep -s 2

        [Clicker]::LeftClickAtPoint(858,386)
        [Clicker]::LeftClickAtPoint(858,386)

        Start-Sleep -s 1

        [System.Windows.Forms.SendKeys]::SendWait("0.1")

        Start-Sleep -s 1

        [System.Windows.Forms.SendKeys]::SendWait("%(n)")

        Start-Sleep -s 1

        [System.Windows.Forms.SendKeys]::SendWait("%(n)")

        Start-Sleep -s 1

        [System.Windows.Forms.SendKeys]::SendWait("%(s)")

        Start-Sleep -s 1


        $Number_shots=20; # total number of BE shots

        $hora= Get-Date -Format HH # disctintive hour for the shots (hour of the
FIRST shot taken)
        $minuto= Get-Date -Format mm # disctintive minute for the shots (hour of
the FIRST shot taken)

        # counter to repeat the following commands

        for ($idx = 1 ; $idx -le $Number_shots ; $idx++ )
        {

        $delay = 80 # time delay between BE shots in SECONDS

        # Triggering the bender element for the S-wave

        [Clicker]::LeftClickAtPoint(773,487)

        Start-Sleep -s 2

        # Save the S-wave shot

        [Clicker]::LeftClickAtPoint(775,556)

        Start-Sleep -s 1

        [System.Windows.Forms.SendKeys]::SendWait("FileName_S_$idx $hora
$minuto")

        Start-Sleep -s 1

        [System.Windows.Forms.SendKeys]::SendWait("{ENTER}")

        # time delay for the next pair of shots

        #Start-Sleep -s $delay

        # Counter for the next pair of shots

        $Counter_Form = New-Object System.Windows.Forms.Form
        $Counter_Form.Text = "Countdown Timer for BE shots!"
        $Counter_Form.Width = 450
        $Counter_Form.Height = 200
```

```
        $Counter_Label = New-Object System.Windows.Forms.Label
        $Counter_Label.AutoSize = $true
        $Counter_Label.ForeColor = "Green"
        $normalfont = New-Object System.Drawing.Font("Times New Roman",14)
        $Counter_Label.Font = $normalfont
        $Counter_Label.Left = 20
        $Counter_Label.Top = 20
        $Counter_Form.Controls.Add($Counter_Label)
        while ($delay -ge 0)
        {
          $Counter_Form.Show()
          $Counter_Label.Text = "Seconds Remaining: $($delay)"
          if ($delay -lt 5)
          {
             $Counter_Label.ForeColor = "Red"
             $fontsize = 20-$delay
             $warningfont = New-Object System.Drawing.Font("Times New
Roman",$fontsize,[System.Drawing.FontStyle]([System.Drawing.FontStyle]::Bold -
bor [System.Drawing.FontStyle]::Underline))
             $Counter_Label.Font = $warningfont
          }
         start-sleep 1
         $delay -= 1
        }
        $Counter_Form.Close()

        Show-Process -Process (Get-Process -Name GDSBES) -Maximize
```

REFERENCES

Ahmadi, A., and Ahmadi, M. M. (2019). "Three-dimensional numerical analysis of corner effect of an excavation supported by ground anchors." International Journal of Geotechnical Engineering, 1-13.

Airey, D., and Mohsin, A. K. M. (2013). "Evaluation of Shear Wave Velocity from Bender Elements Using Cross-correlation." Geotechnical Testing Journal, 36(4), 506-514.

ASTM (2014). "Standard test methods for crosshole seismic testing." ASTM D4428/D4428M-14 West Conshohocken, PA.

ASTM (2019). "Standard Test Methods for Downhole Seismic Testing." ASTM D7400/D7400M-19 West Conshohocken, PA.

Bahrami, M., Khodakarami, M. I., and Haddad, A. (2018). "3D numerical investigation of the effect of wall penetration depth on excavations behavior in sand." Computers and Geotechnics, 98, 82-92.

Bang, E.-S., and Kim, D.-S. (2007). "Evaluation of shear wave velocity profile using SPT based uphole method." Soil Dynamics and Earthquake Engineering, 27(8), 741-758.

Besson, A., Séger, M., Giot, G., and Cousin, I. (2013). "Identifying the characteristic scales of soil structural recovery after compaction from three in-field methods of monitoring." Geoderma, 204-205, 130-139.

Black, J., Stanier, S., and Clarke, S. "Shear wave velocity measurement of Kaolin during undrained unconsolidated triaxial compression." Proc., Proceedings of the 62nd Canadian Geotechnical Conference, Sheffield.

Boone, S. J. (1996). "Ground-Movement-Related Building Damage." Journal of Geotechnical Engineering, 122(11), 886-896.

Boone, S. J., Westland, J., and Nusink, R. (1999). "Comparative evaluation of building responses to an adjacent braced excavation." Canadian Geotechnical Journal, 36(2), 210-223.

Boscardin, M. D., and Cording, E. J. (1989). "Building Response to Excavation‐Induced Settlement." Journal of Geotechnical Engineering, 115(1), 1-21.

Brignoli, E. G., Gotti, M., and Stokoe, K. H. (1996). "Measurement of shear waves in laboratory specimens by means of piezoelectric transducers." Geotechnical testing journal, 19(4), 384-397.

Brinkgreve, R., Broere, W., and Waterman, D. (2007). "PLAXIS 2D." Version 8.5 finite-element code for soil and rock analyses: complete set of manuals.

Bryson, L. S. (2002). "Performance of a stiff excavation support system in soft clay and the response of an adjacent building."PhD dissertation, Northwestern Univ, Evanston, Ill.

Bryson, L. S., and Zapata-Medina, D. G. (2012). "Method for Estimating System Stiffness for Excavation Support Walls." Journal of Geotechnical and Geoenvironmental Engineering, 138(9), 1104-1115.

Bryson, L. S., Zapata-Medina, D. G., and Romana-Giraldo, J. (2018). "Empirical Method to Estimate Lateral Wall Deformation Profiles and Bending Moment in Excavation Retaining Walls." IFCEE 2018, 65-75.

Burd, H. J., Houlsby, G. T., Augarde, C. E., and Liu, G. (2000). "Modelling tunnelling-induced settlement of masonry buildings." Proceedings of the Institution of Civil Engineers - Geotechnical Engineering, 143(1), 17-29.

Burland, J. B., and Wroth, C. (1975). "Settlement of buildings and associated damage."

Butterfield, R. (1979). "A natural compression law for soils (an advance on e–log p′)." Géotechnique, 29(4), 469-480.

Calamita, G., Serlenga, V., Stabile, T. A., Gallipoli, M. R., Bellanova, J., Bonano, M., Casu, F., Vignola, L., Piscitelli, S., and Perrone, A. (2019). "An integrated geophysical approach for urban underground characterization: the Avigliano town (southern Italy) case study." Geomatics, Natural Hazards and Risk, 10(1), 412-432.

Chen, H., Li, J., and Li, L. (2018). "Performance of a Zoned Excavation by Bottom-Up Technique in Shanghai Soft Soils." Journal of Geotechnical and Geoenvironmental Engineering, 144(11), 05018003.

Cheshomi, A., and Khalili, A. (2021). "Comparison between pressuremeter modulus (EPMT) and shear wave velocity (Vs) in silty clay soil." Journal of Applied Geophysics, 192, 104399.

Chheng, C., and Likitlersuang, S. (2018). "Underground excavation behaviour in Bangkok using three-dimensional finite element method." Computers and Geotechnics, 95, 68-81.

Choo, J., Jung, Y.-H., and Chung, C.-K. (2011). "Effect of Directional Stress History on Anisotropy of Initial Stiffness of Cohesive Soils Measured by Bender Element Tests." Soils and Foundations, 51(4), 737-747.

Choudhury, T., and Kaushik, H. B. (2018). "Seismic Response Sensitivity to Uncertain Variables in RC Frames with Infill Walls." Journal of Structural Engineering, 144(10), 04018184.

Clough, G. W. (1990). "Construction induced movements of in situ walls." Design and performance of earth retaining structures, 439-470.

Clough, G. W., Smith, E. M., and Sweeney, B. P. "Movement control of excavation support systems by iterative design." Proc., Foundation engineering: Current principles and practices, ASCE, 869-884.

Crawford, M. M., Bryson, L. S., Woolery, E. W., and Wang, Z. (2019). "Long-term landslide monitoring using soil-water relationships and electrical data to estimate suction stress." Engineering Geology, 251, 146-157.

Díaz-Curiel, J., Biosca, B., Arévalo-Lomas, L., and Rueda-Quintero, S. (2020). "Improved use of seismic profiles to estimate allowable pressure in granular soils: Application to quaternary deposits with different gradings." Journal of Applied Geophysics, 175, 103988.

Do, T.-N., Ou, C.-Y., and Lim, A. (2013). "Evaluation of Factors of Safety against Basal Heave for Deep Excavations in Soft Clay Using the Finite-Element Method." Journal of Geotechnical and Geoenvironmental Engineering, 139(12), 2125-2135.

Dong, Y., Burd, H., Houlsby, G., and Hou, Y. (2014). "Advanced finite element analysis of a complex deep excavation case history in Shanghai." Frontiers of Structural and Civil Engineering, 8(1), 93-100.

Donohue, S., Gavin, K., and Tolooiyan, A. (2011). "Geophysical and geotechnical assessment of a railway embankment failure." Near Surface Geophysics, 9(1), 33-44.

Duan, W., Cai, G., Liu, S., and Puppala, A. J. (2019). "Correlations between Shear Wave Velocity and Geotechnical Parameters for Jiangsu Clays of China." Pure and Applied Geophysics, 176(2), 669-684.
Dulácska, E. (1992). Soil settlement effects on buildings, Elsevier.
Dunnicliff, J. (1993). Geotechnical instrumentation for monitoring field performance, John Wiley & Sons.
Dutta, T. T., Otsubo, M., and Kuwano, R. (2021). "Effect of shearing history on stress wave velocities of sands observed in triaxial compression tests." Soils and Foundations, 61(2), 541-548.
Elbeggo, D., Hussien, M. N., Ethier, Y., and Karray, M. (2019). "Robustness of the P-RAT in the Shear-Wave Velocity Measurement of Soft Clays." Journal of Geotechnical and Geoenvironmental Engineering, 145(5), 04019014.
Fang, H. Y. (1991). Foundation engineering handbook, Van Nostrand Reinhold, New York.
Fellin, W. (2002). "Hypoplasticity for beginners." University of Innsbruck.
Finno, R. J., and Bryson, L. S. (2002). "Response of Building Adjacent to Stiff Excavation Support System in Soft Clay." Journal of Performance of Constructed Facilities, 16(1), 10-20.
Finno, R. J., Arboleda-Monsalve, L. G., and Sarabia, F. (2015). "Observed Performance of the One Museum Park West Excavation." Journal of Geotechnical and Geoenvironmental Engineering, 141(1), 04014078.
Finno, R. J., Blackburn, J. T., and Roboski, J. F. (2007). "Three-Dimensional Effects for Supported Excavations in Clay." Journal of Geotechnical and Geoenvironmental Engineering, 133(1), 30-36.
Finno, R. J., Bryson, S., and Calvello, M. (2002). "Performance of a Stiff Support System in Soft Clay." Journal of Geotechnical and Geoenvironmental Engineering, 128(8), 660-671.
Finno, R. J., Voss, F. T., Rossow, E., and Blackburn, J. T. (2005). "Evaluating Damage Potential in Buildings Affected by Excavations." Journal of Geotechnical and Geoenvironmental Engineering, 131(10), 1199-1210.
GDS-Instruments. 2010. GDSBES GDS Instruments, Hook, U.K.
Germaine, J. T., and Germaine, A. V. (2009). Geotechnical laboratory measurements for engineers, John Wiley & Sons.
Ghorbani, A., Jafarian, Y., and Maghsoudi, M. S. (2012). "Estimating shear wave velocity of soil deposits using polynomial neural networks: Application to liquefaction." Computers & Geosciences, 44, 86-94.
Goh, A. T. C. (2017). "Basal heave stability of supported circular excavations in clay." Tunnelling and Underground Space Technology, 61, 145-149.
Goh, K. H., and Mair, R. J. (2014). "Response of framed buildings to excavation-induced movements." Soils and Foundations, 54(3), 250-268.
Gouveia, F., Gomes, R. C., and Lopes, I. (2019). "Shallow and in depth seismic testing in urban environment: A case study in Lisbon Miocene stiff soils using joint inversion of active and passive Rayleigh wave measurements." Journal of Applied Geophysics, 169, 199-213.

Guadalupe, Y., Baxter, C. D. P., and Sharma, M. S. R. (2013). "Measuring Shear Wave Velocity in Laboratory to Link Small- and Large-Strain Behavior of Soils." Transportation Research Record, 2335(1), 79-88.
Halim, D., and Wong, K. S. (2012). "Prediction of Frame Structure Damage Resulting from Deep Excavation." Journal of Geotechnical and Geoenvironmental Engineering, 138(12), 1530-1536.
Harahap, S. E., and Ou, C.-Y. (2019). "Finite element analysis of time-dependent behavior in deep excavations." Computers and Geotechnics, 103300.
Hardin, B. O., and Black, W. L. (1968). "Vibration Modulus of Normally Consolidated Clay." Journal of the Soil Mechanics and Foundations Division, 94(2), 353-369.
Hardin, B. O., and Richart, F. E. (1963). "Elastic Wave Velocities in Granular Soils." Journal of the Soil Mechanics and Foundations Division, 89(1), 33-65.
Houlsby, G. T., and Wroth, C. P. (1991). "The variation of shear modulus of a clay with pressure and overconsolidation ratio." Soils and Foundations, 31(3), 138-143.
Hsieh, P.-G., and Ou, C.-Y. (1998). "Shape of ground surface settlement profiles caused by excavation." Canadian Geotechnical Journal, 35(6), 1004-1017.
Hsiung, B.-C. B., Yang, K.-H., Aila, W., and Ge, L. (2018). "Evaluation of the wall deflections of a deep excavation in Central Jakarta using three-dimensional modeling." Tunnelling and Underground Space Technology, 72, 84-96.
Hsiung, B.-C. B., Yang, K.-H., Aila, W., and Hung, C. (2016). "Three-dimensional effects of a deep excavation on wall deflections in loose to medium dense sands." Computers and Geotechnics, 80, 138-151.
Hua, T., Yang, Z., Yang, X., Huang, H., Yao, Q., Wu, G., and Li, H. (2020). "Assessment of geomaterial compaction using the pressure-wave fundamental frequency." Transportation Geotechnics, 22, 100318.
Huang, M., Tang, Z., and Yuan, J. (2018). "Basal stability analysis of braced excavations with embedded walls in undrained clay using the upper bound theorem." Tunnelling and Underground Space Technology, 79, 231-241.
Imani, P., Tian, G., Hadiloo, S., and El-Raouf, A. A. (2021). "Application of combined electrical resistivity tomography (ERT) and seismic refraction tomography (SRT) methods to investigate Xiaoshan District landslide site: Hangzhou, China." Journal of Applied Geophysics, 184, 104236.
Jodry, C., Palma Lopes, S., Fargier, Y., Sanchez, M., and Côte, P. (2019). "2D-ERT monitoring of soil moisture seasonal behaviour in a river levee: A case study." Journal of Applied Geophysics, 167, 140-151.
Kadlíček, T., Janda, T., Šejnoha, M., Mašín, D., Najser, J., and Beneš, Š. (2022). "Automated calibration of advanced soil constitutive models. Part II: hypoplastic clay and modified Cam-Clay." Acta Geotechnica.
Kang, X., Kang, G.-C., and Bate, B. (2014). "Measurement of stiffness anisotropy in kaolinite using bender element tests in a floating wall consolidometer." Geotechnical Testing Journal, 37(5), 869-883.
Koutsoftas, D. C., Frobenius, P., Wu, C. L., Meyersohn, D., and Kulesza, R. (2000). "Deformations during Cut-and-Cover Construction of MUNI Metro Turnback Project." Journal of Geotechnical and Geoenvironmental Engineering, 126(4), 344-359.

Kung, G. T., Juang, C. H., Hsiao, E. C., and Hashash, Y. M. (2007). "Simplified Model for Wall Deflection and Ground-Surface Settlement Caused by Braced Excavation in Clays." Journal of Geotechnical and Geoenvironmental Engineering, 133(6), 731-747.

L'Heureux, J.-S., and Long, M. (2017). "Relationship between Shear-Wave Velocity and Geotechnical Parameters for Norwegian Clays." Journal of Geotechnical and Geoenvironmental Engineering, 143(6), 04017013.

Landon, M. M., DeGroot, D. J., and Sheahan, T. C. (2007). "Nondestructive Sample Quality Assessment of a Soft Clay Using Shear Wave Velocity." Journal of Geotechnical and Geoenvironmental Engineering, 133(4), 424-432.

Lee, J.-S., and Santamarina, J. C. (2005). "Bender Elements: Performance and Signal Interpretation." Journal of Geotechnical and Geoenvironmental Engineering, 131(9), 1063-1070.

L'Heureux, J. S., Long, M., Vanneste, M., Sauvin, G., Hansen, L., Polom, U., Lecomte, I., Dehls, J., and Janbu, N. (2013). "On the prediction of settlement from high-resolution shear-wave reflection seismic data: The Trondheim harbour case study, mid Norway." Engineering Geology, 167, 72-83.

Li, D., Li, Z., and Tang, D. (2015). "Three-dimensional effects on deformation of deep excavations." Proceedings of the Institution of Civil Engineers - Geotechnical Engineering, 168(6), 551-562.

Likitlersuang, S., Surarak, C., Wanatowski, D., Oh, E., and Balasubramaniam, A. (2013). "Finite element analysis of a deep excavation: A case study from the Bangkok MRT." Soils and Foundations, 53(5), 756-773.

Lim, A., and Ou, C.-Y. (2018). "Performance and Three-Dimensional Analyses of a Wide Excavation in Soft Soil with Strut-Free Retaining System." International Journal of Geomechanics, 18(9), 05018007.

Lin, C.-H., Lin, C.-P., Dai, Y.-Z., and Chien, C.-J. (2017). "Application of surface wave method in assessment of ground modification with improvement columns." Journal of Applied Geophysics, 142, 14-22.

Long, M. (2001). "Database for Retaining Wall and Ground Movements due to Deep Excavations." Journal of Geotechnical and Geoenvironmental Engineering, 127(3), 203-224.

Marchetti, S., Monaco, P., Totani, G., and Marchetti, D. (2008). "In Situ Tests by Seismic Dilatometer (SDMT)." From Research to Practice in Geotechnical Engineering, 292-311.

Mašín, D. (2005). "A hypoplastic constitutive model for clays." International Journal for Numerical and Analytical Methods in Geomechanics, 29(4), 311-336.

Mašín, D. (2009). "Comparison of Predictive Capabilities of Selected Elasto-Plastic and Hypoplastic Models for Structured Clays." Soils and Foundations, 49(3), 381-390.

Mašín, D. (2019). Modelling of Soil Behaviour with Hypoplasticity Another Approach to Soil Constitutive Modelling, Springer International Publishing, Cham.

Melo, L. B. B. d., Silva, B. M., Peixoto, D. S., Chiarini, T. P. A., de Oliveira, G. C., and Curi, N. (2021). "Effect of compaction on the relationship between electrical resistivity and soil water content in Oxisol." Soil and Tillage Research, 208, 104876.

Microsoft-Corporation. 2016. Powershell, Redmond, WA: Microsoft Corporation.

Mohamad Nor, O., Abbiss, C. P., Mohd. Raihan, T., and Khairul Anuar Mohd, N. (2011). "Prediction of long-term settlement on soft clay using shear wave velocity and damping characteristics." Engineering Geology, 123(4), 259-270.
Moon, S.-W., and Ku, T. (2016). "Development of global correlation models between in situ stress-normalized shear wave velocity and soil unit weight for plastic soils." Canadian Geotechnical Journal, 53(10), 1600-1611.
Moon, S.-W., and Ku, T. (2018). "Undrained Shear Strength in Cohesive Soils Estimated by Directional Modes of In-Situ Shear Wave Velocity." Geotechnical and Geological Engineering, 36(5), 2851-2868.
Muttashar, W. R., and Bryson, L. S. (2020). "Constitutive model for predicting stress-strain behavior of fine-grained sediments using shear-wave velocity." Marine Georesources & Geotechnology, 38(8), 896-910.
Muttashar, W. R., Bryson, L. S., and Woolery, E. (2019). "Determining the effects of depositional processes on consolidation behavior of sediment using shear-wave velocity." Marine Georesources & Geotechnology, 37(9), 1032-1043.
Ni, S.-H., Chang, W.-J., Yang, Y.-Z., and Fan, E.-S. (2018). "Evaluating Compaction Quality during Earth Dam Construction Using Multi-Channel Analysis of Surface Wave." Geotechnical Earthquake Engineering and Soil Dynamics V, 432-442.
Niemunis, A. (2002). "Extended hypoplastic models for soils."Habilitation Thesis, Ruhr-University, Bochum.
Oh, T.-M., Bang, E.-S., Cho, G.-C., and Park, E.-S. (2017). "Estimation of undrained shear strength for saturated clay using shear wave velocity." Marine Georesources & Geotechnology, 35(2), 236-244.
Orazalin, Z. Y., Whittle, A. J., and Olsen, M. B. (2015). "Three-Dimensional Analyses of Excavation Support System for the Stata Center Basement on the MIT Campus." Journal of Geotechnical and Geoenvironmental Engineering, 141(7), 05015001.
Ou, C.-Y. (2006). Deep excavation: Theory and practice, Taylor & Francis, London.
Owusu-Nimo, F., and Boadu, F. K. (2020). "Evaluating effective stress conditions in soils using non-invasive electrical measurements – Laboratory studies." Journal of Applied Geophysics, 174, 103961.
Pasierb, B., Grodecki, M., and Gwóźdź, R. (2019). "Geophysical and geotechnical approach to a landslide stability assessment: a case study." Acta Geophysica, 67(6), 1823-1834.
Peck, R. B. (1969). "Deep excavations and tunneling in soft ground." Proc. 7th ICSMFE, 1969, 225-290.
Polshin, D. E., and Tokar, R. "Maximum allowable non-uniform settlement of structures." Proc., Proc., 4th Int. Conf. on Soil Mechanics and Foundation Engineering, Butterworth's London, 402-405.
Robertson, P. K., Sasitharan, S., Cunning, J. C., and Sego, D. C. (1995). "Shear-Wave Velocity to Evaluate In-Situ State of Ottawa Sand." Journal of Geotechnical Engineering, 121(3), 262-273.
Roboski, J., and Finno, R. J. (2006). "Distributions of ground movements parallel to deep excavations in clay." Canadian Geotechnical Journal, 43(1), 43-58.
Romero-Ruiz, A., Linde, N., Baron, L., Breitenstein, D., Keller, T., and Or, D. (2022). "Lasting Effects of Soil Compaction on Soil Water Regime Confirmed by Geoelectrical Monitoring." Water Resources Research, 58(2), e2021WR030696.

Sabatini, P., Pass, D. G., and Bachus, R. C. (1999). "Ground anchors and anchored systems." United States. Federal Highway Administration. Office of Bridge Technology.

Sanchez-Salinero, I., Rosset, J. M., and Stokoe, K. H. II. (1986). "Analytical Studies of Body Wave Propagation and Attenuation." Rep. No. GR 86-15, Univ. of Texas, Austin, TX.

Santamarina, J. C., Klein, K. A., and Fam, M. A. (2001). Soils and waves, J. Wiley & Sons New York.

Schneider, J., Flemings, P. B., Day-Stirrat, R. J., and Germaine, J. T. (2011). "Insights into pore-scale controls on mudstone permeability through resedimentation experiments." Geology, 39(11), 1011-1014.

Schuster, M., Kung, G. T.-C., Juang, C. H., and Hashash, Y. M. A. (2009). "Simplified Model for Evaluating Damage Potential of Buildings Adjacent to a Braced Excavation." Journal of Geotechnical and Geoenvironmental Engineering, 135(12), 1823-1835.

Shams Maleki, Y., and Khazaei, J. (2017). "A Numerical Comparison of the Behavior of a Braced Excavation Using Two and Three-Dimensional Creep Plastic Analyses." Geotechnical and Geological Engineering, 35(5), 2017-2035.

Shirley, D. J., and Hampton, L. D. (1978). "Shear-wave measurements in laboratory sediments." The Journal of the Acoustical Society of America, 63(2), 607-613.

Skempton, A. W., and MacDonald, D. H. "The Allowable Settlements of Buildings." Proc., Proceedings of the Institution of Civil Engineers, 727-768.

Skempton, A. W., and Macdonald, D. H. (1956). "The allowable settlements of buildings." Proc. Inst. Civ. Eng, 5(6), 727-768.

Son, M., and Cording, E. J. (2005). "Estimation of Building Damage Due to Excavation-Induced Ground Movements." Journal of Geotechnical and Geoenvironmental Engineering, 131(2), 162-177.

Son, M., and Cording, E. J. (2011). "Responses of Buildings with Different Structural Types to Excavation-Induced Ground Settlements." Journal of Geotechnical and Geoenvironmental Engineering, 137(4), 323-333.

Stolte, A. C., and Cox, B. R. (2020). "Towards consideration of epistemic uncertainty in shear-wave velocity measurements obtained via seismic cone penetration testing (SCPT)." Canadian Geotechnical Journal, 57(1), 48-60.

Sun, Y., Zhou, S., and Luo, Z. (2017). "Basal-heave analysis of pit-in-pit braced excavations in soft clays." Computers and Geotechnics, 81, 294-306.

Tan, Y., and Wei, B. (2012). "Observed Behaviors of a Long and Deep Excavation Constructed by Cut-and-Cover Technique in Shanghai Soft Clay." Journal of Geotechnical and Geoenvironmental Engineering, 138(1), 69-88.

Tan, Y., Huang, R., Kang, Z., and Bin, W. (2016). "Covered Semi-Top-Down Excavation of Subway Station Surrounded by Closely Spaced Buildings in Downtown Shanghai: Building Response." Journal of Performance of Constructed Facilities, 30(6), 04016040.

Tan, Y., Li, X., Kang, Z., Liu, J., and Zhu, Y. (2015). "Zoned Excavation of an Oversized Pit Close to an Existing Metro Line in Stiff Clay: Case Study." Journal of Performance of Constructed Facilities, 29(6), 04014158.

Teng, F., Arboleda-Monsalve, L. G., and Finno, R. J. (2018). "Numerical Simulation of Recent Stress-History Effects on Excavation Responses in Soft Clays." Journal of Geotechnical and Geoenvironmental Engineering, 144(8), 06018005.
Terzaghi, K. (1943). Theoretical soil mechanics, Wiley, New York:.
Tezcan, S. S., Keceli, A., and Ozdemir, Z. (2006). "Allowable Bearing Capacity of Shallow Foundations Based on Shear Wave Velocity." Geotechnical & Geological Engineering, 24(1), 203-218.
Timoshenko, S. (1957). Strength of materials, D. Van Nostrand Company, New York.
Trafford, A., and Long, M. (2020). "Relationship between Shear-Wave Velocity and Undrained Shear Strength of Peat." Journal of Geotechnical and Geoenvironmental Engineering, 146(7), 04020057.
Tschebotarioff, G. P. (1973). Foundations, retaining, and earth structures, McGraw-Hill, New York.
Ukritchon, B., Whittle, A. J., and Sloan, S. W. (2003). "Undrained Stability of Braced Excavations in Clay." Journal of Geotechnical and Geoenvironmental Engineering, 129(8), 738-755.
Uyanık, O. (2011). "The porosity of saturated shallow sediments from seismic compressional and shear wave velocities." Journal of Applied Geophysics, 73(1), 16-24.
Vardanega, P. J., and Bolton, M. D. (2013). "Stiffness of Clays and Silts: Normalizing Shear Modulus and Shear Strain." Journal of Geotechnical and Geoenvironmental Engineering, 139(9), 1575-1589.
Viggiani, G., and Atkinson, J. H. (1995). "Interpretation of bender element tests." Géotechnique, 45(1), 149-154.
Wang, F., Li, D., Du, W., Zarei, C., and Liu, Y. (2021). "Bender Element Measurement for Small-Strain Shear Modulus of Compacted Loess." International Journal of Geomechanics, 21(5), 04021063.
Wang, X., Huang, H., Shen, S., Jin, G., Mao, Q., and Lu, H. (2020). "Characterization of In Situ Modulus of Asphalt Pavement and Its Relation to Cracking Performance Using SASW Method." Journal of Transportation Engineering, Part B: Pavements, 146(3), 04020039.
Wang, Y. H., Lo, K. F., Yan, W. M., and Dong, X. B. (2007). "Measurement Biases in the Bender Element Test." Journal of Geotechnical and Geoenvironmental Engineering, 133(5), 564-574.
Whiteley, J. S., Watlet, A., Uhlemann, S., Wilkinson, P., Boyd, J. P., Jordan, C., Kendall, J. M., and Chambers, J. E. (2021). "Rapid characterisation of landslide heterogeneity using unsupervised classification of electrical resistivity and seismic refraction surveys." Engineering Geology, 290, 106189.
Whitlow, R. D., Haskins, R., McComas, S. L., Crane, C. K., Howard, I. L., and McKenna, M. H. (2019). "Remote Bridge Monitoring Using Infrasound." Journal of Bridge Engineering, 24(5), 04019023.
Xiao, X., Li, M.-G., Wang, J.-H., and Chen, J.-J. (2018). "Numerical Evaluation of Control Measures for Tunnel Deformation Induced by an Oversized Deep Excavation." Journal of Aerospace Engineering, 31(6), 04018109.

Yamashita, S., Kawaguchi, T., Nakata, Y., Mikami, T., Fujiwara, T., and Shibuya, S. (2009). "Interpretation of international parallel test on the measurement of Gmax using bender elements." Soils and Foundations, 49(4), 631-650.

Yoo, J.-K., Park, D., and Baxter, C. D. P. (2018). "Estimation of Drained Shear Strength of Granular Soil from Shear Wave Velocity and Confining Stress." Journal of Geotechnical and Geoenvironmental Engineering, 144(6), 04018027.

Zhang, L. M., and Ng, A. M. Y. (2005). "Probabilistic limiting tolerable displacements for serviceability limit state design of foundations." Géotechnique, 55(2), 151-161.

Zhao, Y. (2016). "Soil Moduli Obtained from a Back Pressure Constant Rate of Strain Bender Element Consolidation Apparatus."PhD thesis, University of Arkansas, Fayetteville, AR

Zhao, Y. (2016). Soil Moduli Obtained from a Back Pressure Constant Rate of Strain Bender Element Consolidation Apparatus, University of Arkansas.

Zhao, Y., Mahmood, N., and Coffman, R. A. (2020). "Soil Fabric and Anisotropy as Observed Using Bender Elements during Consolidation." International Journal of Geomechanics, 20(4), 04020029.

VITA

EDUCATION

University of Kentucky | Lexington, KY
Master of Science | Civil Engineering 2018
Universidad Nacional de Colombia | Medellin, Colombia
Bachelor of Science | Civil Engineering 2014

RESEARCH EXPERIENCE

University of Kentucky | Lexington, KY
Research/Teaching Assistant 2016-Present

WORK EXPERIENCE

Alfa y Omega Engineers | Rionegro, Colombia
Staff Engineer 2015-2016

PEER-REVIEWED AND CONFERENCE PUBLICATIONS

- Bryson, L. S., Zapata-Medina, D. G., and Romana-Giraldo, J. (2018). "Empirical Method to Estimate Lateral Wall Deformation Profiles and Bending Moment in Excavation Retaining Walls." IFCEE 2018 Orlando, Florida.
- Huff; J., Bryson;, L. S., and Giraldo, J. R. (2018). "Economy and Design of Augered Cast-In-Place Piles at the Fargo WTP." IFCEE 2018, ASCE, Orlando, Florida.
- Bryson, L. S., Zapata-Medina, D. G., and Romana-Giraldo, J. (2018). "Empirical Method to Estimate Lateral Wall Deformation Profiles and Bending Moment in Excavation Retaining Walls." IFCEE 2018, 65-75.
- Bryson, L. S., and Giraldo, J. R. (2020). "Analysis of case study presenting ground anchor load-transfer response in shale stratum." Canadian Geotechnical Journal, 57(1), 85-99.
- Romana Giraldo, J., Bryson, L. S., and Gutierrez Soto, M. (2020). "Performance of Two Anchored Walls Under Cut and Fill Construction Sequences." Geotechnical and Geological Engineering, 38(2), 1799-1816.

- Romana-Giraldo, J., and Bryson, L. S. (2021). "Excavation Support System Design Method to Limit Damage in Adjacent Infrastructure." Journal of Geotechnical and Geoenvironmental Engineering, 147(12), 04021147.
- Romana-Giraldo, J., and Bryson, L. S. (2021). "Simplified Strut-Based Model for Cracking of Infill Walls due to Excavation-Induced Distortions." IFCEE 2021, 34-43.